

**Analytical development for precise and accurate  
determination of highly siderophile elements in  
geological samples and its application to the study  
of Horoman peridotite massif, Japan**

2019, March

ZHOU Xiaoyu

Graduate School of Natural Science and Technology  
(Doctor`s course)  
OKAYAMA UNIVERSITY

## Abstract

Recent development of analytical instruments enables to determine the sub-ng g<sup>-1</sup> level of highly siderophile elements (HSEs: Ru, Rh, Pd, Re, Os, Ir, Pt, and Au) in the geological samples. Inductively coupled plasma mass spectrometer (ICP-MS) coupled with isotope dilution (ID) method (except for monoisotopic elements Rh and Au) is able to provide highly precise and accurate HSE data. Currently, sample decomposition using inverse aqua regia at elevated temperatures and pressures (e.g., Carius tube CT or high pressure asher HPA) is one of the most common methods used to extract HSEs from geological samples. Moreover, it has been recognized that additional HF-desilicification is necessary to recover the HSEs, potentially contained within the silicate or oxide minerals in mafic samples, which cannot be dissolved solely by inverse aqua regia. However, the abundances of interfering elements and the concentration of HSEs in procedural blanks tend to increase in the eluent when conventional ion-exchange purification procedures are applied to the desilicified samples. In this study, we developed a newly developed purification procedure for HSEs analysis, using a cation exchange resin (AG 50W-X12) and three additional purification steps. When the HF-desilicification was performed during sample decomposition, trace amounts of Zr, forming stable fluoro-complex, cannot be removed by Ln resin. Chelex 100 resin, however, can effectively separate Pd from the Zr fluoro-complex. Furthermore, the Cr multi-oxide interference for Ru measurement was further purified by the final AG50W-X8 resin and critically evaluated. With careful purification and utilisation of the desolvating nebulizer system, the ratios of the interferences intensities relative to the measured intensities of HSE isotope masses: CrO<sub>3</sub><sup>+</sup>/Ru<sup>+</sup>, YO<sup>+</sup>/Pd<sup>+</sup>, Cd<sup>+</sup>/Pd<sup>+</sup>, ZrO<sup>+</sup>/Pd<sup>+</sup>, HfO<sup>+</sup>/Ir<sup>+</sup> and HfO<sup>+</sup>/Pt<sup>+</sup>, were reduced by less than a few hundred parts per million. Thus, no interference correction is required for the measurement of Ru, Pd, Re, Ir and Pt for both desilicified and non-desilicified geological samples, with a low procedural blank concentration comparable to or better than the conventional methods.

The effectiveness of HF-desilicification on the extraction of Ru, Pd, Re, Ir and Pt from whole rock sample was evaluated for five geological reference materials UB-N (serpentinite, CRPG), JP-1 (harzburgite, GSJ), TDB-1(diabase, CCRMP), MUH-1(harzburgite, IAG) and OKUM (komatiitic basalt, IAG). Our results indicate that desilicification is required to enhance the recovery of both Ru (~30%) and Re (~10%) from TDB-1. However, unlike mafic rock, UB-N, JP-1 and MUH-1 are independent of the use of HF or not, as their HSE data in desilicified and non-desilicified samples displayed no significant differences. The reference material OKUM presented different characteristics of HSEs as ultramafic rock. In this study, the systematic higher desilicified data of Ru (~11%), Ir (~24%) and Pt (~13%) than non-desilicified data demonstrate that the HF-desilicification is effective to liberate Ru, Ir and Pt from the residues during CT decomposition.

Horoman peridotite complex is one of the least altered peridotite massifs in the world and preserve the unique chemical and isotopic compositions, which may record multiple mantle processes. In this study, we determined HSE abundances and  $^{187}\text{Os}/^{188}\text{Os}$  ratios of a suite of samples, ranging from fertile plagioclase lherzolites through refractory spinel lherzolites to highly depleted spinel harzburgites, and subordinated dunite. Generally, the positive correlations between Re and S,  $\text{Al}_2\text{O}_3$ , and Yb concentrations, ranging from harzburgites, spinel lherzolites to plagioclase lherzolites, indicate that harzburgites and spinel lherzolites may have experienced higher degrees of melt extraction during partial melting. The melt extraction may have occurred at ~1.4 Ga using the most depleted harzburgite samples based on Re depletion model ages. Moreover, it is also observed that most massive plagioclase lherzolite samples showed depleted Os and Ru patterns relative to the primitive upper mantle (PUM), and higher  $^{187}\text{Re}/^{188}\text{Os}$  ratios than the 4.56 Ga reference line for PUM in Re-Os isochron diagram, which could not be simply explained by melt extraction. The Os subtraction process occurred in massive plagioclase lherzolites basically controlled the higher  $^{187}\text{Re}/^{188}\text{Os}$  ratios. The depletions of Ru

and Os in massive plagioclase lherzolites could be caused by the dissolution of platinum group element minerals such as  $\text{RuS}_2$ - $\text{OsS}_2$  phases during metamorphic or alteration processes (e.g., melt/fluid rock reactions). Moreover, the higher enrichment of Re in one sample might be also possibly attributed to the Re addition caused by melt-rock interaction process. Nevertheless, the Os subtraction process is likely to be a predominant secondary process following melt extraction among most massive plagioclase lherzolites. The thin-layer peridotites preserved successive melt extraction, melt-rock interaction, sulfide precipitation processes based on HSE abundances and Re-Os isotope system. The peridotites with the most depletion of Pt, Pd and Re may only undergo melt extraction; peridotites with higher  $^{187}\text{Re}/^{188}\text{Os}$  ratios may experience melt-rock reaction by addition of Re and Pd; the rest of thin-layer peridotites were reacted with S-saturated melt. The Pt and Pd were dissolved and precipitated again in sulfide, but less Re was added, leading to lower  $^{187}\text{Re}/^{188}\text{Os}$  ratios. Dunite presented different behavior of HSE abundances and Os isotopic compositions among all the Horoman peridotite samples. The enrichment of Pd, Pt and Re concentrations compared to PUM, and relatively higher  $^{187}\text{Re}/^{188}\text{Os}$  ratios than PUM may be attributed to the process of the basaltic-melt addition to the peridotites. Also, the fluid alteration could be one of the explanations for the highly radiogenic  $^{187}\text{Os}/^{188}\text{Os}$  ratios observed in dunite, which may have occurred at the subduction zone at younger age.

## **Acknowledgement**

I would like to express my honest appreciation and deep gratitude to all people who have encouraged and supported me throughout my PhD thesis work.

First of all, I would like to express my sincerest gratitude to my supervisor Prof. Eizo Nakamura at Institute for Planetary Materials, Okayama University, for giving me an opportunity to this project in his group in PML, and also his scientific guidance and constant encouragement during my research work.

I would like to thank my co-supervisor Prof. Ryoji Tanaka, who always supported a lot for analytical techniques, scientific advice and improving the manuscript during the course of this study. I would also like to thank Dr. Masahiro Yamanaka and Ms. Chie Sakaguchi, who always helped and supported me a lot during my clean room work. Special thanks go to Mrs. Kayo Tanaka for her technical supports, I'm very grateful to Prof. Katsura Kobayashi, Dr. Tak Kunihiro, Dr. Hiroshi Kitagawa, Dr. Tsutomu Ota for their scientific discussions.

I would also like to show my gratitude to my classmates and colleagues Tai Nguyen Truong, Belay Iyasu Getachew, Tsegereda Ayalew Yemer, Feyissa Dejene Hailemariam, Que Dinh Hoang, Wei Zhang, Kucukarslan Nurcan, Tulibako Mwaisuba Tulibonwya, Maya-Liliana Avramescu, Nghiem Van Dao, Potiszil Christian, Yanqing Li, Ivan Pineda Velasco for their lovely friendship.

Last but not the least, I would like to thank my family who are so supportive for both my research work and life, and always stand by me anytime.

## Table of Contents

<b>Abstract</b> .....	i
<b>Acknowledgement</b> .....	iv
<b>List of figures</b> .....	ix
<b>List of tables</b> .....	x iii

### Chapter 1. Introduction

1.1. Highly siderophile elements in the Earth.....	2
1.2. Orogenic peridotite massif.....	2
1.3. Highly siderophile element behavior in mantle tectonites.....	6
1.4. Motivation and aim of this study.....	8

### Chapter 2. Analytical method for measurements of highly siderophile elements in geological reference materials

1. Introduction.....	12
2. Experimental section .....	15
2.1. Reagents and materials.....	15
2.2. Sample decomposition and chemical separation procedures.....	16
2.2.1. Decomposition .....	16
2.2.2. Separation of Os from HSEs.....	17
2.2.3. Desilicification.....	17
2.2.4. Separation and purification of HSEs.....	18
2.2.5. Recovery yield experiment of HSEs.....	18
2.3. Mass spectrometric measurement.....	19

2.3.1.	Ru, Pd, Re, Ir and Pt mass fractions by ICP-MS.....	19
2.3.2.	Os mass fractions and isotope ratios by TIMS.....	20
3.	Results and discussion.....	21
3.1.	Chemical separation of HSEs.....	21
3.1.1.	Removing cationic matrix elements using cation exchange resin AG50W-X12 .....	21
3.1.2.	Secondary purification of Pd-Ir-Pt from Zr and Hf by Ln resin.....	22
3.1.3.	Separation of Ru-Re-Ir-Pt fraction and Pd fraction during Chelex 100 resin.....	23
3.1.4.	Final purification of Ru from Cr during cation exchange resin AG50W-X8.....	24
3.2.	Recovery yield of HSEs, interfering elements, and blank.....	25
3.2.1.	Recovery yield of HSEs in natural samples.....	25
3.2.2.	Elimination of interfering elements.....	25
3.2.3.	Total procedural blanks.....	26
3.3.	HSE mass fractions and Os isotope ratios of reference materials .....	27
3.3.1.	UB-N .....	27
3.3.2.	JP-1.....	28
3.3.3.	MUH-1.....	29
3.3.4.	OKUM.....	29
3.3.5.	TDB-1.....	31
4.	Conclusions .....	32
	Figures.....	34
	Tables.....	46

## Chapter 3. Osmium isotopes and highly siderophile elements in Horoman peridotite massif,

### Japan

1. Introduction.....	57
2. Geological setting and previous studies .....	59
2.1. Geological setting.....	59
2.2. Previous petrological and geochemical significance.....	61
3. Sample description.....	63
3.1. Petrography and petrology.....	63
3.1.1. Massive plagioclase lherzolite.....	63
3.1.2. Massive spinel lherzolite and harzburgite.....	63
3.1.3. Massive dunite.....	64
3.1.4. Thin-layer peridotite.....	64
3.2. Major and trace element compositions and H-Li-O-Sr-Nd-Hf-Pb isotopes.....	64
4. Analytical methods.....	67
4.1. Sample digestion and HSE separation.....	67
4.2. Mass spectrometric measurements.....	67
4.2.1. N-TIMS measurements for Os mass fraction and $^{187}\text{Os}/^{188}\text{Os}$ ratio.....	67
4.2.2. ICP-MS measurements for other HSEs.....	69
4.2.3. Total procedural blank.....	69
4.2.4. External precision of reference material UB-N.....	69
5. Results.....	70
5.1. Sample heterogeneity of peridotites.....	70
5.2. HSE mass fractions.....	70
5.3. Os isotope ratios.....	72

6. Discussions.....	74
6.1. Evaluation of Re-Os model ages.....	74
6.2. HSE abundances and fertility.....	75
6.3. Phase control for Os and Ru fractionations.....	77
6.4. Effect of fluid-rock interaction.....	78
6.4.1. Recent serpentinisation process.....	78
6.4.2. SSH alteration at MOR after melt extraction.....	79
6.4.3. Fluid-rock reaction in the mantle wedge.....	79
6.5. Re-Os model ages for two-step fractionation processes.....	80
6.6. Melt/fluid–rock reaction of one sample dunite.....	81
7. Conclusions.....	82
Figures.....	84
Tables.....	105
Appendix.....	106
<b>References.....</b>	<b>113</b>

## List of figures

Figure

2.1. Workflow diagram for separations and determination of HSE mass fractions and Os isotope ratios developed in this study.....	34
2.2. Photo of borosilicate Carius tube (2.5 mm thick and 200 mm long) (left) and stainless steel jacket with the tube (right) connected to the exhaust post of the laboratory.....	35
2.3. Os final purification by microdistillation.....	36
2.4. Photo of CETAC Aridus II™ Desolvating Nebulizer system.....	37
2.5. $^{186}\text{Os}/^{188}\text{Os}$ , $^{187}\text{Os}/^{188}\text{Os}$ and $^{190}\text{Os}/^{188}\text{Os}$ ratios with 2SD of 0.1-50 ng of DROsS using both static mode ( $10^{11}\Omega$ and $10^{12}\Omega$ resistors) and peaking-jumping mode from this and previous studies.....	38
2.6. Elution profiles of HSEs (synthetic solution) during 1 <sup>st</sup> column using 20 ml of cation exchange resin AG50W-X12.....	39
2.7. Elution profiles of HSEs and interfering elements (synthetic solution) in 3 ml of AG50W-X8 (broken line) and -X12 (solid line). The insert for HSE shows the tailing of Ru, Pd, Re, Ir and Pt eluting from 6 to 12 ml for both X8 and X12.....	40
2.8. Recovery yields of HSEs and interfering elements (Cr, Y, Zr, Cd and Hf) for each column using matrix-containing synthetic solution without (a) and with (b) desilicification. 1: AG50W-X12, 2: Ln resin, 3: Chelex 100, 4: AG50W-X8. For the 3 <sup>rd</sup> column, two fractions were collected, one is the Ru-Re-Ir-Pt cut, and the other is the Pd cut (Figure 1.9). The recoveries shown for 3 <sup>rd</sup> column are: Ru, Re, Ir, Pt, Hf and Cr for the Ru-Re-Ir-Pt cut and Pd, Zr, Y and Cd for the Pd cut.....	41
2.9. Elution profiles of HSEs (reference material TDB-1 with desilicification by HF) during 3 <sup>rd</sup> column using Chelex100 resin: Pd was successfully separated from Zr and Cd.....	42
2.10. Range of total procedural blanks from this study and previous studies, CT: Carius tube, HPA: high pressure asher.....	43
2.11 a-c. HSE mass fractions for reference materials UB-N, JP-1 and TDB-1, respectively; comparison	

with previous studies (error bar: 1SD), CT: Carius tube, CT-HF: Carius tube with post-Os desilicification, HPA: high pressure asher, HPA-HF: high pressure asher with post-Os desilicification. Os data of CT-HF were compiled with Os data of CT in this and previous studies.....	44
2.12. PUM-normalised HSE patterns for reference materials TDB-1, OKUM, UB-N, MUH-1 and JP-1, respectively with and without desilicification by HF from this study. The gray lines denote HSE patterns of DS. The PUM data are from Becker et al. (2006). DS: HF-desilicification.....	45
3.1. Map of regional setting of the Hidaka metamorphic belt and location of the Horoman peridotite massif (Yamamoto et al. 2010).....	84
3.2. Lithologic map of the Horoman peridotite massif. The map is modified after Ranaweera et al. (2018).....	85
3.3. Primitive mantle normalised REE patterns from previous literatures. Primitive mantle data: McDonough and Sun (1995). .....	86
3.4. Lithological variation of trace elements and isotopic data for TLP. The thickness from bottom to top is 1.95m. The broken line is boundary of T-TLP and B-TLP classified in this study. Data are from Malaviarachchi et al. (2008, 2010) and Ranaweera et al. (2018). Black circle: plagioclase lherzolite; black square: harzburgite; open circle: gabbro.....	87
3.5. CI chondrite normalised REE patterns of Horoman peridotite samples. CI chondrite data: McDonough and Sun (1995). Data are from Malavirachchi et al. (2008) and unpublished data for dunite.....	88
3.6. Plot of Yb vs. Al <sub>2</sub> O <sub>3</sub> in Horoman peridotite samples.....	89
3.7. Oxygen, Li and H isotopic compositions, and H <sub>2</sub> O concentrations of the Horoman peridotite samples (Ranaweera et al. 2018). Symbols are the same as in Figure 3.6. (a) Oxygen and Li isotope compositions. The range of the plot displayed in (b) is shown by the dashed line. (b) Oxygen and Li isotope compositions of the Horoman samples. (c) Hydrogen isotope compositions and H <sub>2</sub> O concentrations of the Horoman peridotites.....	90
3.8. Primitive upper mantle normalised patterns of Horoman peridotite samples. PUM data: Becker et al. (2006) for HSEs and McDonough and Sun (1995) for S (primitive mantle composition). Grey	

region: 1 $\sigma$ range of the estimated primitive upper mantle.....	91
3.9. Lithology diagram of the HSE and S abundances, Re/Os, Ru/Ir and <sup>187</sup> Os/ <sup>188</sup> Os ratios of thin-layer peridotites from top to bottom.....	92
3.10. Plots of HSEs vs. Yb in Horoman peridotite samples. PM is the 1 $\sigma$ range of primitive mantle value for Yb (McDonough and Sun, 1995) and primitive upper mantle value of Becker et al. (2006). Error bars in each sample is determined by 1 $\sigma$ external precision of reference samples. Symbols are the same as in Figure 3.6.....	93
3.11. Plots of HSEs vs. S in Horoman peridotite samples. PM is the 1 $\sigma$ range of primitive mantle value for S (McDonough and Sun, 1995) and primitive upper mantle value of Becker et al. (2006). Error bars in each sample is determined by 1 $\sigma$ external precision of reference samples. Symbols are the same as in Figure 3.6.....	94
3.12. Re-Os isochron diagram for Horoman peridotite samples. T <sub>MA</sub> ages are shown as solid lines; T <sub>RD</sub> ages are shown as horizontal dashed lines. ....	95
3.13. Plots of fertility indicator Al <sub>2</sub> O <sub>3</sub> vs. <sup>187</sup> Os/ <sup>188</sup> Os for the massive (left) and thin-layer (right) peridotites. Three samples of T-TLP (HR+55, +20, +12) are plotted in massive peridotite diagram (left).....	96
3.14. Plots of Os/Ir vs. Yb (a), Ru/Ir vs. Yb (b) and Os/Ir vs. $\delta^7$ Li (c), Ru/Ir vs. $\delta^7$ Li (d) for Horoman peridotite samples. Symbols are the same as in Figure 3.6.....	97
3.15. Plots of Re/Os vs. Re (a), Re/Os vs. Os (b), Re vs. Os (c), Re/Ir vs. Re (d) for Horoman peridotite samples. Blue and red indicate the low-Os and high-Os types of peridotites. Symbols are the same as in Figure 3.6.....	98
3.16. Re-Os isochron diagrams of Horoman peridotite samples. Blue and red indicate the low-Os and high-Os types of peridotites. Symbols are the same as in Figure 3.6.....	99
3.17. (a) Plot of modal abundances vs. H <sub>2</sub> O contents; (b) H <sub>2</sub> O vs. Ru/Ir, and (c) H <sub>2</sub> O content vs. Os/Ir of Horoman peridotite samples. The data for serpentine abundances and H <sub>2</sub> O contents are from Ranaweera et al. (2018). Symbols are the same as in Figure 3.6.....	100

3.18. Initial $^{87}\text{Sr}/^{86}\text{Sr}$ ratios of Horoman peridotite samples at 154 Ma (a and b) and 1 Ga (c and d). The Sr isotopic compositions of the upper mantle is between E-DMM and D-DMM of Workman and Hart (2005). The ranges of Os/Ir and Ru/Ir ratios in the upper mantle is $\pm 1\sigma$ range of PUM after Becker et al. (2006). Symbols are the same as in Figure 3.6.....	101
3.19. Re-Os isotope model calculation for estimation of the two-steps fractionation processes. The first step was melt extraction from the PUM composition at 1.4 Ga, the age of initial melt extraction was assumed by $T_{\text{RD}}$ of the harzburgite samples. The secondary Re/Os fractionation was calculated at (a) 0.3 Ga when TLP were reacted with MORB-like melt and (b) 0.15 Ga when the fluid metasomatism was occurred for EP-MSP in the mantle wedge.....	102
3.20. Pb isotopic compositions of the massive and thin-layer peridotites. The global MORB data (small grey circles) are from the PetDB Database.....	103
3.21. The classification of B-TLPs based on the HSE abundances and Re-Os isotope system.....	104
A1. Photo of the amplifier assembly of TRITON Plus.....	106
A2. The gain factors of the three $10^{13}\Omega$ amplifiers at negative mode from this study.....	107
A3. Comparison of analytical precision of $^{187}\text{Os}/^{188}\text{Os}$ ratios measured by different sources.....	108
A4. Comparison of $^{187}\text{Os}/^{188}\text{Os}$ ratios using various amounts of the DROsS obtained by TRITON and TRITON Plus with different amplifiers. Green dot: TRITON data; Black dot: TRITON Plus data.....	109

## List of Tables

### Table

2.1. Separation scheme for Ru-Pd-Ir-Re-Pt purification.....	46
2.2. ICP-MS operating conditions.....	47
2.3. Potential isobaric and polyatomic interferences for HSEs.....	48
2.4. Collection schemes of Os isotope measurement for the static mode and peak-jumping mode...	49
2.5. Potential polyatomic interferences on the mass spectrum of $\text{OsO}_3^-$ during N-TIMS measurement.....	50
2.6. Measurement of $^{17}\text{O}/^{16}\text{O}$ and $^{18}\text{O}/^{16}\text{O}$ ratios during each analytical session.....	51
2.7. Distribution coefficient ( $K_d$ ) of HSEs and interfering elements in Ln resin and Chelex 100 determined from this study.....	52
2.8. Ratios of interferences intensities relative to the measured intensities of HSE isotope masses (cps/cps in parts per million) during ICP-MS measurement.....	53
2.9. HSE mass fractions ( $\text{ng g}^{-1}$ ) of UB-N, JP-1 and MUH-1 from this study.....	54
2.10. HSE mass fractions ( $\text{ng g}^{-1}$ ) of OKUM and TDB-1 from this study.....	55
3.1. HSE mass fractions ( $\text{ng g}^{-1}$ ), $\text{Al}_2\text{O}_3$ contents (wt. %) and Os model ages of Horoman peridotite samples from this study.....	105
A1. Sequence of gain calibration.....	110
A2. Total procedural blanks (ng), HSE mass fractions ( $\text{ng g}^{-1}$ ) and Os isotope ratios of UB-N from this study.....	111
A3. Relative percentage difference of duplicate Horoman peridotite samples from this study.....	112

# **Chapter 1: Introduction**

### **1.1. Highly siderophile elements in the Earth**

Abundance and fractionation behavior of the highly siderophile elements (HSEs: Ru, Rh, Pd, Re, Os, Ir, Pt, and Au) and their isotope systems (e.g.,  $^{187}\text{Re}$ - $^{187}\text{Os}$  and  $^{190}\text{Pt}$ - $^{186}\text{Os}$  isotope systems) play an important role in constraining origin and evolution of the Earth's mantle. The HSE abundances of silicate Earth inferred from the fertile peridotites are much higher than those can be expected by metal-silicate partitioning, under the assumption of bulk Earth as a chondritic composition (e.g., Mitchell and Keays 1981, Morgan et al. 1981). The excess HSE abundances, together with their broadly chondritic abundance ratios in highly to intermediately refractory elements, have been generally explained by the late accretion model, i.e., a late veneer of chondritic material after the segregation of the core (e.g., Chou 1978). However, the non-chondritic HSE concentration ratios are reported from numbers of orogenic peridotites (e.g., Pattou et al. 1996) and abyssal peridotites (e.g., Snow and Schmidt 1998). One model explains that an addition of outer-core materials back into the mantle (Snow and Schmidt 1998) for the non-chondritic HSE characteristics, but it remains highly controversial. Earth's mantle have been experienced multiple processes such as partial melting, degassing, metasomatism, alteration, and metamorphism. Because of the divergent chemical behavior of HSEs between metal, sulfide, silicates, and fluid during these processes, it is difficult to account for the non-chondritic HSE characteristics in the Earth's mantle simply.

### **1.2. Orogenic peridotite massif**

Tectonically emplaced mantle rocks, such as orogenic peridotite massif, ophiolites, and abyssal peridotites, provide a principle constraint on the composition and multiple processes in the Earth's upper mantle. These mantle rocks were tectonically exhumed from the upper mantle and occur : (1) as dispersed ultramafic bodies, a few meters to kilometers in size, in suture zones and mountain belts (i.e., the Alpine or orogenic peridotite massif) (e.g., De Roever 1957, Den Tex 1969); (2) as the lower

ultramafic section of large (tens of kilometers) ophiolite or island arc complexes, obducted on continental margins (e.g., Coleman 1971, Boudier and Coleman 1981); (3) from the oceanic mantle that were dredged on the ocean floor or recovered from drill cores (i.e., abyssal peridotite) (e.g., Bonatti et al. 1974, Prinz et al. 1976) and so forth.

Compared to mantle xenoliths, however, the tectonically emplaced mantle rocks have a disadvantage that their original geodynamic setting is somehow not exactly known and their significance is more or less a subject of speculation. For example, the provenance of orogenic lherzolite massifs (subcontinental lithosphere vs. upwelled asthenosphere) is still debated (e.g., Menzies and Dupuy, 1991). Additionally, the mantle structures and mineralogical compositions of tectonically emplaced mantle rocks maybe disturbed by deformation and metamorphic processes during shallow upwelling, exhumation and tectonic emplacement. For example, some garnet peridotites may experience very complicated evolutions. They were first buried in the stability of garnet peridotites, and in greater than 150 km depths; later on, they were exhumed to the surface, dragged by buoyant crustal rocks (e.g., Green et al. 1997, Brueckner and Medaris 2000). Nevertheless, some peridotite massifs are sufficiently well preserved to allow the observation of structural relationships between mantle lithology, which are much larger than the sampling scale of mantle xenoliths. These massifs are able to provide the observations and evaluations of the scale of mantle heterogeneity and the chronological mantle processes, such as vein injection, melt-rock reaction, and deformation. Detailed studies of such as orogenic peridotite massif on a centimeter to kilometer scale provide valuable insights into melt transfer mechanisms, such as melt flow in lithospheric vein conduits or wall rock reactions (Bodinier et al. 1990), melt extraction from mantle source via channeled porous flow (Kelemen et al. 1995) and so forth.

Orogenic peridotite are distributed along the mountain belts, representing tectonically emplaced mantle rocks, rather than crystallised ultramafic magmas or olivine-rich cumulates. They are generally characterised by the predominance of lherzolites, equilibrated in any of the garnet-, spinel- or plagioclase-peridotite facies defined by O'Hara (1967). The orogenic peridotites vary in size from small blocks (~several meters) to large ultramafic exposures (up to ~hundreds km<sup>2</sup>), forming the main body of overthrust tectonic setting (e.g., the Ronda massif, southern Spain). They are distinguishable from ophiolitic peridotites that orogenic peridotites are unrelated to oceanic rock associations. However, exceptions for some lherzolites, which contain shallow intrusive rocks interpreted as embryonic ocean crust, are presumably considered to be intermediate between the "true" orogenic peridotite massif and the "lherzolite subtype" of the ophiolites (e.g., the Lanzo plagioclase lherzolite massif, Italian Apls). The orogenic massifs are generally associated with platform sediments or continental rocks, recording extreme metamorphic conditions, which ranges from high temperature (HT) at intermediate (IP) or low pressure (LP) to high pressure (HP) or ultrahigh pressure (UHP) at variable temperature conditions. The HT metamorphism were discovered such as Beni Bousser (northern Morocco) and Ronda massifs. On the other hand, some orogenic peridotites are associated with HP to UHP area, such as Bohemian Massif in Central Europe (e.g., Tubia and Cuevas 1986, Bodinier et al, 1991, Brueckner and Medaris 2000, Medaris et al. 2005).

The lherzolites of the orogenic massifs are mostly fertile (>10% clinopyroxene). Subordinate rock types include refractory peridotite (i.e., clinopyroxene-poor lherzolite, harzburgite, and/or dunite), and mafic layers such as mafic granulite clinopyroxenite and websterite. The proportion of refractory peridotites in orogenic massif is typically up to ~30-40 vol. %, whereas the mafic layers are generally <5 vol. %. Several orogenic peridotites underwent secondary processes, stemming from the segregation and migration of partial melts or from the melt/fluid-peridotite interactions (e.g., Bodinier

et al. 1988). Some peridotite bodies were almost entirely metasomatised by melt/fluid of mantle, subducted slab, or crustal origin (e.g., Cawthorn 1975, Rampone and Morten 2001). Based on their principal petrologic facies and P-T trajectory before the exhumation, the orogenic peridotite massifs are subdivided into three main groups: (1) The HP/UHP massif, which is mainly equilibrated at HP or UHP in the stability field of garnet peridotites; (2) The IP massif, which is mostly equilibrated at IP in the stability field of spinel peridotites; (3) The LP massif, which is featured by exhumation at very shallow levels in extensional setting, ending in the tectonic denudation of serpentinised mantle peridotites on the seafloor.

Many previous studies have reported major and trace elements data of orogenic, ophiolitic and abyssal peridotites. In spite of their different provenances (e.g., subcontinental lithosphere, mantle wedge, or oceanic mantle and so forth), most tectonically emplaced rocks show coherent covariation trends for major elements, which reflect their variable modal compositions between a fertile end-member (i.e., comparable to the pristine mantle compositions) and a refractory end-member (McDonough and Sun, 1995). The fertile compositions are mainly in the orogenic lherzolite massifs (maximum at ~55-60% for modal olivine, and ~3.0-3.5 wt. % for  $\text{Al}_2\text{O}_3$  contents), whereas refractory compositions are mostly in ophiolitic and abyssal peridotites (maximum at ~70-80% for modal olivine, and ~0.5-1.5 wt. % for  $\text{Al}_2\text{O}_3$  contents). Among rare earth element (REE) data, the heavy REEs in mantle peridotites are negatively correlated with Mg and positively correlated with Al. Most tectonically emplaced mantle rocks show a well-defined Yb content vs.  $\text{Al}_2\text{O}_3$  content, which is classically ascribed to variable degrees of melt extraction. However, any secondary processes (e.g., melt-rock reactions, melt redistributions, or refertilisations) may also lead to the heavy-REE variations. In contrast, the light-REEs show scattered variations plotting against  $\text{Al}_2\text{O}_3$  content. Although the orogenic lherzolites in general, seem to be more enriched in light-REEs than the ophiolitic and abyssal peridotites, the light-

REE depleted fertile orogenic lherzolites relative to chondrite have been widely explained as depleted mid-ocean ridge basalt (MORB) mantle (DMM), representing the MORB source (e.g., Hartmann and Wedepohl 1993). They were interpreted as the mantle residues which had very small degrees (<3 %) of melt extraction from a pristine mantle source (i.e., primitive mantle) (e.g., Menzies et al. 1977). Moreover, among the orogenic peridotites, the metasomatised samples are more enriched in light-REEs than the unmetasomatised samples. For the lithophile trace elements, the highly incompatible elements (i.e., Rb, Cs, Ba, Nb, Ta, Th and U) are strongly scattered on the Al covariation diagrams, and the variations could be dominantly controlled by peridotite provenances.

### **1.3. Highly siderophile element behavior in mantle tectonites**

The mantle tectonites (i.e., tectonically emplaced mantle rocks) are able to provide a range of geological environments with regard to their origin and evolutions. Numerous studies have obtained and observed the behavior of Os isotopic compositions and/or HSE abundances in peridotites. Previous studies either focused on large-scale geochemical and isotopic variations, or on grain-size compositional differences, both of which have significantly improved the understanding of the mechanism that the fractionation of HSEs in the mantle at different spatial scales. Moreover, the Os isotope system and Re-Os model ages are able to directly date the melting process of these mantle tectonites, and provide diverse insights into the efficacy of mixing and melting processes in the Earth's mantle as a function of time and space.

The value of the strongly chalcophile elements, including the HSEs in the study of processes in the Earth's mantle originates from the fact that the abundances of these elements are dominantly controlled by diverse, trace sulfides and alloys which can be strongly affected by melting and metasomatic processes in different ways from the host minerals of the lithophile elements. For

instances, the large levels of partial melting in the mantle, coupled with melt removal, typically leading to the residual mantle which is moderately to strongly depleted in incompatible HSEs (i.e., Pt, Pd and Re), by contrast, melt removal can cause minor enrichment of the compatible HSEs (i.e., Os, Ir and Ru), relative to the fertile mantle. The contrasting fractionation behavior of the HSEs results in the generations of characteristic siderophile element signatures, and provides a robust tool to constrain the extent and timing of the processes involved. A general observation is that harzburgites have similar abundances of Os, Ir and Ru as lherzolites, whereas, the abundances of Pt, Pd and Re of harzburgites are typically much lower compared to lherzolites. Previous studies have pointed out that the main host phase of HSEs in lherzolites at high temperatures should be sulfides. Hence, the stronger depletion of Pt, Pd, Re and sulfur in harzburgites compared to lherzolites possibly reflects the consumption of sulfide in peridotites during higher degrees of melting process (e.g., Barnes et al. 1985, Morgan 1986).

The divergence in the evolution of Os isotopic compositions in the Earth's mantle is the basis of both Re-Os mantle model age ( $T_{MA}$ ) and Re depletion model age ( $T_{RD}$ ) (Shirey and Walker 1998, Rudnick and Walker 2009).  $T_{MA}$  are based on the measured  $^{187}\text{Re}/^{188}\text{Os}$  ratio of a mantle rock, and the Os isotopic composition is able to be projected backward in time from that measured to a primitive upper mantle evolution trajectory to obtain a model age. If Re was added prior to or during melt removal, the model age will be older than the true age of melt depletion. By contrast, a  $T_{RD}$  age is based on the assumption that all Re in the mantle rock was removed during melt depletion, as such, it normally provides a minimum age of melt depletion. Parent and daughter elements for other isotope systems (e.g., Rb-Sr, Sm-Nd, U-Pb isotope systems) behave incompatible during mantle melting, being mainly controlled by silicate phases. In contrast, Re behaves as a moderately incompatible element, whereas, Os is highly compatible during melting (Morgan, 1986). The loss of Re and retention of Os in the mantle residuals during partial melting leads to a decrease of the Re/Os ratio of the residual mantle,

and subsequent retardation in the growth of  $^{187}\text{Os}/^{188}\text{Os}$  ratio in the residuals, compared to mantle that has not been experienced melt removal (e.g., Walker et al. 1989). On the contrary, the higher concentrations of Re in the crust, relative to the Earth's mantle, coupled with the lower concentrations of Os in the crust, leading to the very high Re/Os ratio and increase  $^{187}\text{Os}/^{188}\text{Os}$  ratio in the Earth's crust. Depending on the tectonic setting, some processes may or may not influence the model ages. These secondary processes include serpentinisation, sulfide breakdown, refertilisation and melt-rock reaction and so forth (Rudnick and Walker 2009). For example, melt-rock reaction in the mantle commonly associated with melting, is typically zero age with regard to melting, and should not normally affect the model age recorded for the melting process. Conversely, melt percolation and melt reaction in the continental lithosphere may occur long after melt depletion event, which has the potential to disturb the true age (Rudnick and Walker 2009). Nevertheless, both model ages play an important role on the constrains on the timing of melt extraction process in the Earth's mantle.

#### **1.4. Motivation and aim of this study**

Horoman peridotite massif which is located in the low-pressure high-temperature type Hidaka metamorphic belt at the southern tip of Hokkaido in northern Japan, is presumably suited for the investigation of HSE behavior in the upper mantle, because it is the least altered peridotite massif in the world and preserves the unique chemical and isotopic compositions, which may record the multiple mantle processes (e.g., Takazawa et al. 2000, Yoshikawa and Nakamura 2000, Malaviarachchi et al. 2008). The Horoman massif exhibits a well-developed compositional layering on a scale of centimeters to several hundred meters, which is divided into two stratigraphic zones: the Upper Zone where the layers are thinner and mafic layers are more abundant, and the Lower Zone where layers define lithological sequences of ~100 to 500 m (Niida, 1984). The Main Harzburgite-Lherzolite (MHL) suite as the major part of the Horoman massif, consists of plagioclase lherzolite, spinel

lherzolite and harzburgite, which have been interpreted as the result of variable degrees of melt extraction from the MORB-source mantle (Frey et al. 1991, Takahashi 1991, Takazawa et al. 1996, Yoshikawa and Nakamura 2000, Malaviarachchi et al. 2008).

The uniqueness of the Horoman peridotite is that the highly unradiogenic Pb isotopic compositions were discovered among so far reported peridotites on the Earth, which is the key information to solve the Pb paradox. Malaviarachchi et al. (2008) suggested that the least radiogenic Pb isotopic compositions with the Pb enrichment in plagioclase lherzolites could be caused by hydrothermal processes after the melt extraction at the mid-ocean-ridge system (MORs) (Kelemen et al. 2007). Ranaweera et al. (2018) also suggested that the positive correlations among H, B and Cl contents and positive correlation of S with Pb contents in these samples might be caused by ancient sub-seafloor hydrothermal (SSH) alteration.

The HSE abundances have been analysed for 6 samples of Horoman peridotites (Rehkämper et al. 1999), and Os isotopic compositions were analysed for 20 samples (Saal et al. 2001). The  $^{187}\text{Os}/^{188}\text{Os}$  ratios of most Horoman samples so far reported by Saal et al. (2001) ranged from 0.1158 to 0.1283, which were similar range as peridotites reported in other localities (e.g., Reisberg et al. 1991, Reisberg and Lorand 1995), however, some samples extended to higher  $^{187}\text{Re}/^{188}\text{Os}$  ratios than that of PUM. Therefore, based on higher Pd/Ir and Pt/Ir ratios relative to chondrite (Rehkämper et al. 1999) and suprachondritic  $^{187}\text{Re}/^{188}\text{Os}$  ratios (Saal et al. 2001), both studies suggested that it might be the result of a refertilisation process of a depleted peridotite by sulfides derived from percolating magmas or involving mixing of a MORB-like source.

These interpretations based on previous HSE data somehow contradict with the geochemical studies, which have been basically interpreted by the behavior of lithophile elements (Yoshikawa and Nakamura 2000, Malaviarachchi et al. 2008, Ranaweera et al. 2018). In this thesis, therefore, the HSE abundances and  $^{187}\text{Os}/^{188}\text{Os}$  ratios of the Horoman peridotite samples were analysed, among which major- and trace- element abundances, Sr-Nd-Hf-Pb isotope systems, elemental abundances of H, B, Cl, F, S, and isotopic compositions of H, Li, O have been reported (Malaviarachchi et al. 2008, 2010, Ranaweera et al. 2018). Based on these comprehensive datasets, I will further evaluate the genesis and evolution processes of Horoman peridotite samples, such as the hydrothermal alteration, melt-rock interaction, and/or other unrevealed processes as a function of time and space.

In order to obtain accurate and precise HSE data for the study of Horoman peridotite samples, the analytical method for the measurements of HSE mass fractions and Os isotopic compositions was developed in this study. As terrestrial rock samples contain extremely low HSE abundances (typically  $< \text{a few ng g}^{-1}$ ), relative to major and trace elements (e.g., Cr, Y, Zr, Hf, Cd, Mo and W, as potential interfering elements for HSE measurements by ICP-MS), the purification procedure becomes a prerequisite and necessity. A newly developed purification procedure of the HSEs for geological samples, using a cation exchange resin (AG 50W-X12) and three additional purification steps (i.e., Eichrom-Ln resin, Chelex100 resin and cation exchange resin AG 50W-X8) was presented in this thesis. When using this method, the ratios of the interferences intensities relative to the measured intensities of HSE isotope masses:  $\text{CrO}_3^+/\text{Ru}^+$  (101),  $\text{YO}^+/\text{Pd}^+$  (105),  $\text{Cd}^+/\text{Pd}^+$  (106),  $\text{ZrO}^+/\text{Pd}^+$  (106),  $\text{HfO}^+/\text{Ir}^+$  (193) and  $\text{HfO}^+/\text{Pt}^+$  (194,195), were reduced by less than a few hundred parts per million. Hence, this purification procedure allows the accurate and precise measurements of HSEs without interference correction for geological samples.

**Chapter 2: Analytical method for measurements of highly siderophile elements in geological reference materials**

## 1. Introduction

Highly siderophile elements (HSEs) are used as important geochemical tracers for understanding fundamental processes such as planetary differentiation, core segregation, late accretion, core-mantle interaction, meteorite impacts, metallogenesis and others. (e.g., Brandon et al. 1999, 2006, Becker et al. 2001a, 2006, Horan et al. 2003, Brandon and Walker 2005, Dale et al. 2012a). For example, the abundances of HSE in the terrestrial mantle are used to assess multi-stage melting process or metasomatic interactions. In addition, the Re-Os and Pt-Os isotope systems, in some instances, can be used to place chronological constraints on when these processes occurred. HSEs are also used as a good tracer for marine and environmental sciences. For example, hydrothermal enrichments of HSEs have been suggested for different anomalies concentrations in sediments, Pd and Pt are more soluble in low and intermediate temperatures while Ru, Rh, Os and Ir are the least soluble (Sawlowicz, 1993). Recent development of analytical instruments employing thermal ionisation mass spectrometry (TIMS) and inductively coupled plasma mass spectrometry (ICP-MS) enables to determine the sub-ng g<sup>-1</sup> level of HSEs in geological samples. Although numerous analytical methods for HSEs have been developed, further improvements of purification procedures to obtain highly precise and accurate data employing TIMS and ICP-MS have been reported in recent years (e.g., Jarvis et al. 1997a, Rehkämper and Halliday 1997, Ely et al. 1999, Pearson and Woodland 2000, Meisel and Moser 2004a, b, Qi et al. 2004, Shinotsuka and Suzuki 2007, Savard et al. 2010, Fischer-Gödde et al. 2011, Ishikawa et al. 2014, Li et al. 2014, 2015, Chu et al. 2015a, Day et al. 2016, Ren et al. 2016). Quantitative measurements of HSEs is hampered by the following: (1) extremely low abundances (typically < a few ng g<sup>-1</sup>) in terrestrial rock samples, (2) achieving full sample-spike equilibrium without losing the volatile OsO<sub>4</sub>, (3) sample heterogeneity caused by the nugget effect, (4) relatively high contribution of procedural blanks relative to the low HSE mass fractions, and (5) incomplete removal of matrix and isobaric and polyatomic interfering elements.

Although there exist several analytical methods for the sample digestion and purification methods for HSE analysis, it seems that each method has its advantages and disadvantages. Among all digestion methods ( Table 2.1), the Carius tube (CT) method coupled with isotope dilution (ID) method using inverse aqua regia was employed by most laboratories (e.g., Becker et al. 2006, Luguët et al. 2007, Shinotsuka and Suzuki 2007, Puchtel et al. 2008, Qi and Zhou 2008, Ishikawa et al. 2014, Li et al. 2014), because (1) it provides much lower and better constrained procedural blank levels compared to high and irreproducible Re and Os blank by alkaline fusion method ( Morgan and Walker 1989), or high Os blank by NiS fire assay (Hoffman et al. 1978), (2) it is capable of determination for both HSE concentrations and Os isotope ratios from the same sample aliquot as well as avoiding losses of volatile OsO<sub>4</sub>. However, one major potential limitation of the CT method is that inverse aqua regia cannot dissolve silicates and oxide minerals containing a small fraction of HSEs. To obtain complete or high recovery of HSEs from natural samples using the CT method, a desilicification step is necessary by adding HF before or after inverse aqua regia digestion, was applied and its effectiveness reported for mafic rock samples (Dale et al. 2009, Meisel et al. 2009, Ishikawa et al. 2014, Li et al. 2015, Day et al. 2016). However, some analytical problems arise when applying the desilicification process; the abundances of interfering elements and procedural blanks of HSEs in the desilicified sample elution were much higher than in the non-desilicified sample elution (Day et al. 2016). Ishikawa et al. (2014) reported that there were no significant differences for interfering elements and procedural blanks between desilicified and non-desilicified sample elutions, and also suggested the post-CT desilicification because (1) there is no resolvable effect on Os concentration regardless of whether HF digestion was before or after aqua regia attack; (2) the usage of HF will cause corrosion of the CT and make it explosive during continuous aqua regia digestion. However, Day et al. (2016) pointed out that using an HF digestion-step is not required for intraplate basalts, even the release of additional Re by a second-stage HF digestion would result in measured Re/Os, which does not reflect the ratio in

equilibrium with measured  $^{187}\text{Os}/^{188}\text{Os}$ . The procedure of desilicification in some extent depends on the components of natural samples and the purpose for isotope analysis study. Moreover, Ishikawa et al. (2014) discussed the potential problem of the Cr oxide species for the measurement of Ru. Therefore, improvement of the purification procedure is a prerequisite for accurate HSE measurement results for desilicified samples.

To separate HSEs from the other elements in geological samples, previous studies have employed either an anion exchange resin (Jarvis et al. 1997b, Pearson and Woodland 2000, Meisel et al. 2001, Ishikawa et al. 2014, Chu et al. 2015a) or a cation exchange resin (Jarvis et al. 1997a, Ely et al. 1999, Meisel et al. 2003a, 2004a, b, Shinotsuka and Suzuki 2007, Fischer-Gödde et al. 2011, Li et al. 2014). For the anion exchange chromatography, anionic HSE chloro-complexes can be retained using a small amount of resin, as most of the cationic major elements pass through the column. However, the major drawback of this approach has been the difficulty of obtaining quantitative elution and complete recovery of all HSEs from the resin, due to their strong affinity to the resin (Jarvis et al., 1997b). Cation exchange resins have the advantage of high recovery of HSEs, compared to anion exchange resin, but a larger volume of resin is required. The major element matrix cations can be removed using both types of resin. These ion-exchange methods are, however, unable to completely separate interfering elements (e.g., Cr, Y, Zr, Hf, Cd, Mo and W) from HSEs in mass spectrometric measurement. Therefore, several previous studies employed one or more purification steps (Shinotsuka and Suzuki 2007, Ishikawa et al. 2014, Li et al. 2014, Chu et al. 2015a). In geological samples, the concentrations of the interfering elements are considerably higher than those of the HSEs, making it difficult to sufficiently purify the HSEs to avoid the interferences. Therefore, isobaric and polyatomic interference corrections have been generally applied in mass spectrometric measurements. (e.g., Ely et al. 1999, Pearson and Woodland 2000, Shinotsuka and Suzuki 2007, Ishikawa et al. 2014, Li et al. 2014).

In this study, we present a newly developed purification procedure for HSEs from geological samples using a cation exchange resin (AG 50W-X12) and three additional purification steps (i.e., Eichrom-Ln resin, Chelex100 resin and cation exchange resin AG 50W-X8), following CT decomposition, Os extraction, and HF desilicification. This procedure allows the measurements of HSEs without interference correction. Using this procedure, the Ru, Pd, Re, Ir, Pt and Os mass fractions and  $^{187}\text{Os}/^{188}\text{Os}$  ratios of reference materials in ultramafic to mafic compositions were evaluated.

## **2. Experimental section**

All experiments in this study were performed at the Pheasant Memorial Laboratory for Geochemistry and Cosmochemistry (PML), Institute for Planetary Materials, Okayama University at Misasa, Japan (Nakamura et al. 2003).

### **2.1. Reagents and materials**

High purity water ( $\geq 18.2 \text{ M}\Omega \text{ cm}$ ) was prepared using a Milli-Q system (Merck Millipore, Darmstadt, Germany). For the sample decomposition and purification, TAMAPURE-AA-10 grade 38% HF and 68%  $\text{HNO}_3$ , TAMAPURE-AA-100 grade 30% HCl (Tama Chemicals, Kawasaki, Japan), infinity pure-grade  $\text{CCl}_4$  (Wako Pure Chemical Industries, Osaka, Japan), and analytical grade 48% HBr (Kanto Chemical, Tokyo, Japan) were utilised. The HBr was further purified twice by distillation, as in Makishima and Nakamura (2001). We employed a HSE mix spike solution containing  $^{101}\text{Ru}$ ,  $^{105}\text{Pd}$ ,  $^{185}\text{Re}$ ,  $^{189}\text{Os}$ ,  $^{191}\text{Ir}$  and  $^{195}\text{Pt}$  enriched isotopes prepared as described by Nakamura et al. (2003). Mass fractions of the HSEs in the mixed spike solution were calibrated by isotope dilution methods using the Precious Metals plasma standard solution from Specpure<sup>®</sup> (Alfa Aesar, Lancashire, UK; the certified concentrations:  $100.0 \pm 0.5 \mu\text{g ml}^{-1}$  of Au, Ir, Os, Pd, Pt, Re, Rh and Ru, are directly traceable to the NIST SRMs). The geological reference materials UB-N (serpentinite, CRPG), JP-1 (harzburgite,

GSJ), TDB-1 (diabase, CCRMP), MUH-1 (harzburgite, IAG) and OKUM (komatiitic basalt, IAG) were analysed in this study. The ultramafic reference materials UB-N and JP-1 from purchased batches were further pulverised in our laboratory. Of five reference materials, MUH-1 and OKUM are new ultramafic reference materials prepared by *IAGeo limited*, which have been distributed for interlaboratory comparisons of HSE concentrations and Os isotopic compositions (Meisel et al. 2013, Meisel and Horan 2016). The major and trace elements were already certified via *IAGeo limited* (Burnham et al. 2010).

Powdered samples were decomposed with inverse aqua regia in a borosilicate CT (2.5 mm thick and 200 mm long, Figure 2.2), and modified as described by Shirey and Walker (1995). Before decomposition, the CT was washed in detergent (TMSC, Tama Chemicals, Kawasaki, Japan), subsequently rinsed with water and a mixture of 9.5 mol l<sup>-1</sup> HCl (4 ml) and 16 mol l<sup>-1</sup> HNO<sub>3</sub> (8 ml) was added. The CT was flame-sealed, and finally washed at 240 °C for ~48 h, following the procedure described by Day and Walker (2015).

## **2.2. Sample decomposition and chemical separation procedures**

### **2.2.1. Decomposition**

The workflow of the sample decomposition and subsequent chemical purification procedures is shown in Figure 2.1. Approximately 1 g of powdered sample, adequate amounts of HSE mixed spike solution, 2.5 ml of 9.5 mol l<sup>-1</sup> HCl and 7.5 ml of 16 mol l<sup>-1</sup> HNO<sub>3</sub> were loaded into a pre-washed CT, which was then flame-sealed. To reduce the vapor pressure of the reagents and to prevent Os loss, the CT was kept at ~ -90 °C during the whole procedure. The CT was installed into a stainless steel jacket (Figure 2.2), and heated for 72 h at 240 °C. The stainless steel jacket was connected to the exhaust post of the laboratory, to prevent leakage of any gas into the oven, in the event that CT was compromised during

heating.

### **2.2.2. Separation of Os from HSEs**

After cooling the CT, the supernatant solution was transferred into a PFA vessel (25 ml vol.). Osmium was extracted from the inverse aqua regia by adding 3 ml of  $\text{CCl}_4$  and shaking the vessel (Cohen and Waters 1996, Shen et al. 1996). To achieve high recovery of Os, this process was repeated three times. Then, 4 ml of  $8.8 \text{ mol l}^{-1}$  HBr was added to the  $\text{CCl}_4$  solution, and this solution was left at room temperature overnight to back-extract Os into the HBr. The HBr solution was transferred into the PFA vial (7 ml vol.), and dried at  $100 \text{ }^\circ\text{C}$ . Finally, Os was purified by a microdistillation method (Birck et al. 1997), which used a conical PFA vial loaded with  $20 \text{ }\mu\text{l}$  of  $\text{H}_2\text{SO}_4\text{-CrO}_3$  solution (8% m/v of  $\text{CrO}_3$  solution in  $12 \text{ mol l}^{-1}$   $\text{H}_2\text{SO}_4$ ). The conical vial was rapidly and tightly closed in the upside down position, and wrapped in aluminum foil with the exception of a hole at the top of the vial (Figure 2.3). The vial was then heated on hot plate at about  $80 \text{ }^\circ\text{C}$  for 3 h. Keeping temperature homogenous is very important, if the temperature is higher than  $80 \text{ }^\circ\text{C}$ , some of the Cr solution may be transferred to the HBr solution, while if the temperature is much lower than  $80 \text{ }^\circ\text{C}$ , the recovery of distillation of Os decreases.

### **2.2.3. Desilicification**

The Os-extracted inverse aqua regia solution, with or without an insoluble residue, was used for quantitative measurements of Ru, Pd, Re, Ir and Pt. For the desilicification method, the residue in the CT was mixed with the Os-extracted inverse aqua regia solution in a PFA vessel (25 ml vol.), and then centrifuged. After removing the supernatant solution, the residue was digested in 5 ml of  $20 \text{ mol l}^{-1}$  HF. This HF solution and the supernatant solution were dried at  $120 \text{ }^\circ\text{C}$ . Both fractions were then again dissolved with  $6 \text{ mol l}^{-1}$  HCl and dried at  $120 \text{ }^\circ\text{C}$ , repeating this procedure several times. Finally, the

two solutions were mixed and dried down at 100 °C. For the non-desilicification method, only the Os-extracted inverse aqua regia solution was used for analysis.

#### **2.2.4. Separation and purification of HSEs**

Purification of HSE bearing solution from the matrix elements and interfering elements was performed in four steps of ion chromatographic separation, which is summarised in Table 2.1. The digested sample fraction dissolved in 10 ml of 0.5 mol l<sup>-1</sup> HCl was loaded onto 20 ml of cation exchange resin (Bio-Rad AG50W-X12, 200-400 mesh). The HSE-rich solution eluted with 0.5 mol l<sup>-1</sup> HCl was evaporated to near dryness and again dissolved in 0.5 mol l<sup>-1</sup> HCl before being loaded onto an Eichrom-Ln resin (100-150µm) to separate Y, Zr and Hf. The HSE-rich fraction was eluted with 0.5 mol l<sup>-1</sup> HCl and evaporated to near dryness, then dissolved in 0.5 mol l<sup>-1</sup> HNO<sub>3</sub>. The HNO<sub>3</sub> solution was subsequently loaded onto a Bio-Rad Chelex100 resin (200-400 mesh) to separate the remaining Zr and Cd ions from Pd. Using the Chelex100 resin, Ru-Re-Ir-Pt-rich and Pd-rich fractions were eluted with 0.5 mol l<sup>-1</sup> HNO<sub>3</sub> and 8 mol l<sup>-1</sup> HCl, respectively. The Ru-Re-Ir-Pt-rich fraction was evaporated to near dryness at 100 °C and dissolved in 0.5 mol l<sup>-1</sup> HNO<sub>3</sub>, which was further purified to remove Cr, using a cation exchange resin (Bio-Rad AG50W-X8, 200-400 mesh).

#### **2.2.5. Recovery yield experiment of HSEs**

The recovery yields of HSEs and interfering elements after each purification step were examined using the matrix-containing synthetic samples. The matrix powder, ultramafic-mafic in composition (SiO<sub>2</sub> = 46.3, TiO<sub>2</sub> = 1.2, Al<sub>2</sub>O<sub>3</sub> = 7.1, Fe<sub>2</sub>O<sub>3</sub> = 11.5, MgO = 25.3, CaO = 5.1, Na<sub>2</sub>O = 1.1, and K<sub>2</sub>O = 0.4 g 100g<sup>-1</sup>) was prepared using chemical reagents (amorphous SiO<sub>2</sub>, Ti solution in 5% HNO<sub>3</sub>, Al solution in 5% HCl, Fe<sub>2</sub>O<sub>3</sub>, MgO, CaCO<sub>3</sub>, NaCl, and KNO<sub>3</sub>). For the recovery experiments concerning HSEs and interfering elements, a mixture of ~100 ng of HSEs dissolved in HCl and a mixture of ~2500 µg

of Cr, ~ 50 µg of Y, ~200 µg of Zr, ~500 ng of Cd and ~ 5µg of Hf dissolved in HCl were mixed with ~1 g of matrix powder, respectively. Recovery experiments were performed for both non-desilicification and desilicification procedures using these two sets (i.e., HSEs and interfering elements) of starting materials. After decomposing the starting materials by inverse aqua regia, 5 ml of 20 mol l<sup>-1</sup> HF was added for each set of samples and heated. Then, the decomposed sample was treated using the same procedure as for the natural samples. Finally, each sample solution was eluted following the procedure shown in Table 2.1. The recovery yield of HSEs and interfering elements after each ion chromatography step was determined by isotope dilution and calibration curve methods, respectively.

### 2.3. Mass spectrometric measurement

#### 2.3.1. Ru, Pd, Re, Ir and Pt mass fractions by ICP-MS

Ruthenium, Pd, Re, Ir and Pt intensities were measured using ICP-MS (ThermoScientific Element XR), and Os isotope ratios were measured as OsO<sub>3</sub><sup>-</sup> by TIMS (ThermoFinnigan TRITON). The ICP-MS measurements were performed using three analytical protocols: Ru-Ir-Pt, Re, and Pd analyses. Among these protocols, Ru-Ir-Pt and Pd fractions were measured with dry plasma using a desolvating nebulizer system (Cetac Aridus II) (Figure 2.4). For the Re measurements, a wet plasma was used because it is more effective in eliminating the memory effect as described by Fischer-Gödde et al. (2011). The desolvating nebulizer system effectively increases the intensities of target elements with decreasing interference oxide intensities for: <sup>53</sup>Cr<sup>16</sup>O<sub>3</sub><sup>+</sup> on <sup>101</sup>Ru<sup>+</sup>, <sup>89</sup>Y<sup>16</sup>O<sup>+</sup> on <sup>105</sup>Pd<sup>+</sup>, <sup>90</sup>Zr<sup>16</sup>O<sup>+</sup> on <sup>106</sup>Pd<sup>+</sup>, <sup>177</sup>Hf<sup>16</sup>O<sup>+</sup> on <sup>193</sup>Ir<sup>+</sup>, <sup>178</sup>Hf<sup>16</sup>O<sup>+</sup> on <sup>194</sup>Pt<sup>+</sup>, and <sup>179</sup>Hf<sup>16</sup>O<sup>+</sup> on <sup>195</sup>Pt<sup>+</sup>. The monitored mass to charge ratio (m/z) of the analytes and interferences for the Ru-Ir-Pt and Re fractions are m/z 53 (Cr), 99 (Ru), 101 (Ru), , 178 (Hf), , 185 (Re), 187 (Re), 188 (Os)191 (Ir), 193 (Ir), 194 (Pt), 195 (Pt), and for the Pd fraction are m/z 89 (Y), 90 (Zr), 105 (Pd), 106 (Pd), 112 (Cd) (Table 2.3). The ratios of CrO<sub>3</sub><sup>+</sup>/Cr<sup>+</sup>,

$YO^+/Y^+$ ,  $ZrO^+/Zr^+$  and  $HfO^+/Hf^+$  were monitored using 200 ng g<sup>-1</sup> of Cr solution, 1 ng g<sup>-1</sup> of Y solution, and 20 ng g<sup>-1</sup> of a Zr and Hf mixed solution dissolved in 0.5 mol l<sup>-1</sup> HNO<sub>3</sub>, which was prepared from commercially-available 100-1000 µg g<sup>-1</sup> standard solutions. The operating conditions of the ICP-MS are summarised in Table 2.2. All measurements were performed in the pulse-counting mode and low resolution mode with intensities < ~5-6 × 10<sup>6</sup> cps.

### 2.3.2. Os mass fractions and isotope ratios by TIMS

For Os isotopic composition measurements, purified Os was loaded on Pt filaments (0.5 mm × 0.025 mm; purity 99.999% m/m; H.Cross Company, Moonachie, USA) which were previously washed with 16 mol l<sup>-1</sup> HNO<sub>3</sub> and baked in air at 3 A for 2 minutes. Os dissolved in 8.8 mol l<sup>-1</sup> HBr was loaded slowly onto the filament and covered with 0.5 µl of a Ba(OH)<sub>2</sub>-NaOH activator (Creaser et al. 1991, Völkening et al. 1991), which was then heated in air under a heat lamp.

A gain calibration of the amplifiers was performed at the beginning of every daily analytical session. Oxygen gas was bled into the ion source, maintained at ~3 × 10<sup>-5</sup> Pa during the analyses. Employing a static multi-ion-collection mode using Faraday cups, <sup>184</sup>Os<sup>16</sup>O<sub>3</sub><sup>-</sup>, <sup>186</sup>Os<sup>16</sup>O<sub>3</sub><sup>-</sup>, <sup>188</sup>Os<sup>16</sup>O<sub>3</sub><sup>-</sup>, <sup>189</sup>Os<sup>16</sup>O<sub>3</sub><sup>-</sup>, <sup>190</sup>Os<sup>16</sup>O<sub>3</sub><sup>-</sup> and <sup>192</sup>Os<sup>16</sup>O<sub>3</sub><sup>-</sup> were simultaneously measured (Table 2.4). These signals were collected over 10 blocks of 10 cycles with an 8 s integration time and a 3 s idle time. When analysing low quantities of Os (<1 ng), a secondary electron multiplier (SEM) in peak-jumping mode was applied. The measurement in peak-jumping mode consisted of 5 blocks with 10 cycles per block, each cycle containing six masses including <sup>192</sup>Os<sup>16</sup>O<sub>3</sub><sup>-</sup>, <sup>190</sup>Os<sup>16</sup>O<sub>3</sub><sup>-</sup>, <sup>189</sup>Os<sup>16</sup>O<sub>3</sub><sup>-</sup>, <sup>188</sup>Os<sup>16</sup>O<sub>3</sub><sup>-</sup>, <sup>187</sup>Os<sup>16</sup>O<sub>3</sub><sup>-</sup> and <sup>186</sup>Os<sup>16</sup>O<sub>3</sub><sup>-</sup>, with integration times of 2, 1, 2, 4, 8, and 2 s, respectively (Table 2.4). The idle time was 3 s for mass 240 and 0.5 s for all other masses. Interfering ions (<sup>196</sup>Pt<sup>16</sup>O<sub>2</sub><sup>-</sup>, <sup>198</sup>Pt<sup>16</sup>O<sub>2</sub><sup>-</sup>, <sup>183</sup>W<sup>16</sup>O<sub>3</sub><sup>-</sup>, <sup>185</sup>Re<sup>16</sup>O<sub>3</sub><sup>-</sup>, <sup>194</sup>Pt<sup>16</sup>O<sub>3</sub><sup>-</sup>) were measured in the peak-jumping mode using a 4 s integration time for 1

block of 10 cycles, before and after the Os analysis, and the time-drifted interference intensity was used for Os data reduction.

Data reduction was performed in the following order on the raw data: correction for interferences, oxygen correction using the  $^{17}\text{O}/^{16}\text{O}$  and  $^{18}\text{O}/^{16}\text{O}$  ratios measured during each analytical session (Table 2.5 and 2.6), spike reduction, and instrumental mass fractionation correction using  $^{192}\text{Os}/^{188}\text{Os} = 3.083$  (Nier 1937) via the exponential law. The  $^{186}\text{Os}/^{188}\text{Os}$ ,  $^{187}\text{Os}/^{188}\text{Os}$  and  $^{190}\text{Os}/^{188}\text{Os}$  for DROsS (Durham Romil Osmium Standard supplied by IAGeo Limited) yielded  $0.11994 \pm 0.00006$ ,  $0.16092 \pm 0.00005$  and  $1.98381 \pm 0.00010$ , respectively, using 50 ng of Os measured in static mode (2SD,  $n=20$ );  $0.11993 \pm 0.00018$ ,  $0.16091 \pm 0.00012$  and  $1.98385 \pm 0.00020$ , respectively, using 1 ng of Os by static mode (2SD,  $n=21$ ); and  $0.11983 \pm 0.00097$ ,  $0.16079 \pm 0.00029$  and  $1.98451 \pm 0.00377$ , respectively, using 0.1 ng of Os by a peak-jumping mode (2SD,  $n=12$ ). These results agreed well with previously published data for the same material (Luguet et al. 2008, Wittig et al. 2010, Liu and Pearson 2014, Chatterjee and Lassiter 2015, Chu et al. 2015b) (Figure 2.5).

### **3. Results and discussion**

#### **3.1. Chemical separation of HSEs**

##### **3.1.1. Removing cationic matrix elements using cation exchange resin AG50W-X12**

Most studies that separate matrix elements by the cation-exchange method used AG50W-X8 resin for HSE separation (e.g., Meisel et al. 2003a, Shinotsuka and Suzuki 2007, Fischer-Gödde et al. 2011, Li et al. 2014). In this study, we selected an AG50W-X12 resin because it has a greater cation capacity than AG50W-X8. Comparison of elution curves for HSEs using 3 ml of AG50W-X8 and -X12 showed the superiority of X12 to reduce the tailing of Ru and more effectively separate the interfering elements Zr, Hf and Cd (Figure 2.7). Theoretically, >11 ml (calculation based on ion exchange capacity) of

AG50W-X12 resin is necessary to retain all cations in an appropriate bearing solution for ~1 g of natural silicate rocks ranging from rhyolitic to peridotitic in composition. In this study, we used 20 ml of resin to avoid the breakthrough of cations (Table 2.1 and Figure 2.6). The recovery of HSEs with and without matrix elements after the first column did not change significantly, resulting in > ~92% (Figure 2.7) and > ~95% yields (Figure 2.6), respectively while the major cations were reduced to almost negligible amounts. Figure 2.8 shows that there were no significant differences with regard to the recovery of interfering elements in the HSE cut between non-desilicified and desilicified samples: ~6% for Cr, < ~0.2% for Y, ~5-8% for Zr, ~21-23% for Cd, and ~1-6% for Hf. The cation exchange resin retains Cr<sup>3+</sup>, mainly forming Cr(H<sub>2</sub>O)<sub>6</sub><sup>3+</sup>, but it cannot adsorb the Cr<sup>6+</sup> mostly present in anion complexes such as Cr<sub>2</sub>O<sub>7</sub><sup>2-</sup> or CrO<sub>4</sub><sup>2-</sup> (Korkish 1989). Therefore, it is important to suppress the formation of Cr<sup>6+</sup> in the sample solution to retain Cr in the cation exchange resin. Cr concentration in the HSE-rich fraction significantly increased when the sample solution dissolved in HCl was evaporated at >110 °C. Thus, the evaporation temperature before sample loading was set at 100 °C. Following this procedure, the majority of Cr was separated from the HSE-rich fraction, and further separation of Cr was achieved at the final purification step, as we will discuss in a later section.

### **3.1.2. Secondary purification of Pd-Ir-Pt from Zr and Hf by Ln resin**

Molecular interferences of ZrO<sup>+</sup> and HfO<sup>+</sup> are significant for Pd and Ir-Pt, respectively, because of the elevated Zr/Pd, Hf/Ir and Hf/Pt ratios in terrestrial rock samples. To separate Zr and Hf from HSEs, Ln resin was used because it can selectively retain Zr and Hf chloro-complexes (Münker et al. 2001). Calculation of the distribution coefficient ( $K_d$ ) for the distribution of HSEs, Zr, and Hf between Ln resin and 0.5 mol l<sup>-1</sup> HCl using the batch method (Table 2.7) yielded extremely high  $K_d$  values for Zr and Hf (>10<sup>6</sup>) and low values for HSEs (< 2 for Ru, Pd, Ir and Pt and 11 for Re). This suggests that a low molarity of HCl effectively separates Zr, Hf and Y ( $K_d$  = ~500) from HSEs. Using a matrix-free

synthetic HSE solution, ~100% of Ru, Pd, Re, Pt and ~90% of Ir were recovered in the HSE cut. The recoveries of HSEs with matrix elements after the second column were ~83-96% and ~90-100% from the starting materials with and without desilicification, respectively. Interfering elements Zr and Hf were completely removed by Ln resin for the non-desilicified sample. However, ~6% of Zr and ~3% of Hf remained in HSE cut for the desilicified sample (Figure 2.8). This reveals that fluoro-complexes of Zr and Hf, which are more stable than chloro-complexes of these elements (Makishima et al. 2009), remained in the solution even after repeated addition of HCl. Because the  $K_d$  values of Zr, Hf and HSEs are nearly identical between the Ln resin and 0.5 mol l<sup>-1</sup> HF, it is difficult to separate these elements by the second column (Table 2.7). However, the first and second columns effectively separated Y from the HSE cut for the desilicified sample (~0.2% and < ~0.01% after first and second columns, respectively), because of the higher  $K_d$  for Y between the Ln resin and 0.5 mol l<sup>-1</sup> HF than for the HSEs (Table 2.7). Nearly all Cr and Cd were eluted in the HSE cut both for non-desilicified and desilicified samples during the second column (Figure 2.8).

### **3.1.3. Separation of Ru-Re-Ir-Pt fraction and Pd fraction during Chelex 100 resin**

Chelex 100 resin is an organic ion exchanger containing weakly acidic iminodiacetic functional groups with strong chelating properties, and forming chelate complexes with numerous metal cations. The actual form of the functional group when acting as a cation exchanger or anion exchanger depends on the pH of the medium. In this study, Chelex 100 was conditioned in an acidic medium. The  $K_d$  values of the target elements with various reagents are shown in Table 2.7. The elution profile of Chelex 100 resin using ~1g of desilicified TDB-1 is shown in Figure 2.9. The elution profiles of Hf and Y are not shown in Figure 2.9, because the quantities of Hf and Y in the loading solution were reduced to almost negligible levels (< ~100 pg) in the HSE cut after the second column. However, we observed that the behaviour of Hf and Y is similar to that of Zr using both matrix-free and matrix-containing synthetic

solutions, which is consistent with the  $K_d$  values of these elements between Chelex 100 and  $0.5 \text{ mol l}^{-1} \text{ HNO}_3$  and HF (Table 2.7). Figure 2.9 shows that Zr and Cd were eluted with the Ru-Re-Ir-Pt fraction by  $0.5 \text{ mol l}^{-1} \text{ HNO}_3$ , whereas Pd was retained in Chelex 100, which was collected by  $8 \text{ mol l}^{-1} \text{ HCl}$ . Thus, the third column could effectively remove the Zr fluoro-complex and Cd from Pd. Figure 2.8 indicates that nearly 100% of Ru, Re, Ir and Pt were eluted for non-desilicified sample through the third column. However, recoveries of Ru, Re, Ir and Pt for the desilicified sample were ~63-80%. This might be attributed to the presence of fluoro-complexes of HSEs in the loading solution because  $K_d$  values of HSEs between Chelex 100 and  $0.5 \text{ mol l}^{-1} \text{ HF}$  are higher than those between  $0.5 \text{ mol l}^{-1} \text{ HNO}_3$  (Table 2.7). The recovery of Pd for both non-silicified and silicified samples reveals that ~20 % of the loaded Pd was retained in the third column, which could occur due to a strong affinity of Pd in anionic form to Chelex 100.

Our results indicate that it is better to minimise the formation of fluoro-complexes prior to the use of the second and third columns, in order to enhance recoveries of HSEs and remove Hf. Figure 2.8 shows that recovery of Hf in the Ru-Re-Ir-Pt cut after the third column for the desilicified sample was ~3% while that of the natural samples was almost negligible. This difference between matrix-contained recovery experiments and natural samples could be caused by the HF dissolution procedure. For the natural samples, HF dissolution was performed only for residues after the inverse aqua regia decomposition, whilst it was performed for all solutions during the matrix-contained recovery experiments. We also found that the recovery of Hf in the Ru-Re-Ir-Pt cut increased when HF-desilicification was performed for both the supernatant solution and residues, following inverse aqua regia decomposition. In this study, therefore, desilicification was only performed for the residues.

#### **3.1.4. Final purification of Ru from Cr during cation exchange resin AG50W-X8**

It was found that ~6% of Cr still remained in both desilicified and non-desilicified synthetic solutions after the third column (Figure 2.9). Ru concentrations in terrestrial rock samples are much lower than Cr concentrations (typically Cr/Ru > ~400,000 for basalt and peridotite) and Cr/Ru might possibly increase during the desilicification process as Cr is hosted in silicates or oxide minerals in rocks. Therefore, it would be advisable to further reduce the Cr concentration, because Cr multi-oxide probably interferes with Ru in natural samples, when no further purification is conducted. In this study, ~60-85% of Ru, Re, Ir and Pt were collected, and > ~99% of Cr was removed after the final ion chromatography step using the AG50W-X8 resin, which was modified using the method in Yamakawa et al. (2009).

### **3.2. Recovery yield of HSEs, interfering elements, and blank**

#### **3.2.1. Recovery yield of HSEs in natural samples**

The recovery yields of HSEs from natural sample (UB-N) determined by calibration curve method calibrated by HSE standard solution, both with and without desilicification, were ~60-80% for Ru, Re, Ir and Pt and ~80-90% for Pd, which is almost consistent with the results determined by matrix-contained synthetic solutions (Figure 2.8). Several studies previously reported the recovery of HSEs from natural samples. Using an anion exchange resin, variable yields (~30-90%) of HSEs from ultramafic and mafic samples were reported by Pearson and Woodland (2000) and Chu et al. (2015a). Using a cation exchange resin, Shinotsuka and Suzuki (2007) showed ~70-90% of HSEs for TDB-1 and JP-1. Therefore, the recovery yields achieved in this study were comparable with or better than those reported in the previous studies.

#### **3.2.2. Elimination of interfering elements**

Table 2.8 shows the ratios of interferences intensities relative to the measured intensities of HSE

isotope masses during ICP-MS measurement for reference materials. The ratios were negligible, as follows: <1 parts per million (ppm) for  $^{53}\text{Cr}^{16}\text{O}_3^+$  on m/z 101 (Ru) and for  $^{89}\text{Y}^{16}\text{O}^+$  on m/z 105 (Pd), <2 ppm for  $^{178}\text{Hf}^{16}\text{O}^+$  on m/z 194 and for  $^{179}\text{Hf}^{16}\text{O}^+$  on m/z 195 (Pt), and  $<26\pm 20$  ppm for  $^{177}\text{Hf}^{16}\text{O}^+$  on m/z 193 (Ir). The sum of  $^{106}\text{Cd}^+$  and  $^{90}\text{Zr}^{16}\text{O}^+$  exceeded 100 ppm (23-249 ppm) for m/z 106 (Pd), which however, did not affect the result, despite not performing an interference correction. It is therefore concluded that no interference correction is necessary for Ru, Pd, Re, Ir and Pt measurements in our analytical method. Because this method can effectively purify Pd with high recovery (~80-90%), it has great potential for application to precise Pd isotope analysis.

### **3.2.3. Total procedural blanks**

Total procedural blanks of HSEs from this study were 0.9-2.5 pg for Ru, 8.8-25 pg for Pd, 0.01-0.5 pg for Re, 0.05-0.4 pg for Ir, 1.2-18 pg for Pt and 0.9-3.9 pg for Os. Figure 2.10 shows the comparison of the total procedural blanks in this study with those previously published. The mean values of the Re, Ir and Pt blanks tended to be somewhat lower than those obtained by both CT and HPA methods. The main source of Pd in the blank from this study could have come from the Chelex 100 resin. This is similar behaviour to that reported in the studies which used anion exchange resin such as AG1X-8, which contains considerable amounts of Pd. Therefore, minimising the contamination of resin blanks using sufficient cleaning procedures is important to keep consistent blank levels (e.g., Becker et al. 2006, Ishikawa et al. 2014). In this study, the proportion of HSEs in blanks was 0.8-3.5 % for Os and < 1% for other HSEs for TDB-1; 0.8-2% for Pd, 0.02-1% for Re and < 1% for other HSEs for JP-1; and <1% for all HSEs for UB-N, MUH-1 and OKUM. Although the proportions of blanks were low, all concentrations and isotopic compositions were blank-corrected based on the measurement of blanks that were undertaken along with the measurement of the samples.

### 3.3. HSE mass fractions and Os isotope ratios of reference materials

The HSE mass fractions and Os isotope ratios of reference materials UB-N, JP-1, MUH-1, OKUM and TDB-1 were determined by our analytical method (Table 2.9 and 2.10). The primitive upper mantle (PUM)-normalised HSE patterns for these reference materials are shown in Figure 2.12.

#### 3.3.1. UB-N

UB-N, a serpentinised fertile Iherzolite, is recognized as a relatively homogeneous ultramafic reference material for HSE analysis (Meisel and Moser 2004b), and has been determined by many laboratories. All HSE data determined in desilicified and non-desilicified analyses showed no considerable differences in our study. The mass fractions of HSEs as well as  $^{187}\text{Os}/^{188}\text{Os}$  ratios (care should be taken that all Os mass fractions and isotopic compositions of both our data and referred published data were compiled in CT in Figure 2.11a-c, as Os was extracted and analysed before desilicification) were in good agreement with the range of the published data (Figure 2.11a and 12). Among all HSEs, in particular, the Re and Pt showed relatively more variable mean mass fractions between laboratories, especially for those more than one time higher intermediate precision values than those in our study, such as Re ( $0.210 \pm 0.018 \text{ ng g}^{-1}$ , 1SD and  $n = 9$ ) in CT data (Ishikawa et al. 2014) and ( $0.201 \pm 0.012 \text{ ng g}^{-1}$ , 1SD and  $n = 8$ ) in HPA data (Fischer-Gödde et al. 2011), and Pt ( $8.07 \pm 1.17 \text{ ng g}^{-1}$ , 1SD and  $n = 6$ ) in CT data (Luguet et al. 2007). As the majority of HSE contents in UB-N are typically hosted in base metal sulfides, which are easily decomposed during acid digestion, thus, the higher variance of Re and Pt in UB-N might be dominated by other artificial effects other than lab bias. It should be noted that UB-N is distributed only in coarse grained batches, and powders are presumably further pulverised among independent laboratories. It was observed that Cr concentrations vary systematically from batch to batch, possibly causing the differences in HSE concentrations (Meisel and Horan, 2016).

Generally, the HSEs in UB-N seem to be relatively homogeneous compared to the ultramafic reference materials JP-1 and MUH-1 from our study (Figure 2.7). However, the reproducibility (RSD: relative standard deviation) of Pt, Pd and Re (1.8-2.5% RSD for desilicified samples, and 2.6-5.2% RSD for non-desilicified samples) in UB-N were more favorable than those of Ru, Ir and Os (6.8-13.6% RSD for desilicified samples, and 5.0-10.3% RSD for non-desilicified samples) (Table 2.9), which indicates that Ru, Ir and Os might also reside in alloys or difficult to digest platinum-group minerals such as laurite (Ru, Os, Ir)<sub>2</sub>S<sub>2</sub> in UB-N (even HF treatment did not seem to favor their digestion), by contrast, the Pt, Pd and Re are almost entirely hosted in base metal sulfides of the sample matrix (Meisel et al. 2003a, b).

### 3.3.2. JP-1

JP-1 is a highly depleted harzburgite as ultramafic reference material for HSE analysis barely reported in a few literatures. Our results did not display systematic differences between the data for the desilicified and non-desilicified methods (Figure 2.11b and 2.12). The mass fractions of Pd, Pt and Os were in good agreement with the range of the reported data both with and without desilicification. Moreover, the desilicified data of Ru and Ir also agreed well with both the desilicified and non-desilicified data in the literatures, whereas the non-desilicified data of them had slightly lower mean mass fractions, but consistent with the desilicified data from this study (within 1 SD intermediate precision). Because their intermediate precisions for both desilicified and non-desilicified analyses were relatively large, perhaps it resulted from the effect of sample heterogeneity rather than desilicification. Although there was no difference for Re in this study among the desilicified and non-desilicified analyses, our values were ~20% higher than the values in the literatures, except for those reported by Meisel and Moser (2004b), which were one order of magnitude higher and with a large intermediate precision ( $0.29 \pm 0.36 \text{ ng g}^{-1}$ , 1SD and n=9). The reason for the significant difference in

Re is uncertain, but it could reflect the nugget effect. In this study, every HSE of JP-1 was poorly reproducible compared to those of UB-N (Table 2.9), which demonstrates that the host minerals of HSEs in JP-1 are more inhomogeneously distributed through the sample powder. Moreover, the Pd and Re (6.8-12% RSD) were relatively more reproducible than Ru, Ir, Os and Pt (15-27% RSD). Hence, the variance of HSEs in JP-1 may be strongly influenced by host minerals such as laurite, and Pt-rich nugget. The  $^{187}\text{Os}/^{188}\text{Os}$  ratios agreed well with those provided by Ishikawa et al. (2014), however, the published data of them are quite limited in number for further discussion. The results of UB-N and JP-1 indicate that in their analyses HF treatment was unnecessary, as suggested in Meisel et al. (2003b) and Ishikawa et al. (2014).

### **3.3.3. MUH-1**

In this study, the HSEs of MUH-1, a depleted harzburgite, displayed no systematic variations between the desilicified and non-desilicified methods (Figure 2.12). Although the mean mass fraction of Re in desilicified samples was slightly higher than that in non-desilicified samples, the firm conclusion (i.e., the effectiveness of HF on Re extraction) cannot be drawn at present, as every single desilicified data was not systematically higher than non-desilicified data (Table 2.9). The slight variances in Re might in some way reflect the inhomogeneity of sample powder. The reason is uncertain, thus, it may require further scrutiny. All HSEs (except for Re and Ir) were less reproducible than UB-N (a fertile lherzolite), but were quite similar to JP-1 (a harzburgite).

### **3.3.4. OKUM**

The reference material OKUM (a komatiite) somehow displayed different characteristics of HSEs as ultramafic rock as observed in our study. Each desilicified-sample showed systematically higher mass fractions of Ru, Ir and Pt compared to non-desilicified samples (Table 2.10 and Figure 2.12). Moreover,

the desilicified mean mass fractions of Ru, Ir, and Pt were ~11%, ~24%, ~13%, respectively, higher than non-desilicified data. The mean mass fractions of both Pd and Re with and without desilicification, were in good agreement with the range of non-desilicified HPA data reported by Savard et al. (2010) (Pd=12.20±6% RSD; Re=0.566±6% RSD) and Wang and Becker (2014) (Pd=11.8±4% RSD; Re=0.4±21% RSD). However, the desilicified data of Ru (4.39±1.2% RSD), Ir (0.951±9.3% RSD) and Pt (11.5±1.7% RSD) from our study seemed more consistent with HPA data both from Savard et al. (2010) (Ru=4.15±2% RSD; Ir=0.943±4% RSD; Pt=11.44±2% RSD) and Wang and Becker (2014) (Ru=4.44±2% RSD; Ir=0.897±8% RSD). Hence, this could be explained by the incomplete digestion in OKUM by CT method used in this study (i.e., Ru, Ir and Pt may be released more completely from the whole rock powder at elevated temperatures with prolonged heating, even without HF treatment). The same problem occurred in Re from TDB-1 which was discussed in Ishikawa et al. (2014) and Meisel and Horan (2016) (see section on TDB-1 as below). It is also possible that CT method is less efficient in dissolving HSE-bearing phases than HPA method. For example, Meisel et al. (2003b, 2004a) examined and discussed about the efficiency of both CT and HPA methods on HSE extractions of UB-N. Nevertheless, the HF treatment is somewhat useful to liberate Ru, Ir and Pt from residues during CT decomposition from our study. Furthermore, it should be noted that Pt (46% RSD) and Os (97% RSD) in OKUM reported by Wang and Becker (2014) were particularly heterogeneous (at 0.5-1 g test portion size), which demonstrates that the Pt and Os concentrations may be influenced significantly by the nugget effect. The variance of Os also occurred in OKUM in our study, but they were more reproducible (15% RSD). In general, it is evident that the homogeneity of HSEs in harzburgites (JP-1 and MUH-1) are much worse than those in lherzolite (UB-N) and komatiite (OKUM). Most of HSEs in harzburgites are hosted in alloys and laurites, whereas the dominant HSE-bearing phases in lherzolites and komatiites are base metal sulfides, which are more easily digested in aqua regia (Meisel et al. 2013).

### 3.3.5. TDB-1

TDB-1 is a widely used mafic reference material for HSE analysis (e.g., Meisel and Moser 2004a, b, Ishikawa et al. 2014). The results demonstrate that the mass fractions of Ru and Re for desilicified analyses were higher than those for the non-desilicified analyses, while the mass fractions of Pd, Ir and Pt were identical by the two methods, within a 1SD intermediate precision (Figure 2.11c and 12). It is also observed that Ir (>15% RSD) seemed much more heterogeneous than other HSEs in TDB-1 from this study (Table 2.10). The problems of incomplete recovery of HSEs in TDB-1 during acid digestion have been pointed out elsewhere (e.g., Dale et al. 2009, Meisel et al. 2009). Dale et al. (2012b) also discovered that Ru and Re concentrations with desilicification in TDB-1 by HPA digestion were consistently ~40% and ~24%, respectively higher than those obtained without desilicification. Ishikawa et al. (2014) further examined the efficiency of both Ru and Re extractions using different digestion methods at various heating conditions, which suggested that either the CT or the HPA method, followed by the desilicification, was the most favorable protocol for their complete recoveries from TDB-1. Moreover, both Ishikawa et al. (2014) and Meisel and Horan (2016) pointed out that Re in TDB-1 was able to fully extracted from the sample matrix at elevated temperatures over longer durations in aqua regia, even without additional treatment by HF. By contrast, Ru was dependent on HF treatment for complete release from silicates minerals. As shown in figure 2.11c, it is also apparent that the higher variance of Re without desilicification in both CT and HPA digestions was the result of incomplete Re recoveries at different conditions between individual laboratories, whereas the nearly constant non-desilicified Ru concentrations among labs indicated the usefulness of HF treatment. Therefore, the result of systematic higher Ru and Re values for desilicified method, relative to non-desilicified method obtained under the equal heating conditions in this study, also supports the previous theory on the effectiveness of HF treatment on the enhancement of both Ru and Re extractions (e.g., Meisel et al. 2009, Dale et al. 2012b, Ishikawa et al. 2014). Instead, the identical Pd,

Ir and Pt mass fractions with and without desilicification imply that they were probably completely extracted from the whole rock powder by non-desilicified method. The mean mass fraction of Os was nearly consistent with the reported data of both CT and HPA methods, except for those of Ishikawa et al. (2014), Qi and Zhou (2008) and Savard et al. (2010). Among all HSEs, the high variance of Os between laboratories could be possibly affected by the nugget effect. Furthermore, the  $^{187}\text{Os}/^{188}\text{Os}$  ratios in our study agreed well with previously reported CT and HPA data, within a 1SD intermediate precision.

#### 4. Conclusions

An effective analytical method was developed for the determination of HSE and Os isotopic compositions from the same aliquot for natural samples by high-resolution ICP-MS and TIMS coupled with isotope dilution methods. This study presents two new methodologies for the purification of Ru, Pd, Re, Ir and Pt: (1) a 50W-X12 cation exchange resin can more effectively separate HSEs, in particular Ru, from matrix elements than the 50W-X8 resin generally used in previous studies, (2) When the HF-desilicification was performed during sample decomposition, trace amounts of Zr, forming stable fluoro-complex, cannot be removed by Ln resin. Chelex 100, however, can effectively separate Pd from the Zr fluoro-complex, because the  $K_d$  of Pd is ~1000-3000 times higher than that for Zr in both diluted HF and  $\text{HNO}_3$ . Furthermore, the Cr multi-oxide interference in Ru analysis, rarely discussed in previous literature, was critically evaluated. In this method, with careful purification and utilisation of the desolvating nebulizer system, the ratios of the interferences intensities relative to the measured intensities of HSE isotope masses:  $\text{CrO}_3^+/\text{Ru}^+$  (101),  $\text{YO}^+/\text{Pd}^+$  (105),  $\text{Cd}^+/\text{Pd}^+$ (106),  $\text{ZrO}^+/\text{Pd}^+$  (106),  $\text{HfO}^+/\text{Ir}^+$ (193) and  $\text{HfO}^+/\text{Pt}^+$  (194,195), were reduced by less than a few hundred parts per million. Thus, no interference correction is required for the measurement of Ru, Pd, Re, Ir and Pt for both desilicified and non-desilicified geological samples. The contributions of

procedural blank of HSEs in reference materials as ~ 1g of sample size were < ~1% and did not significantly affect the results.

The HSE and Os isotopic compositions of UB-N, JP-1 and TDB-1, which have already been commonly used as reference materials between laboratories, determined in this study were in good agreement with the range of the previously published data, which demonstrates the feasibility and validation of our analytical method for interlaboratory comparison. Furthermore, the effectiveness of HF-desilicification on the extraction of Ru, Pd, Re, Ir and Pt from whole rock sample was evaluated for UB-N (ultramafic rock), JP-1 (ultramafic rock), TDB-1 (mafic rock), and two new certified ultramafic reference materials MUH-1 and OKUM. Our results indicate that desilicification is required to enhance the recovery of both Ru (~30%) and Re (~10%) from TDB-1. However, unlike mafic rock, UB-N and JP-1 is independent of the use of HF or not. The results of UB-N, JP-1 and TDB-1 support the same conclusions which have already been pointed out elsewhere. Essentially, MUH-1, similar to UB-N and JP-1, is also unnecessary for the application of HF, as its HSE data in desilicified and non-desilicified samples displayed no significant differences. The variances of Re in MUH-1 may perhaps reflect the heterogeneity of sample powder, not the result of the HF treatment. The reference material OKUM somehow presented different characteristics of HSEs as ultramafic rock. In this study, the systematic higher desilicified data of Ru (~11%), Ir (~24%) and Pt (~13%) than non-desilicified data demonstrate that the HF-desilicification is effective to liberate Ru, Ir and Pt from the residues during CT digestion. Knowing that this study used ~1 g test portion size, among four ultramafic reference materials, the homogeneity of HSEs in harzburgites JP-1 and MUH-1 are generally worse than those in lherzolite UB-N and komatiite OKUM.

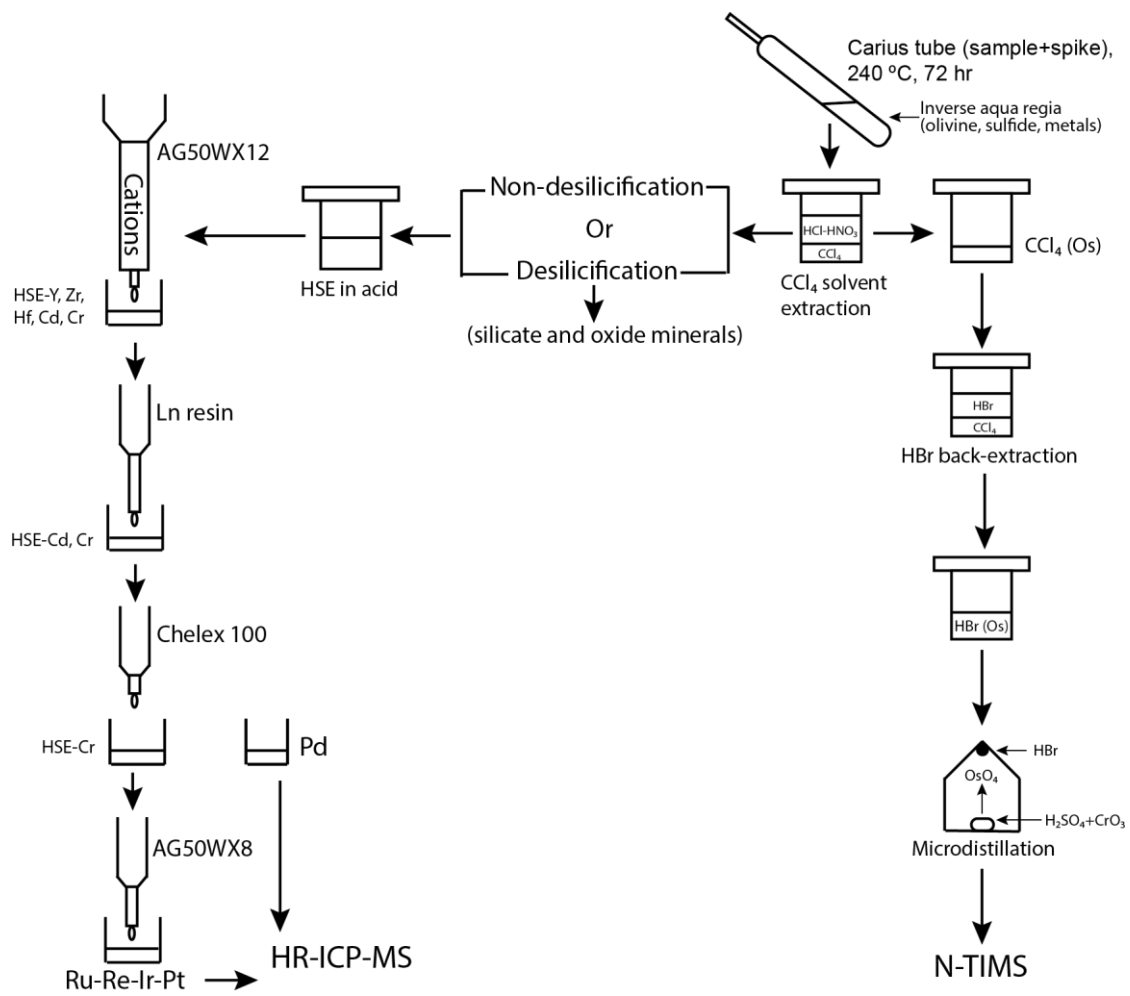


Figure 2.1. Workflow diagram for separations and determination of HSE mass fractions and Os isotope ratios developed in this study.



Figure 2.2. Photo of borosilicate Carius tube (2.5 mm thick and 200 mm long) (left) and stainless steel jacket with the tube (right) connected to the exhaust post of the laboratory.

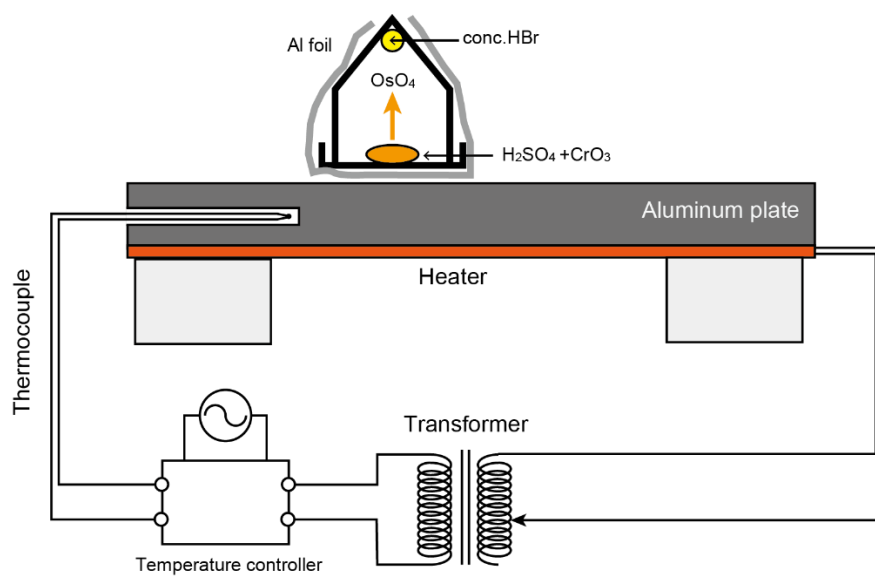


Figure 2.3. Os final purification by microdistillation.



Figure 2.4. Photo of CETAC Aridus II™ Desolvating Nebulizer system

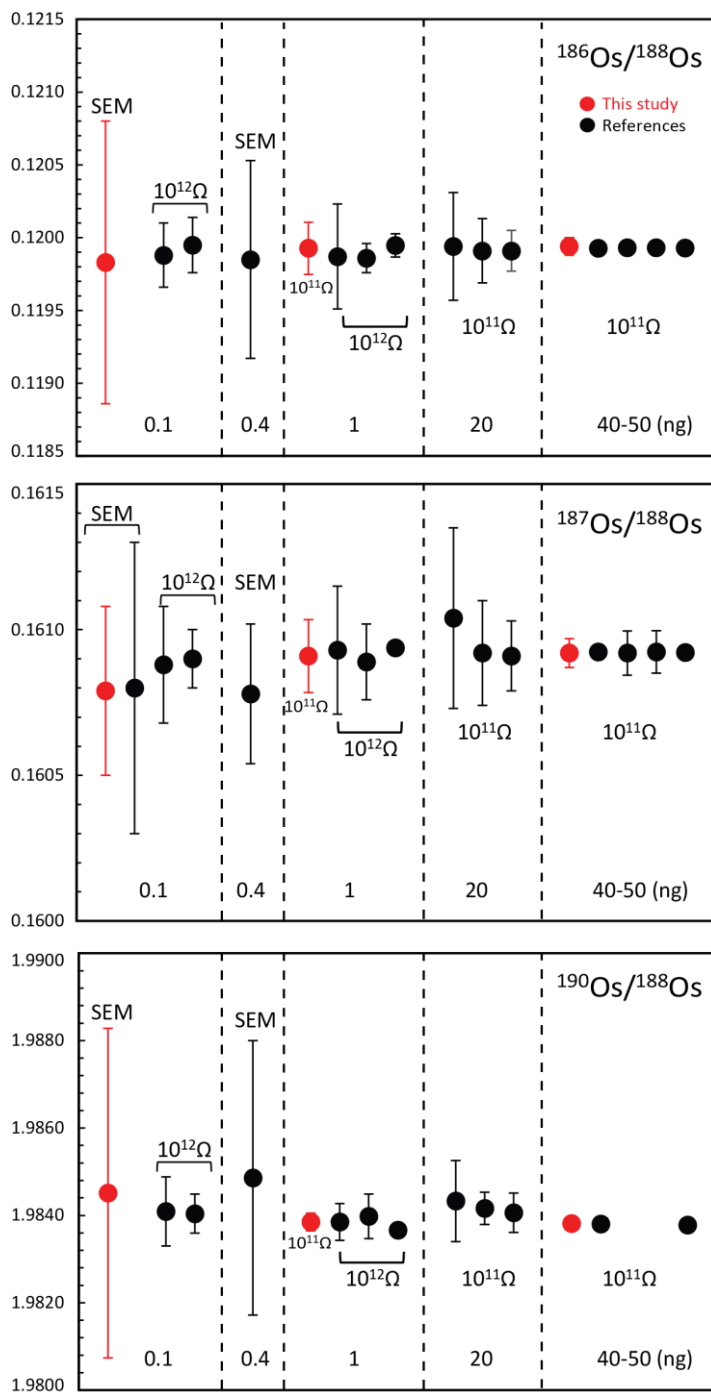


Figure 2.5.  $^{186}\text{Os}/^{188}\text{Os}$ ,  $^{187}\text{Os}/^{188}\text{Os}$  and  $^{190}\text{Os}/^{188}\text{Os}$  ratios with 2SD of 0.1-50 ng of DROsS using both static mode ( $10^{11}\Omega$  and  $10^{12}\Omega$  resistors) and peaking-jumping mode from this and previous studies.

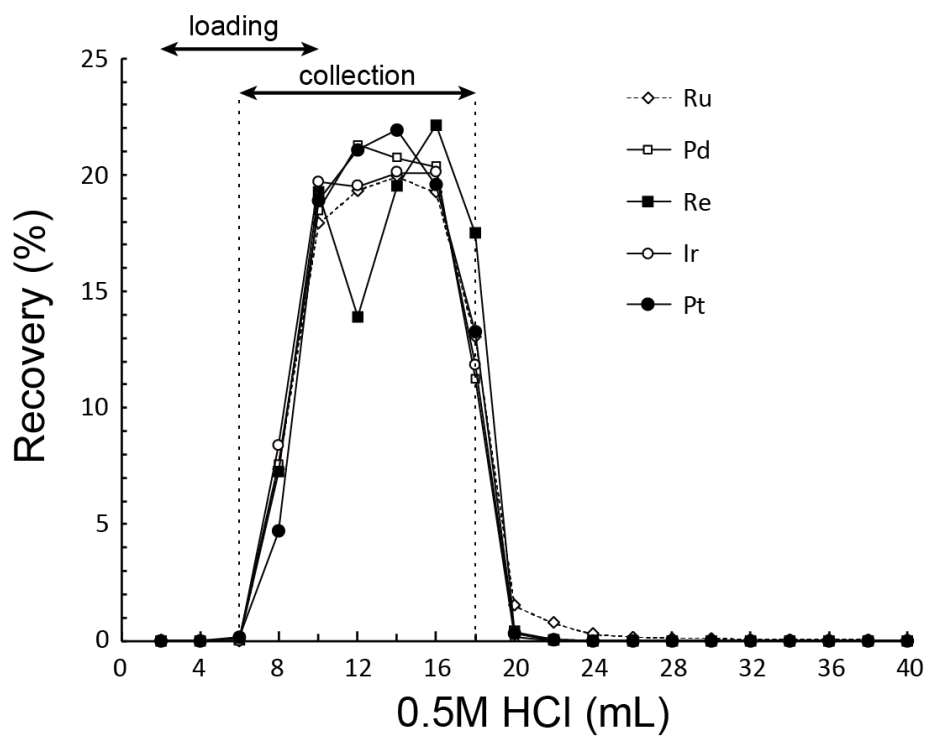


Figure 2.6. Elution profiles of HSEs (synthetic solution) during 1<sup>st</sup> column using 20 ml of cation exchange resin AG50W-X12.

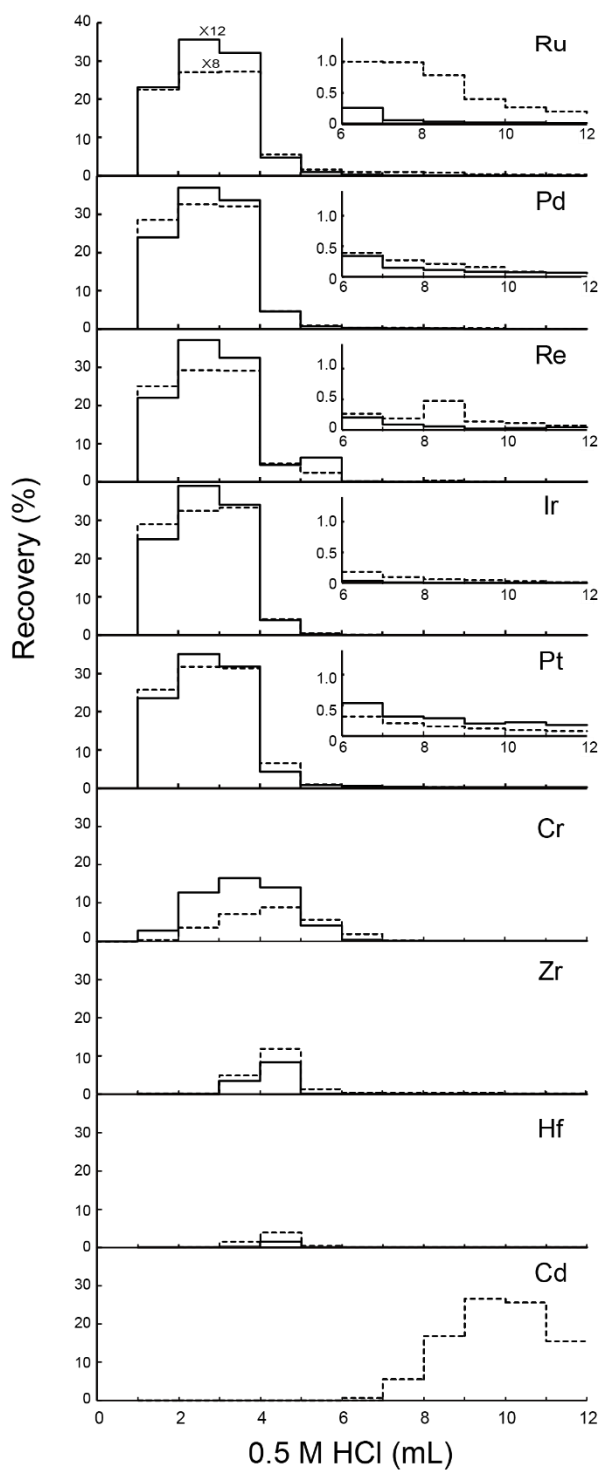


Figure 2.7. Elution profiles of HSEs and interfering elements (synthetic solution) in 3 ml of AG50W-X8 (broken line) and -X12 (solid line). The insert for HSE shows the tailing of Ru, Pd, Re, Ir and Pt eluting from 6 to 12 ml for both X8 and X12

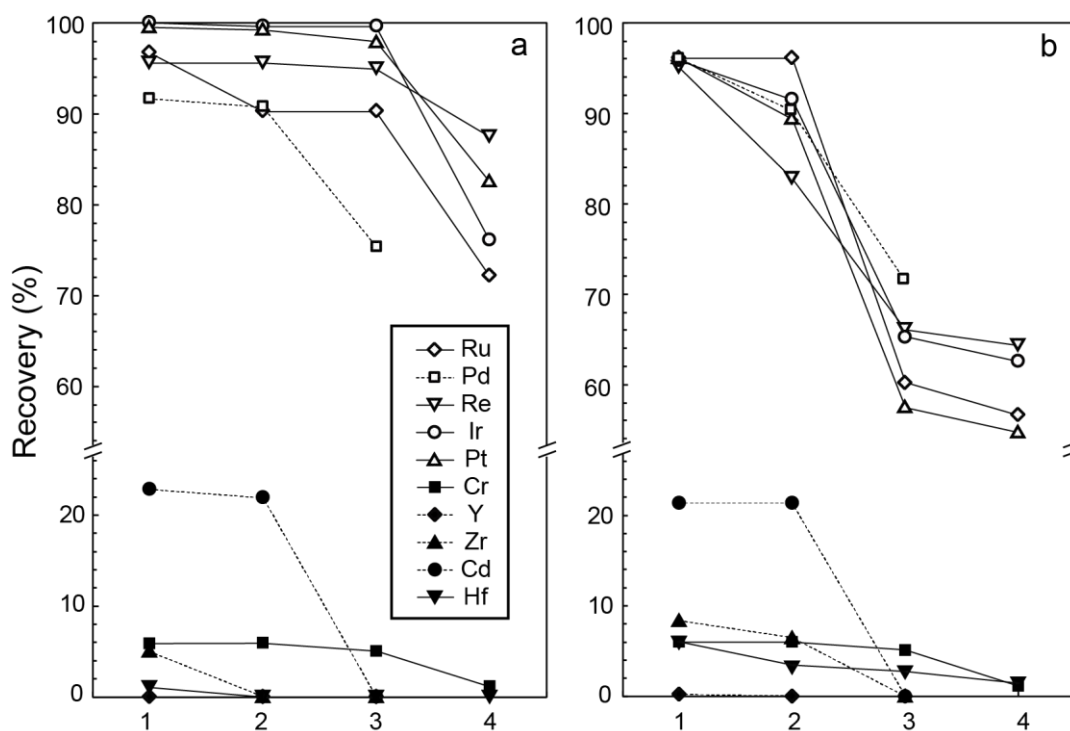


Figure 2.8. Recovery yields of HSEs and interfering elements (Cr, Y, Zr, Cd and Hf) for each column using matrix-containing synthetic solution without (a) and with (b) desilicification. 1: AG50W-X12, 2: Ln resin, 3: Chelex 100, 4: AG50W-X8. For the 3<sup>rd</sup> column, two fractions were collected, one is the Ru-Re-Ir-Pt cut, and the other is the Pd cut (Figure 1.9). The recoveries shown for 3<sup>rd</sup> column are: Ru, Re, Ir, Pt, Hf and Cr for the Ru-Re-Ir-Pt cut and Pd, Zr, Y and Cd for the Pd cut.

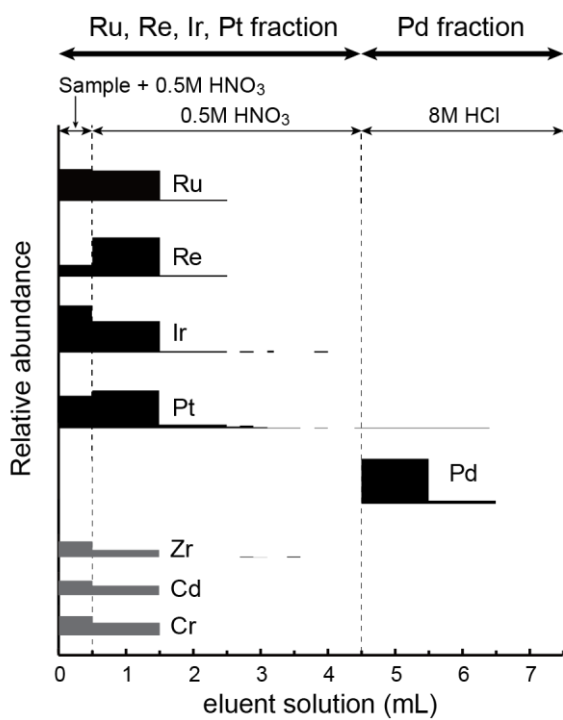


Figure 2.9. Elution profiles of HSEs (reference material TDB-1 with desilicification by HF) during 3<sup>rd</sup> column using Chelex100 resin: Pd was successfully separated from Zr and Cd.

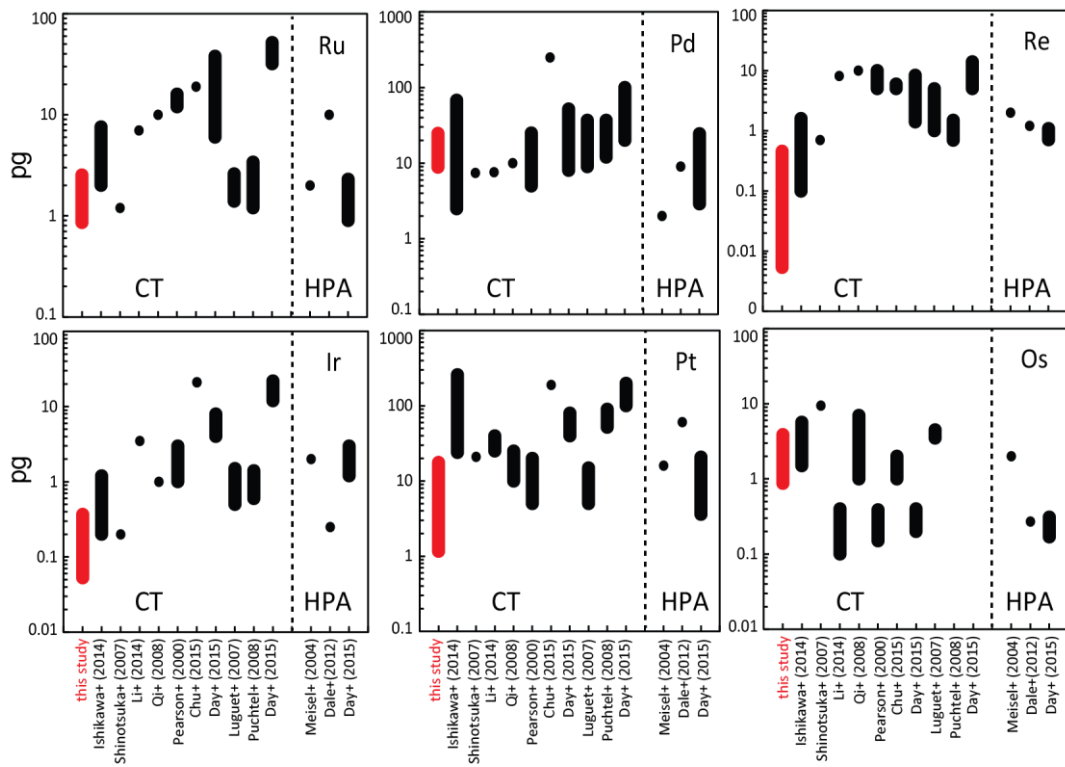


Figure 2.10. Range of total procedural blanks from this study and previous studies, CT: Carius tube, HPA: high pressure asher.

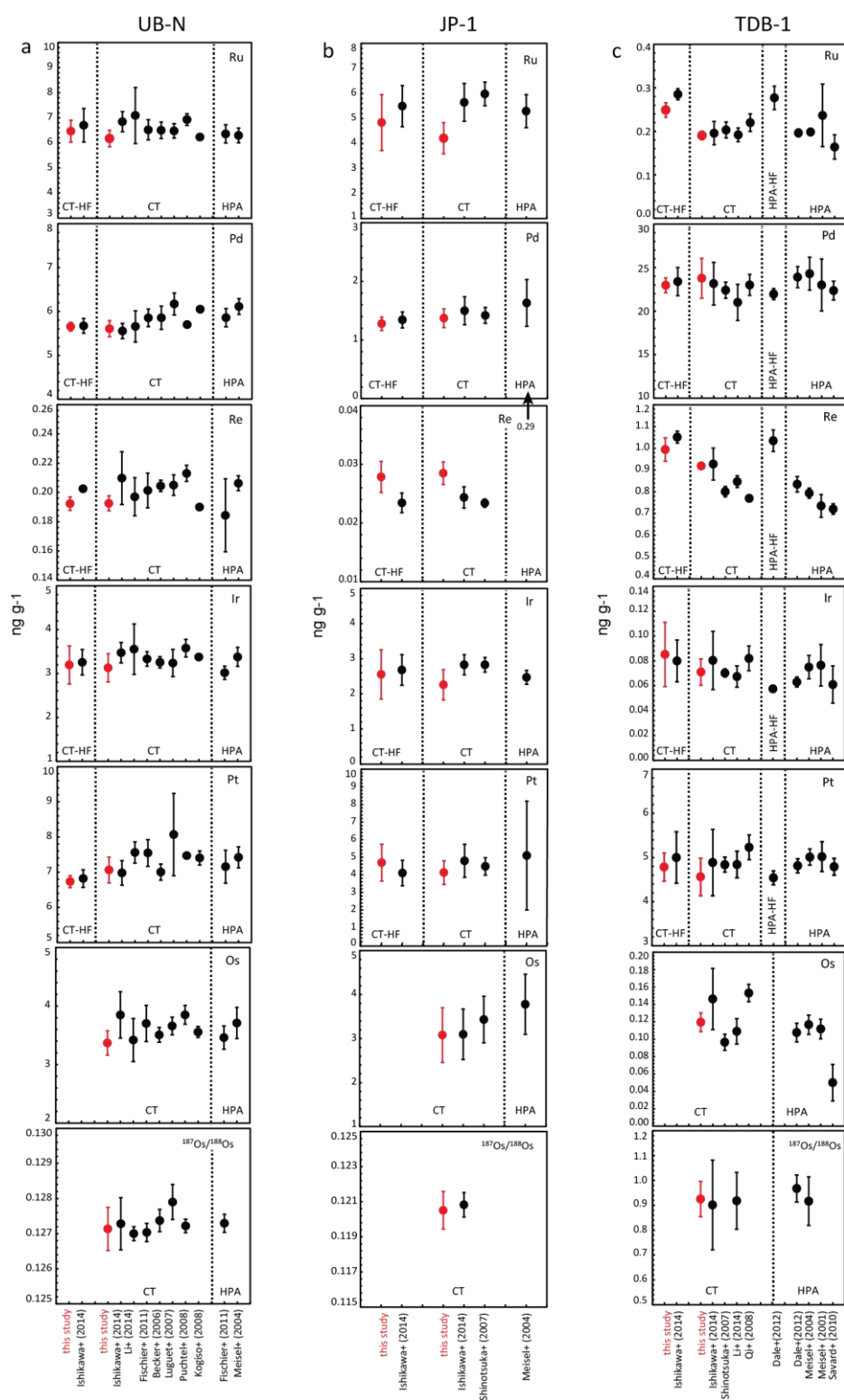


Figure 2.11a-c. HSE mass fractions for reference materials UB-N, JP-1 and TDB-1, respectively; comparison with previous studies (error bar: 1SD), CT: Carius tube, CT-HF: Carius tube with post-Os desilicification, HPA: high pressure ashers, HPA-HF: high pressure ashers with post-Os desilicification. Os data of CT-HF were compiled with Os data of CT in this and previous studies.

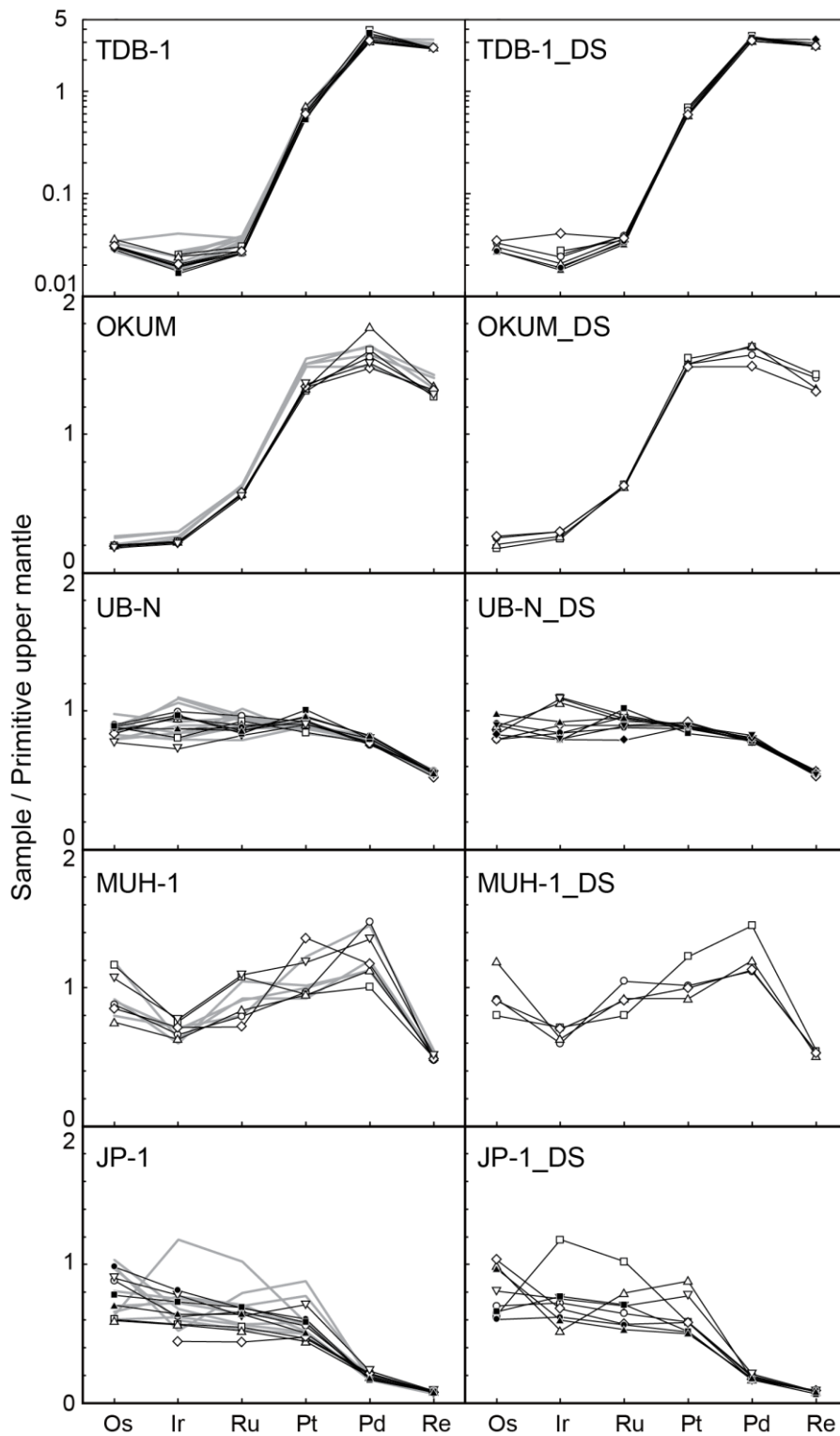


Figure 2.12. PUM-normalised HSE patterns for reference materials TDB-1, OKUM, UB-N, MUH-1 and JP-1, respectively with and without desilicification by HF from this study. The gray lines denote HSE patterns of DS. The PUM data are from Becker et al. (2006). DS: HF-desilicification

Table 2.1. Separation scheme for Ru-Pd-Ir-Re-Pt purification.

<b>(1) Separation of Ru-Pd-Ir-Re-Pt from matrix cations</b>	
AG50WX12 (200-400 mesh): 20 ml	
Column dimension: 15 mm wide × 120 mm long	
Resin cleaning	150 ml 6 mol l <sup>-1</sup> HCl
Conditon	100 ml 0.5 mol l <sup>-1</sup> HCl
Load sample	6 ml 0.5 mol l <sup>-1</sup> HCl
Load and collect sample	4 ml 0.5 mol l <sup>-1</sup> HCl
Collect sample	8 ml 0.5 mol l <sup>-1</sup> HCl
<b>(2) Separation of Ru-Pd-Ir-Re-Pt from Y, Zr, Hf</b>	
Eichrom-LN resin (100-150µm): 0.5 ml	
Column dimension: 4 mm wide × 45 mm long	
Resin cleaning	3 ml 0.5 mol l <sup>-1</sup> HF
Resin cleaning	3 ml Mili-Q
Resin cleaning	6 ml 6 mol l <sup>-1</sup> HCl
Resin cleaning	3 ml Mili-Q
Conditon	3 ml 0.5 mol l <sup>-1</sup> HCl
Load and collect sample	0.5 ml 0.5 mol l <sup>-1</sup> HCl
Collect sample	2.5 ml 0.5 mol l <sup>-1</sup> HCl
<b>(3) Purification of Pd from Zr and Cd</b>	
Chelex100(200-400 mesh, sodium form) : 0.1 ml	
Column dimension: 4 mm wide × 10 mm long	
Resin cleaning	9 ml 9.5 mol l <sup>-1</sup> HCl
Resin cleaning	3 ml Mili-Q
Conditon	3 ml 0.5 mol l <sup>-1</sup> HNO <sub>3</sub>
Load and collect sample	0.5ml 0.5 mol l <sup>-1</sup> HNO <sub>3</sub>
Collect sample (Ru-Re-Ir-Pt fraction)	4 ml 0.5 mol l <sup>-1</sup> HNO <sub>3</sub>
Collect sample (Pd fraction)	3 ml 8 mol l <sup>-1</sup> HCl
<b>(4) Purification of Ru-Re-Ir-Pt from Cr</b>	
AG50WX8 (200-400 mesh): 0.3 ml	
Column dimension: 4 mm wide × 30 mm long	
Resin cleaning	6 ml 6 mol l <sup>-1</sup> HCl
Resin cleaning	3 ml Mili-Q
Conditon	3 ml 0.5 mol l <sup>-1</sup> HNO <sub>3</sub>
Load and collect sample	0.3 ml 0.5 mol l <sup>-1</sup> HNO <sub>3</sub>
Collect sample	0.6 ml 0.5 mol l <sup>-1</sup> HNO <sub>3</sub>

Table 2.2. ICP-MS operating conditions

Parameter	Remark
Instrument	Thermo SCIENTIFIC Element XR
Plasma power	1200W
Torch	Quartz glass torch with a sapphire injector
Plasma Ar gas flow rate	16 l min <sup>-1</sup>
Auxiliary Ar gas flow rate	0.8-0.9 l min <sup>-1</sup>
Sampling orifice	1 mm (made of Ni)
Skimming orifice	0.8 mm (made of Ni)
Background correction	Measured before each sample, after a 550s wash
Data acquisition	Continuous nebulisation with a sample uptake time of 40s
Low resolution mode	127s with 5 scans
Desolvator	Aridus II (CETAC Technologies, USA)
Nebulizer	Micro-flow PFA nebulizer, PFA-50, self-aspiration
Spray chamber	PFA Spray chamber
Spray chamber temperature	110 °C
Desolvator temperature	160 °C
Sweep gas (Ar)	~3.52-5.69 l min <sup>-1</sup>
Nitrogen gas	~2-6 ml min <sup>-1</sup>
Nebulizer Ar gas flow rate	~0.73-0.84 l min <sup>-1</sup> 0.7 l min <sup>-1</sup> with Aridus
Typical sensitivity	~1.5 × 10 <sup>5</sup> cps ng <sup>-1</sup> ml <sup>-1</sup> for <sup>106</sup> Pd at LR mode ~6 × 10 <sup>5</sup> cps ng <sup>-1</sup> ml <sup>-1</sup> for <sup>106</sup> Pd at LR mode with Aridus

Table 2.3. Potential isobaric and polyatomic interferences for HSEs.

HSE isotopes	Interference		HSE isotopes	Interference			
	isobaric	polyatomic		isobaric	polyatomic		
<sup>99</sup> Ru		<sup>62</sup> Ni <sup>37</sup> Cl	<sup>106</sup> Pd	<sup>106</sup> Cd	<sup>88</sup> Sr <sup>16</sup> O <sup>1</sup> H		
		<sup>64</sup> Ni <sup>35</sup> Cl			<sup>68</sup> Zn <sup>37</sup> Cl		
		<sup>64</sup> Zn <sup>35</sup> Cl			<sup>70</sup> Ge <sup>35</sup> Cl		
		<sup>61</sup> Ni <sup>38</sup> Ar			<sup>90</sup> Zr <sup>16</sup> O		
		<sup>63</sup> Cu <sup>36</sup> Ar			<sup>89</sup> Y <sup>16</sup> O <sup>1</sup> H		
		<sup>59</sup> Co <sup>40</sup> Ar			<sup>66</sup> Zn <sup>40</sup> Ar		
	<sup>101</sup> Ru				<sup>53</sup> Cr <sup>16</sup> O <sub>3</sub>	<sup>185</sup> Re	<sup>169</sup> Tm <sup>16</sup> O
					<sup>85</sup> Rb <sup>16</sup> O	<sup>187</sup> Re	<sup>171</sup> Yb <sup>16</sup> O
					<sup>66</sup> Zn <sup>35</sup> Cl	<sup>191</sup> Ir	<sup>175</sup> Lu <sup>16</sup> O
					<sup>64</sup> Zn <sup>37</sup> Cl		<sup>140</sup> Ce <sup>35</sup> Cl <sup>16</sup> O
		<sup>84</sup> Sr <sup>16</sup> O <sup>1</sup> H	<sup>193</sup> Ir	<sup>177</sup> Hf <sup>16</sup> O			
		<sup>61</sup> Ni <sup>40</sup> Ar		<sup>140</sup> Ce <sup>37</sup> Cl <sup>16</sup> O			
		<sup>64</sup> Ni <sup>37</sup> Cl	<sup>194</sup> Pt	<sup>178</sup> Hf <sup>16</sup> O			
		<sup>65</sup> Cu <sup>36</sup> Ar	<sup>195</sup> Pt	<sup>179</sup> Hf <sup>16</sup> O			
<sup>105</sup> Pd			<sup>89</sup> Y <sup>16</sup> O		<sup>178</sup> Hf <sup>16</sup> O <sup>1</sup> H		
			<sup>65</sup> Cu <sup>40</sup> Ar				

Table 2.4. Collection schemes of Os isotope measurement for the static mode and peak-jumping mode.

Cup	L3	L2	L1	C	H1	H2	H3
Amplifier( $\Omega$ )	$10^{12}$	$10^{11}$	$10^{11}$	$10^{11}$	$10^{11}$	$10^{11}$	$10^{11}$
Os isotope mass	$^{184}\text{Os}^{16}\text{O}_3^-$	$^{186}\text{Os}^{16}\text{O}_3^-$	$^{187}\text{Os}^{16}\text{O}_3^-$	$^{188}\text{Os}^{16}\text{O}_3^-$	$^{189}\text{Os}^{16}\text{O}_3^-$	$^{190}\text{Os}^{16}\text{O}_3^-$	$^{192}\text{Os}^{16}\text{O}_3^-$
	IC1 C						
Os isotope mass	$^{192}\text{Os}^{16}\text{O}_3^-$	$^{190}\text{Os}^{16}\text{O}_3^-$	$^{189}\text{Os}^{16}\text{O}_3^-$	$^{188}\text{Os}^{16}\text{O}_3^-$	$^{187}\text{Os}^{16}\text{O}_3^-$	$^{186}\text{Os}^{16}\text{O}_3^-$	



Table 2.6. Measurement of  $^{17}\text{O}/^{16}\text{O}$  and  $^{18}\text{O}/^{16}\text{O}$  ratios during each analytical session.

236	238	239	240	241	242
<b>188Os.16O<sub>3</sub></b>	<b>190Os.16O<sub>3</sub></b>	<b>190Os.16O<sub>2</sub>.17O</b>	<b>192Os.16O<sub>3</sub></b>	<b>192Os.16O<sub>2</sub>.17O</b>	<b>192Pt.16O<sub>2</sub>.18O</b>
			190Os. <b>16O<sub>2</sub>.18O</b>	190Os. <b>16O.17O.18O</b>	190Os. <b>16O.18O<sub>2</sub></b>
			190Os. <b>16O.17O<sub>2</sub></b>	190Os. <b>17O<sub>3</sub></b>	190Os. <b>17O<sub>2</sub>.18O</b>

Table 2.7. Distribution coefficient ( $K_d$ ) of HSEs and interfering elements in Ln resin and Chelex 100 determined from this study.

		<b>Ru</b>	<b>Pd</b>	<b>Re</b>	<b>Ir</b>	<b>Pt</b>	<b>Y</b>	<b>Zr</b>	<b>Cd</b>	<b>Hf</b>
Ln resin	0.5 mol l <sup>-1</sup> HCl	1	0.3	11	1	2	5.4X10 <sup>2</sup>	9X10 <sup>6</sup>	1	3X10 <sup>11</sup>
	0.5 mol l <sup>-1</sup> HF	7	7	8	3	5	20	2	6	7
Chelex 100	0.5 mol l <sup>-1</sup> HNO <sub>3</sub>	6	1.3X10 <sup>3</sup>	20	8	14	0.4	2	2	2
	0.5 mol l <sup>-1</sup> HF	36	2.8X10 <sup>3</sup>	78	35	44	3	1	10	2
	8 mol l <sup>-1</sup> HCl	4	8	30	5	26	2	7	18	7

Table 2.8. Ratios of interferences intensities relative to the measured intensities of HSE isotope masses (cps/cps in parts per million) during ICP-MS measurement.

interference/isotope	Non-desilicification					Desilicification				
	UB-N	JP-1	MUH-1	OKUM	TDB-1	UB-N	JP-1	MUH-1	OKUM	TDB-1
$^{53}\text{Cr}^{16}\text{O}_3^+ / ^{101}\text{Ru}^+$	<1	<1	<1	<1	<1	<1	<1	<1	<1	<1
$^{89}\text{Y}^{16}\text{O}^+ / ^{105}\text{Pd}^+$	<1	<1	<1	<1	<1	<1	<1	<1	<1	<1
$^{90}\text{Zr}^{16}\text{O}^+ / ^{106}\text{Pd}^+$	13 ± 2	66 ± 119	3 ± 2	0.8 ± 0.3	<1	18 ± 6	53 ± 62	3 ± 1	1.6 ± 0.4	<1
$^{106}\text{Cd}^+ / ^{106}\text{Pd}^+$	100 ± 149	172 ± 188	140 ± 95	224 ± 153	23 ± 23	47 ± 15	127 ± 76	110 ± 25	233 ± 188	249 ± 225
$^{177}\text{Hf}^{16}\text{O}^+ / ^{193}\text{Ir}^+$	<1	<1	<1	<1	3 ± 4	<1	<1	<1	<1	26 ± 20
$^{178}\text{Hf}^{16}\text{O}^+ / ^{194}\text{Pt}^+$	<1	<1	<1	<1	<1	<1	<1	<1	<1	2 ± 2
$^{179}\text{Hf}^{16}\text{O}^+ / ^{195}\text{Pt}^+$	<1	<1	<1	<1	<1	<1	<1	<1	<1	1.5 ± 1

Table 2.9. HSE mass fractions (ng g<sup>-1</sup>) of UB-N, JP-1 and MUH-1 from this study.

No.	Ru	Pd	Re	Ir	Pt	Os	<sup>187</sup> Re/ <sup>188</sup> Os	<sup>187</sup> Os/ <sup>188</sup> Os
UB-N (serpentinite, CRPG)								
Carius tube without desilicification								
1	6.76	5.37	0.198	3.48	7.02	3.51	0.272	0.12727
2	6.49	5.47	0.193	2.82	6.42	3.45	0.270	0.12745
3	6.29	5.51	0.193	3.32	6.89	3.35	0.278	0.12676
4	6.02	5.44	0.182	3.37	7.08	3.27	0.269	0.12766
5	5.77	5.70	0.190	2.55	6.86	3.02	0.303	0.12692
6	6.17	5.85	0.198	3.05	7.25	3.41	0.280	0.12856
7	5.86	5.67	0.194	3.39	7.65	3.47	0.270	0.12709
8	6.01	5.84	0.193	3.06	7.32			
mean	6.17	5.61	0.192	3.13	7.06	3.35	0.278	0.12739
1 SD	0.33	0.18	0.005	0.32	0.37	0.17	0.012	0.00060
% RSD	5.4	3.3	2.6	10	5.2	5.0	4.4	0.47
Carius tube with post-Os desilicification								
1	6.72	5.62	0.198	2.94	6.73	3.09	0.309	0.12794
2	6.80	5.51	0.189	3.84	6.75			
3	6.50	5.68	0.199	3.71	6.91	3.47	0.277	0.12671
4	6.27	5.58	0.185	3.14	7.00	3.11	0.288	0.12707
5	6.62	5.64	0.190	3.81	6.65	3.25	0.282	0.12686
6	6.16	5.60	0.194	2.95	6.61	3.57	0.263	0.12676
7	7.14	5.58	0.192	2.77	6.37			
8	6.66	5.73	0.196	3.23	6.75	3.82	0.248	0.12660
9	5.54	6.573	0.193	2.78	6.77	3.24	0.287	0.12601
10	6.25	5.85	0.187	2.79	6.78	3.50	0.258	0.12738
mean	6.46	5.65	0.192	3.20	6.73	3.38	0.277	0.12692
1 SD	0.44	0.10	0.005	0.43	0.17	0.25	0.020	0.00057
% RSD	6.8	1.8	2.4	14	2.5	7.5	7.1	0.45
JP-1 (harzburgite, GSJ)								
Carius tube without desilicification								
1	4.61	1.35	0.0293	2.19	4.23	3.45	0.0411	0.12221
2	3.84	1.46	0.0299	1.98	3.52	2.35	0.0613	0.11961
3	3.65	1.32	0.0281	1.98	3.37	2.31	0.0589	0.11978
4	3.08	1.51	0.0264	1.55	3.62			
5	4.39	1.65	0.0306	2.72	5.38	3.52	0.0420	0.12187
6	4.78	1.22	0.0307	2.84	4.61	3.84	0.0386	0.12183
7	4.82	1.18	0.0275	2.56	4.43	3.04	0.0437	0.11930
8	4.49	1.27	0.0255	2.25	3.83	2.75	0.0448	0.12019
mean	4.21	1.37	0.0285	2.26	4.12	3.04	0.0472	0.12069
1 SD	0.62	0.16	0.0019	0.43	0.67	0.60	0.0091	0.00124
% RSD	15	12	6.8	19	16	20	19	1.0
Carius tube with post-Os desilicification								
1	4.53	1.39	0.0266	2.52	4.45	2.73	0.0470	0.12051
2	7.13	1.33	0.0277	4.13	4.42	2.46	0.0544	0.11945
3	5.56	1.19	0.0282	1.82	6.69	3.86	0.0354	0.11883
4	3.98	1.19	0.0307	2.38	4.42	3.40	0.0367	0.12173
5	4.89	1.49	0.0292	2.63	5.89	3.15	0.0447	0.12061
6	3.93	1.18	0.0301	2.16	3.90	2.35	0.0618	0.12139
7	4.96	1.19	0.0221	2.69	3.93	2.57	0.0416	0.12047
8	3.71	1.26	0.0282	2.09	3.81	3.78	0.0360	0.11988
mean	4.84	1.28	0.0279	2.55	4.69	3.12	0.0447	0.12036
1 SD	1.12	0.11	0.0027	0.70	1.04	0.69	0.0095	0.00096
% RSD	23	8.9	10	27	22	22	21	0.80
MUH-1 (harzburgite, IAG)								
Carius tube without desilicification								
1	5.56	10.5	0.166	2.31	7.36	3.43	0.234	0.12757
2	7.54	7.14	0.172	2.64	7.23	4.54	0.183	0.12652
3	5.87	7.98	0.175	2.20	7.22	2.93	0.287	0.12797
4	5.04	8.32	0.170	2.49	10.3	3.31	0.248	0.12837
5	7.65	9.60	0.179	2.70	9.01	4.17	0.207	0.12794
mean	6.33	8.71	0.172	2.47	8.23	3.68	0.232	0.12767
1 SD	1.19	1.34	0.005	0.21	1.39	0.66	0.040	0.00070
% RSD	19	15	2.7	8.6	17	18	17	0.55
Carius tube with post-Os desilicification								
1	7.33	7.95	0.187	2.08	7.72	3.58	0.252	0.12714
2	5.61	10.3	0.189	2.50	9.33	3.12	0.293	0.12812
3	6.45	8.49	0.177	2.20	7.01	4.64	0.185	0.12761
4	6.36	8.02	0.185	2.46	7.60	3.53	0.253	0.12691
mean	6.44	8.69	0.185	2.31	7.92	3.72	0.246	0.12744
1 SD	0.71	1.10	0.005	0.20	0.99	0.65	0.045	0.00054
% RSD	11	13	2.8	9	13	17	18	0.42

Uncertainties (2SE given in italic, refer to least significant digits) on each sample are calculated by error propagation, which includes uncertainties of isotope ratio, spike concentration, and blank correction.

Table 2.10. HSE mass fractions (ng g<sup>-1</sup>) of OKUM and TDB-1 from this study.

No.	Ru	Pd	Re	Ir	Pt	Os	<sup>187</sup> Re/ <sup>188</sup> Os	<sup>187</sup> Os/ <sup>188</sup> Os								
OKUM (komatiite, IAG)																
Carius tube without desilicification																
1	4.04	4	11.1	1	0.454	4	0.776	9	10.3	2	0.765	11	2.87	5	0.2642	3
2	3.93	4	11.4	1	0.445	4	0.790	8	9.99	20	0.767	11	2.80	5	0.2629	3
3	3.99	4	12.6	1	0.472	5	0.784	9	10.1	2	0.780	11	2.92	5	0.2632	6
4	4.04	4	10.5	1	0.462	5	0.763	8	10.2	2	0.737	10	3.03	5	0.2741	3
5	3.86	4	10.7	1	0.450	4	0.730	8	10.4	2	0.696	10	3.12	5	0.2791	3
mean	3.97		11.3		0.456		0.769		10.2		0.749		2.95		0.2687	
1 SD	0.08		0.83		0.011		0.024		0.1		0.034		0.13		0.0074	
% RSD	1.9		7.3		2.4		3.1		1.4		4.5		4.3		2.8	
Carius tube with post-Os desilicification																
1	4.40	4	11.2	1	0.493	5	1.02	1	11.5	1	0.962	13	2.47	4	0.2302	3
2	4.45	4	11.6	1	0.502	5	0.847	10	11.8	1	0.669	9	3.62	6	0.2912	3
3	4.32	4	11.7	1	0.466	5	0.907	12	11.5	1	0.778	11	2.89	5	0.2576	2
4	4.40	4	10.6	1	0.459	5	1.02	1	11.3	1	1.01	1	2.19	4	0.2266	1
mean	4.39		11.3		0.480		0.951		11.5		0.855		2.80		0.2514	
1 SD	0.05		0.5		0.021		0.088		0.2		0.160		0.62		0.0299	
% RSD	1.2		4.4		4.3		9.3		1.7		19		22		12	
TDB-1 (diabase, CCRMP)																
Carius tube without desilicification																
1	0.184	2	23.9	12	0.924	10	0.067	0	4.41	4	0.116	2	38.6	7	0.976	2
2	0.184	2	25.0	23	0.924	11	0.061	0	4.13	5	0.111	2	40.0	7	0.972	1
3	0.212	2	27.7	18	0.916	10	0.089	0	4.74	5						
4	0.182	2	26.0	18	0.927	10	0.058	0	4.03	4						
5	0.191	2	21.6	7	0.931	19	0.085	0	5.39	6	0.140	2	32.2	8	0.829	1
6	0.185	2	21.3	6	0.895	18	0.069	0	4.50	5	0.118	2	36.6	9	0.917	4
7	0.194	2	22.8	6	0.917	17	0.068	0	4.77	4	0.115	2	38.4	9	0.951	3
8	0.191	2	21.9	5	0.916	16	0.072	0	4.51	4	0.120	2	37.0	9	0.915	2
mean	0.190		23.8		0.919		0.071		4.56		0.120		37.1		0.927	
1 SD	0.010		2.3		0.011		0.011		0.42		0.010		2.7		0.055	
% RSD	5.2		9.7		1.2		15		9.3		8.4		7.4		5.9	
Carius tube with post-Os desilicification																
1	0.223	2	23.4	10	1.03	2	0.063	0	5.17	4	0.106	2	46.6	10	1.028	2
2	0.270	2	23.1	10	1.12	2	0.089	0	4.92	4						
3	0.245	2	24.3	9	0.969	16	0.097	0	5.23	4						
4	0.233	2	23.5	9	0.977	16	0.068	0	4.61	3						
5	0.255	3	21.8	4	0.978	16	0.072	0	4.38	5	0.118	2	40.2	9	0.924	5
6	0.241	2	22.8	4	0.951	16	0.066	0	4.60	5	0.106	2	43.2	10	1.003	2
7	0.269	3	22.9	5	0.973	17	0.085	0	4.89	6	0.128	2	36.7	8	0.813	2
8	0.256	3	21.8	4	0.964	16	0.142	1	4.47	5	0.135	2	34.5	8	0.845	2
mean	0.249		23.0		0.994		0.085		4.78		0.119		40.3		0.923	
1 SD	0.017		0.8		0.054		0.026		0.32		0.013		4.8		0.094	
% RSD	6.7		3.7		5.4		30		6.6		11		12		10	

Uncertainties (2SE given in *italic*, refer to least significant digits) on each sample are calculated by error propagation, which includes uncertainties of isotope ratio, spike concentration, and blank correction.

## **Chapter 3: Osmium isotopes and highly siderophile elements in Horoman peridotite massif, Japan**

## 1. Introduction

Understanding the geochemical behavior of the HSEs in the Earth's mantle is useful to assess multiple processes including such as mantle melting coupled with melt extraction to form crust, mantle metasomatic interactions/refertilisation, and crustal recycling via the plate tectonic cycle (e.g., Martin 1991, Rehkämper et al. 1999, Becker et al. 2001b, Walker et al. 2002, Luguët et al. 2007, Le Roux et al. 2007, Lorand et al. 2009). The HSE abundances are dominantly distributed in trace sulfides and alloys, which can be strongly affected by melting and metasomatic processes, thus, distinguishable from the behavior of constituent minerals. Typically, the apparent partition coefficients of the HSEs between peridotite and basaltic melt is ~10 for Os, Ir and Ru and ~0.1 for Re, Pt, and Pd, resulting the former should be retained more in the mantle residue, whereas the latter more in the basaltic melt during partial melting (Bockrath et al. 2004). The contrasting fractionation behavior of HSEs leads to the generations of characteristic siderophile element signatures, and provides a robust tool to constrain the extent and timing of the processes involved. For example, lherzolites and harzburgites in general have similar trends of Os-Ir-Ru abundances, whereas, the concentrations of Pt-Pd-Re are typically much lower in harzburgites than in lherzolites. Additionally, the  $^{187}\text{Re}$ - $^{187}\text{Os}$  isotope system, in some instances, could be used to place chronological constraints on when these processes occurred.

Tectonically emplaced mantle rocks, such as orogenic peridotite massifs, provide a principle constraint on the composition and multiple processes in the Earth's upper mantle. Compared with mantle xenoliths, peridotite massifs have the advantage of the large-scale exposure of textural and compositional relations between different rock types, which can provide more detailed geochemical and structural information about such as the scale of heterogeneity, the timing of melting, melt/ fluid-rock interactions, and deformation processes in the evolutions of the Earth's mantle.

The Horoman peridotite massif is one of the least altered peridotite massifs in the world (Niida, 1984). Horoman peridotite massif preserves the unique chemical and isotopic compositions in the upper mantle. In particular, the fertile massive plagioclase lherzolite samples from Horoman massif have the least radiogenic Pb isotopic composition among so far reported peridotite materials on the Earth (Malaviarachchi et al. 2008), providing the key information to geochemically characterise the most depleted end component of the Earth's upper mantle. The another advantage of the Horoman peridotite massif is that there exist the comprehensive data sets, including major and trace elements and H-Li-O-Sr-Nd-Hf-Pb isotopic compositions (e.g., Yoshikawa and Nakamura 2000, Malaviarachchi et al. 2008, Malaviarachchi et al. 2010, Ranaweera et al. 2018). In order to further understand the evolution and dynamics of the Earth's mantle, we reckon that Horoman peridotite massif is a suitable candidate, which may be able to discover unknown mantle processes via the new investigation of HSE behavior.

The HSE abundances and Os isotopic compositions of Horoman peridotite samples were reported by Rehkämper et al. (1999) and Saal et al. (2001), respectively. The suprachondritic Pt/Ir and Pd/Ir ratios observed in plagioclase lherzolites were explained by melt addition to a depleted peridotite from sulfide derived from percolating magmas with or without addition of basaltic melts (Rehkämper et al. 1999). Saal et al. (2001) also suggested that Re-Os isotope data supported the refertilisation process which was first mentioned by Obata and Nagahara (1987). The refertilisation process could be explained by adding a mid-ocean ridge basalt (MORB)-like component to a depleted peridotite, under the observation of the depleted Os isotopic signature and the suprachondritic  $^{187}\text{Re}/^{188}\text{Os}$  ratios in plagioclase lherzolites (Saal et al. 2001). However, their studies did not consider other isotope systems of lithophile elements. Hence, in order to more comprehensively understand mantle processes in Horoman peridotite massif, the newly obtained data of HSE abundances and Os isotope ratios for a suite of Horoman samples were presented in this study, ranging from the fertile plagioclase lherzolites

through refractory spinel lherzolites, highly depleted spinel hazrburgites, to the subordinated dunite, which have been analysed for major and trace elements and H-Li-O-Sr-Nd-Hf-Pb isotopic compositions. With combination of these various isotope dataset, it could possibly give the new and important insights into the genesis and evolutional processes of the Earth's mantle.

## **2. Geological setting and previous studies**

### **2.1. Geological setting**

Hokkaido Island is considered to have been formed by the collision and amalgamation of several crustal blocks between the Northeast Japan Arc and the Kuril Arc (e.g., Jolivet et al. 1988). The Hidaka Mountains, together with the surrounding area, have experienced collision-related deformation and modification. Hence, the southcentral part of Hokkaido is called the Hidaka collision zone, and the collision zone consists of the Horoman peridotite massif and other metamorphic rocks of the Hidaka metamorphic belt (Figure 3.1).

The Hidaka metamorphic belt extends NNW-SSE for ~ 120 km, with a maximum width of ~20 km. The structure of the Hidaka metamorphic belt is west-vergent, and the metamorphic grade increases from east to west up to granulite facies pressure-temperature conditions (e.g., Komatsu et al. 1983). In the southernmost part of the Hidaka metamorphic belt, the granulite-facies metamorphic zones are situated surrounding the Horoman peridotite massif, and their distribution extends to ~ 10 km to the southeast (Shiba et al. 1992). The western border of the Hidaka metamorphic belt is bounded by the Hidaka Main Thrust, where the rocks of the Hidaka metamorphic belt on the hanging wall are distinguished from an ophiolitic sequence of the Poroshiri ophiolite (e.g., Miyashita 1983) and a Cretaceous-Paleogene accretionary complex of the Idon'napu belt (e.g., Kiyokawa 1992). Metasediments of the eastern part of the Hidaka metamorphic belt are lithologically continuous with

the early Paleogene sedimentary sequence of the Nakanogawa Group (e.g., Nanayama 1992). It is suggested that the Hidaka metamorphic belt was a crustal fragment of either island arc or continent, and was considered to be an exposed cross-section of magmatic arc and its tectonic evolution has been widely discussed from previous studies (e.g., Osanai et al. 1991, Toyoshima et al. 1994).

Several independent bodies of ultramafic rocks are discovered in the northern and southern areas of the Hidaka metamorphic belt (Komatsu and Nochi 1966, Niidda and Katoh 1978, Niidda and Takazawa 2007). In the northern part of the belt, five peridotite complexes (i.e., Uenezaru, Pankenuushi, Tottabetsu, Oku-Niiappu, Koibokushushibichari) are lined up from north to south along the Hidaka Main Thrust. On the other hand, in the southern part of the Hidaka metamorphic belt, the Menashunbetsu and Horoman peridotite complexes are situated in the western margin of the belt, and three additional small peridotite bodies (i.e., Pon-Nikanbetsu, Nikanbetsu, Abeyaki) are lined up from the eastern part of the Horoman peridotite massif to the southeast in the Hidaka metamorphic belt (Niidda and Takazawa 2007). The Horoman peridotite massif is incomparably larger than the other ultramafic bodies in the Hidaka metamorphic belt.

The Horoman peridotite massif is exposed along the Hidaka Main Thrust between a continental or island arc crust-mantle section and a metamorphosed oceanic crust-mantle section (Figure 3.1). To the west the massif is bordered by a thrust fault involving meta-gabbro, greenschist and blackschist, which constitute metaophiolite and contact with the non-metamorphosed sedimentary rocks. The eastern and northern margins of the Horoman massif are irregularly bounded by NW-SE striking faults and shear zones. The serpentinisation has been developed locally at the margin, faults and shear zones, nevertheless, the massif is essentially unaltered (Niidda 1984).

The Horoman peridotite massif is an Alpine-type ultramafic body (orogenic peridotite), and covers an area of ~ 80 km<sup>2</sup> and is > 3 km thick (Figure 3.2). The ultramafic rocks of the Horoman massif are almost entirely composed of olivine, orthopyroxene and clinopyroxene. Plagioclase, spinel and amphibole are important minor constituents. The massif consists of several well developed layered lithological sequences of the several rock types. The ultramafic type, which comprises of more than 95% of the Horoman massif, includes plagioclase lherzolite, lherzolite, harzburgite, dunite, orthopyroxenite and clinopyroxenite. Plagioclase lherzolite, lherzolite and dunite are the representatives of the Horoman layered massif (Niida 1984). Minor amounts of pyroxenite and mafic layers are concordantly interlayered in the peridotites parallel to their compositional layering and foliation. The foliation is defined by aligned flay mica, ellipsoidal plagioclase, and flattened quartz aggregates (Yamamoto et al. 2010).

## **2.2. Previous petrological and geochemical significance**

The Horoman peridotite massif exhibits a well-developed compositional layering on a scale of centimeters to several hundred meters, which is divided into two stratigraphic zones (Niida 1984): the Upper Zone where the layers are thinner and mafic layers are more abundant, and the Lower Zone where layers define lithological sequences of ~100 to 500 meters. Based on the petrological features, the Horoman peridotite massif has been subdivided into three suites: Main Harzburgite-Lherzolite (MHL), Banded Dunite-Harzburgite (BDH), and Spinel-rich Dunite-Wehrlite (SDW) suites (Takahashi, 1991). As described former, the MHL suite, as the major part of the Horoman peridotite massif, consists of plagioclase lherzolite, spinel lherzolite and harzburgite, which has been interpreted as the residues formed after partial melting of mid-ocean ridge basalt (MORB) source mantle (Frey et al. 1991, Takahashi 1991, Takazawa et al. 1996, Yoshikawa and Nakamura 2000, Malaviarachchi et al. 2008). On the other hand, BDH and SDW suites are considered as cumulates segregated from different

magma sequences (Takahashi, 1991). Horoman peridotite massif also contain two dominant mafic layers which were injected under the pressure ranging from the garnet stability (Type I) to plagioclase stability (Type II) fields (Niida 1984, Takazawa et al. 1999).

Major element compositions of peridotite samples in MHL suite showed systematic trend from the fertile plagioclase lherzolite, spinel lherzolite to refractory harzburgite: the inverse linear trends of SiO<sub>2</sub>, TiO<sub>2</sub>, Al<sub>2</sub>O<sub>3</sub>, CaO, and Na<sub>2</sub>O contents with MgO contents (Frey et al. 1991, Takazawa et al. 2000, Yoshikawa and Nakamura 2000). The abundances of heavy rare earth element (HREE) compositions consistently decrease from plagioclase lherzolite, spinel lherzolite to harzburgite (Figure 3.3). Model calculation of these major and trace element compositions of MHL suite samples indicates the near fractional melting from the MORB-source mantle under polybaric conditions from the garnet to spinel stability fields (Takazawa et al. 2000, Yoshikawa and Nakamura 2000). The enrichment of incompatible light rare earth element (LREE) in spinel lherzolite and harzburgite (Figure 3.3) was inferred by slab fluid metasomatism after melt extraction (Yoshikawa and Nakamura 2000, Malaviarachchi et al. 2008).

Yoshikawa and Nakamura (2000) classified the peridotites in MHL suite into two subgroups. One group which is referred to as DP, which is characterised by the higher  $\epsilon\text{Nd}$  values ( $\epsilon\text{Nd} > +10$ ) with more depleted LREE patterns ( $[\text{Ce}/\text{Yb}]_N < 0.5$ ). The other group which is referred to as EP which is enriched in Nd isotopic compositions ( $\epsilon\text{Nd} < +6$ ) and has relatively variable and enriched LREE patterns. Takazawa et al. (2000) also classified the MHL suite into two subgroups. The first group which is referred as N-type with relatively high CaO, Al<sub>2</sub>O<sub>3</sub>, Na<sub>2</sub>O, TiO<sub>2</sub> contents with lower Mg numbers, these samples are the most fertile peridotites in Horoman massif and compositionally similar to the source of the MORB; by contrast, the another group which is referred as E-type, which has the

relatively lower concentrations of CaO, Al<sub>2</sub>O<sub>3</sub>, Na<sub>2</sub>O, TiO<sub>2</sub>, Yb, and higher Mg number.

### **3. Sample description**

#### **3.1. Petrography and petrology**

The Horoman peridotite massif from this study contains fertile plagioclase lherzolite, refractory spinel lherzolite to highly depleted spinel harzburgite with subordinate dunite, pyroxenite and gabbro (Figure 3.2). The major lithology of the Horoman peridotite massif is classified as the massive peridotite (MSP) and the thin-layer peridotite (TLP). The MSP occurs as massive rocks, composed of plagioclase lherzolites, spinel lherzolites and harzburgites, with a thickness of >1 meter. The TLP as a layer in a few millimeters to centimeters thickness, composed of plagioclase lherzolite and harzburgite, interlayered with gabbros (Figure 3.4).

The sample location, petrographical and petrological descriptions of the analysed samples have been described elsewhere (Malaviarachchi et al. 2010, Ranaweera et al. 2018). Thus, they are briefly summarised as below.

##### **3.1.1. Massive plagioclase lherzolite**

The plagioclase lherzolites of the MSP (P-MSP) have porphyroclastic textures of olivine (Ol), orthopyroxene (Opx), clinopyroxene (Cpx), plagioclase (Pl) and spinel (Spl). Olivine is generally anhedral, and Opx and Cpx contain exsolution lamellae. In all samples, very fine-grained aggregates (<100 µm) of Pl, Ol, Spl and rare Opx were observed. Sample 0901-4 contains two-pyroxene-Spl symplectites.

##### **3.1.2. Massive spinel lherzolite and harzburgite**

The spinel lherzolites of the MSP (S-MSP) contain Ol, Opx, Cpx and Spl. These samples also have porphyroclastic (3-10 mm) textures and contain two-pyroxene-spinel symplectites. Exsolution lamellae in pyroxenes and symplectitic, fine-grained (<100  $\mu\text{m}$ ), aggregates of Opx, Cpx and Spl are common. Porphyroclastic harzburgite samples in the MSPs are composed of Ol, Opx, Spl and rare Cpx, with exsolution lamellae in pyroxene porphyroclast. Harzburgites samples in the MSPs are composed of Ol, Opx, Spl and rare Cpx, with exsolution lamellae in pyroxene porphyroclasts. Two-pyroxene-spinel symplectites and fine-grained aggregates of Opx, Cpx and Spl were observed.

### **3.1.3. Massive dunite**

The massive dunite occurs with the accompanied harzburgite. It consists of Ol (~92 vol. %), chromian Spl (~7 vol. %) and trace amount of Cpx (< 2 vol. %). Most Ol is subhedral neoblast and equigranular (300-500  $\mu\text{m}$ ), and minor porphyroclastic Ol is coarse-grained (2-4 mm). The Spl is scattered in the rock, and occurs as fine-grained euhedral crystal (100 - 500  $\mu\text{m}$ ) and coarse-grained spindle-shaped grains (1-5 mm). Trace Cpx is anhedral neoblast (0.1-1.5 mm) in Ol matrix, and is locally concentrated to form Cpx-bearing band (2-5 mm).

### **3.1.4. Thin-layer peridotite**

In the TLPs, inter-mineral grain boundaries have partly been distorted, creating wide, irregular interfacial angles, where primary mineral porphyroclast are fully or partially dissolved as a consequence of melt-rock reaction.

## **3.2. Major and trace element compositions and H-Li-O-Sr-Nd-Hf-Pb isotopes**

Major- and trace-element abundances of lithophile elements, volatile elements (H, B, Cl, F, S), H-Li-O-Sr-Nd-Hf-Pb isotope abundances of the analysed samples were reported elsewhere (Malaviarachchi

et al. 2008, Malaviarachchi et al. 2010, Ranaweera et al. 2018). The systematic trends of petrologic characteristics, major elements and rare earth elements (REE) compositions ranging from the fertile plagioclase lherzolite, spinel lherzolite to refractory harzburgite (Figure 3.3) have been interpreted to be the result of variable degrees of partial melting from the MORB-source mantle. Most plagioclase lherzolites of the MSP from this study showed nearly flat HREE and smooth LREE depleted REE patterns in the CI chondrite-normalised diagram (Figure 3.5), which are regarded as the partial melting residues (Malaviarachchi et al., 2008). The HREEs showed variable values, in particular, the HREE in the 0904-1 series and the top layer of TLP are lower than the others. By contrast, the spinel lherzolite and harzburgite were depleted in HREEs but enriched in LREEs and Pb, Ba, Rb and Cs concentrations (Figure 3.3), probably due to the slab-fluid metasomatism after melt extraction (Malaviarachchi et al. 2008). The TLPs also showed smooth REE patterns similar P-MSP, but their absolute REE abundances extends to higher values than the massive plagioclase lherzolites (Figure 3.5).

Moreover, based on the chemical and isotope data, the MSPs have been classified into three types (Yoshikawa and Nakamura 2000, Malaviarachchi et al. 2008, Ranaweera et al. 2018) as follows: (1) depleted plagioclase lherzolite (DP-MSP, 0901-4 and 0902-2 series), enriched plagioclase lherzolite (EP-MSP, 0902-8 and 0904-1 series), and enriched spinel lherzolite and harzburgite (ES-MSP, all massive spinel lherzolites and harzburgites). DP-MSP is characterised by lower  $^{87}\text{Sr}/^{86}\text{Sr}$  ratios, higher  $\text{Al}_2\text{O}_3$  content and HREE abundances (Figure 3.6), and higher  $^{143}\text{Nd}/^{144}\text{Nd}$  ratio and  $\delta^7\text{Li}$  values than those of the EP-MSP. The DP-MSP are also characterised by lower La/Sm ratio than the EP-MSP, except for sample 0902-2. Both the DS-MSP and EP-MSP were inferred as the melt-extracted residues at the MOR at circa 1 Ga (Malaviarachchi et al. 2008, Ranaweera et al. 2018). The Pb and Hf isotopic compositions did not show clear differences among DP-MSPs and EP-MSPs. ES-MSP is characterised by higher La/Sm,  $^{87}\text{Sr}/^{86}\text{Sr}$ ,  $^{176}\text{Hf}/^{177}\text{Hf}$  ratios, radiogenic Pb isotopic composition, and lower

$^{143}\text{Nd}/^{144}\text{Nd}$  ratio than DP- and EP-MSPs. The chemical and isotopic compositions of T-TLP resemble to P-MSP. The other TLPs are enriched in HREE and  $^{87}\text{Sr}/^{86}\text{Sr}$  ratio than the other plagioclase lherzolites and show lower  $^{207}\text{Pb}/^{204}\text{Pb}$  ratio at a given  $^{206}\text{Pb}/^{204}\text{Pb}$  ratio than the other plagioclase lherzolites.

The O isotopic compositions of the Horoman peridotites presented evidently unmodified by fluids derived from recently juxtaposed Hidaka meta-sedimentary wall rocks with distinctively high  $\delta^{18}\text{O}$  (Figure 3.7). The significant variations of  $\delta^7\text{Li}$  values (by approximately 5 %) in the massive plagioclase lherzolites might be attributed to isotope fractionation in equilibrated silicate-fluid systems. The  $\delta\text{D}$  values of the massive peridotites were consistent with the lack of H isotope equilibrations with the mantle (Ranaweera et al. 2018).

It is inferred that the MSPs were produced initially by melt extraction from the MOR mantle at circa 1 Ga and by the following processes: (1) sub-seafloor hydrothermal (SSH) alteration at circa 1 Ga, (2) dehydration reactions in the oceanic lithosphere when the mantle was subducted, (3) interaction with slab-derived fluid during subduction (Malaviarachchi et al. 2008, Ranaweera et al. 2018). The enriched geochemical characteristics of EP-MSP and ES-MSP were caused by the third process, i.e., interaction with slab fluid. However, DP-MSP were rarely affected by the interaction of slab-derived fluid, thus preserving the initial melt extraction and subsequent SSH process in their geochemical characteristics.

The fertile composition of TLPs were also inferred to be interacted with MORB-like melt at circa 300 Ma (Malavirarachchi et al. 2010). Figure 3.4 suggests that the geochemical modification by basaltic melt-peridotite reaction was more dominated in the central to bottom layer of TLPs, however, it was the least affected for the top layers. In this study, thus, the TLPs are classified as top (T)-TLP (HR+55,

+20, and +12) and bottom (B)-TLP (HR+5 to HR-90), as shown in Figure 3.4.

## **4. Analytical methods**

### **4.1. Sample digestion and HSE separation**

The detailed analytical methods for measurements of the HSE mass fractions and Os isotope ratios were described in details in Chapter 2. Approximately 1 g of powdered samples prepared by Malaviarachchi et al. (2008) and Ranaweera et al. 2018) were mixed with ~ 0.3 g of HSEs mixed spike solution, then digested in the pre-cleaned CT with inverse aqua regia at 240 °C for 72 h. In this study, the HF-desilicification was not performed, as there is no significant difference between desilicified and non-desilicified HSE data for peridotites (see Chapter 2 in details). The Ru-Pd-Re-Ir-Pt bearing fraction and Os fraction were purified as also described in Chapter 2.

### **4.2. Mass spectrometric measurements**

#### **4.2.1. N-TIMS measurements for Os mass fraction and $^{187}\text{Os}/^{188}\text{Os}$ ratio**

During course of this study, a new TIMS, a Thermo Scientific TRITON Plus (Bremen, Germany), was installed in December 2017 at PML. Thus, we set up the analytical protocol of Os isotope analysis using this new TIMS. The TRITON Plus is equipped with nine Faraday cups, one secondary electron multiplier (SEM), and four compact discrete dynode multipliers (CDD). The configuration of amplifiers connected to the Faraday cups are three  $10^{13} \Omega$ , four  $10^{12} \Omega$ , and three  $10^{11} \Omega$  feedback resistors (Figure A1 in Appendix). The standard deviation of baseline noise of the amplifiers, measured by 12 blocks of each 72 cycle with integration and idle times of 4 and 3 sec, respectively, were 0.29-0.33  $\mu\text{V}$ , 0.69-0.90  $\mu\text{V}$ , and 1.4-2.1  $\mu\text{V}$  for  $10^{13} \Omega$ ,  $10^{12} \Omega$ , and  $10^{11} \Omega$  amplifiers, respectively. Gain factors for  $10^{11}$  and  $10^{12} \Omega$  resistors can be determined automatically using the stable reference current (1.20V for negative mode). However, gain factor of  $10^{13} \Omega$  resistors have to be determined

manually, because gain-board which can perform for auto-gain calibration had not been sold yet. The gain factors of the  $10^{13} \Omega$  amplifiers were measured once every day using the Os isotopic compositions of 50 ng of DROsS prior to the sample measurements. The method is modified after (Trinquier 2014). The sequence of gain calibration is shown in Table A1 in Appendix. The gain factor of each  $10^{13} \Omega$  resistors was calculated by  $^{187}\text{Os}/^{188}\text{Os}$  ratios measured by the average value of Seq. 1 and 5. Cup configuration, analytical sequence, and data reduction methods are same as TRITON. Figure A2 in Appendix shows the gain factors of three  $10^{13} \Omega$  resistors from this study, giving 311-362 parts per million during 8 months.

Relative internal precisions of  $^{187}\text{Os}/^{188}\text{Os}$  ratios against the  $^{188}\text{Os}^{16}\text{O}_3^-$  ion intensities are compared using the four sets of collectors: set 1 is  $10^{12} \Omega$  resistor for  $^{187}\text{Os}^{16}\text{O}_3^-$  intensity and  $10^{11} \Omega$  resistor for  $^{188}\text{Os}^{16}\text{O}_3^-$  intensity; set 2 is  $10^{13} \Omega$  resistor for  $^{187}\text{Os}^{16}\text{O}_3^-$  intensity and  $10^{11} \Omega$  resistor for  $^{188}\text{Os}^{16}\text{O}_3^-$  intensity; set 3 is  $10^{13} \Omega$  resistor for  $^{187}\text{Os}^{16}\text{O}_3^-$  intensity and  $10^{13} \Omega$  resistor for  $^{188}\text{Os}^{16}\text{O}_3^-$  intensity; and set 4 is using peaking-jumping mode (Figure A3 in Appendix). When the intensity of  $^{188}\text{Os}^{16}\text{O}_3^-$  was higher than  $\sim 100\text{mV}$ , the internal precisions of the set 1 and set 2 did not show clear differences. When the intensity of  $^{188}\text{Os}^{16}\text{O}_3^-$  was  $\sim 1$  to  $\sim 100\text{mV}$ , the internal precision was better using the set 1, 2, to 3. The peaking-jumping mode using ion counter was applied when the intensity of  $^{188}\text{Os}^{16}\text{O}_3^-$  was  $< \sim 5 \text{ mV}$ . The internal precisions of set 3 and set 4 were nearly identical when the intensities of  $^{188}\text{Os}^{16}\text{O}_3^-$  were 2 and 5 mV, but using set 4 was better when the  $^{188}\text{Os}^{16}\text{O}_3^-$  intensity was  $< 2\text{mV}$ . In this study, the Os measurement was performed using the three different sets (set 2, 3, and 4), depending on the  $^{188}\text{Os}^{16}\text{O}_3^-$  intensity.

The accuracy and precision of  $^{187}\text{Os}/^{188}\text{Os}$  ratios were evaluated using TRITON and TRITON Plus with different amplifiers of  $10^{11} \Omega$ ,  $10^{12} \Omega$ ,  $10^{13} \Omega$  resistors (Figure A4 in Appendix). When the sample

size of DROsS solution is ~ 50 ng, the  $^{187}\text{Os}/^{188}\text{Os}$  ratios were almost constant within 2 SD, using both TRITON ( $10^{11} \Omega$  resistor) and TRITON Plus ( $10^{12} \Omega$  resistor), however, when sample size is ~ 0.5-1 ng, the  $^{187}\text{Os}/^{188}\text{Os}$  ratios of TRITON ( $10^{11} \Omega$  resistor) were much variable than those of TRITON Plus using  $10^{13} \Omega$  resistor, even the errors for  $^{187}\text{Os}/^{188}\text{Os}$  ratios of TRITON Plus ( $10^{13} \Omega$  resistor) using ~0.1ng of DROsS solution were relatively lower than those of ~1ng of sample size obtained by TRITON ( $10^{11} \Omega$  resistor). Moreover, the  $^{187}\text{Os}/^{188}\text{Os}$  ratios seemed more variable when using peaking jumping mode using 0.1-1 ng of sample size, compared to the static mode. In conclusion, the  $^{187}\text{Os}/^{188}\text{Os}$  ratios obtained by TRITON Plus using  $10^{13} \Omega$  resistor gave more accurate and precise values when sample size is  $< \sim 1$  ng.

#### **4.2.2. ICP-MS measurements for other HSEs**

All other HSEs were measured by a sector-field ICP-MS Thermo Scientific Element XR, as described in Chapter 2.

#### **4.2.3. Total procedural blank**

The total procedural blanks of this study (n=5) were 4-7 pg for Os, 0-0.2 pg for Ir, 1-7 pg for Ru, 5-25 pg for Pt, 5-28 pg for Pd and 0.1-0.4 pg for Re, respectively (Table A2 in Appendix). In this study, the proportion of HSEs in blanks was  $< \sim 1\%$  for all HSEs for the Horoman peridotite samples, which were almost negligible. Although the proportions of blanks were low, all mass fractions and isotopic compositions were blank-corrected based on the measurement of blanks that were undertaken along with the measurement of all samples.

#### **4.2.4. External precision of reference material UB-N**

The external precision of the HSE during the analysis of the Horoman peridotite were tested by using

repeated analyses of the reference material UB-N. The external precision (defined as relative 1 standard deviation, n=5) of Os, Ir, Ru, Pt, Pd and Re concentration data is 8.4%, 12%, 8.7%, 5.9%, 3.4% and 5.2%, respectively, indicating that the Re, Pd and Pt are more reproducible than Ru, Os and Ir in UB-N. The external precision of  $^{187}\text{Os}/^{188}\text{Os}$  ratio was 0.36%. Generally, the HSE mass fractions and Os isotopic compositions obtained for UB-N from this study were in good agreement with the range of the previously reported data (Table A2 in Appendix).

## **5. Results**

### **5.1. Sample heterogeneity of peridotites**

Duplicate analyses of ~1 g test portions of sample powders were conducted for 7 Horoman peridotite samples (Table A3 in Appendix). The relative percentage differences (RPD) of the HSE mass fractions determined from duplicate samples were on average 15 % for Os, 5.6 % for Ir, 9.5 % for Ru, 10 % for Pt, 8.5 % for Pd and 13 % for Re. The maximum RPD between duplicate samples were ~20 % for Os, ~15 % for Ir, ~16 % for Ru, ~33 % for Pt, ~20 % for Pd and ~48 % for Re. It is indicated that Pt and Re seemed more heterogeneous than other HSEs in ~1g of Horoman powder samples.

### **5.2. HSE mass fractions**

HSEs exhibit contrasting behaviors during melting, with the platinum-PGE (PPGE: Pt, Pd, melting temperature <2000°C), and Re typically being more incompatible during melting and crystallization, relative to the iridium-PGE (IPGE: Os, Ir, Ru, melting temperature > 2000 °C; Barnes et al. 1985). For this reason, studies will often list the HSEs in order of relative incompatibility during melting for the investigations of mantle melting processes. Thus, the primitive upper mantle (PUM) normalised HSE abundances for Horoman peridotite samples were plotted in the order of apparent bulk peridotite-melt partition coefficients as  $\text{Os} \geq \text{Ir} \geq \text{Ru} \geq \text{Pt} \geq \text{Pd} \geq \text{Re}$  (e.g., Fisher-Godde et al. 2011) (Figure 3.8).

Generally, lherzolites and harzburgites have similar trends of Os-Ir-Ru abundances, whereas, the concentrations of Pt-Pd-Re are typically much lower in harzburgites than in lherzolites.

The HSE abundances of DP- and EP-MSP were 0.8 to 1.2 times of PUM compositions, except for anomalous Re abundances of 902-2 and 0904-1c with higher and lower values, respectively (Figure 3.8). The PUM-normalised IPGE showed basically two different patterns. All samples of 0901-4 series showed negative anomalies of Os and Ru, relative to Ir and Pt. Similar pattern can also be seen for 0902-2, 0904-1b, 0904-1c, and HR +20 from T-TLP. Other samples showed relatively smooth pattern without significant negative anomalies of Os and Ru. The sample 0902-2a of 0902-2 series had the same feature as 0901-4 series, except for the highly enriched in Re; sample 0902-2 had the trend of all depleted HSEs except for Ir. All samples of 0902-8 series kept almost flat HSE patterns compared to the PUM, only except for sample 0902-8a, which had the slight depletion of Os. The 0904-1 series show depleted HSE patterns relative to the PUM, excluding sample 0904-1a which only had depletion of Pd, and the more depleted Re was observed in sample 0904-1c. All three T-TLPs showed very scattered HSE patterns from each other. The sample HR+20 had the nearly same trend as 0901-4 series, however, HR+55 and HR+12 kept flat HSE patterns with the depletions of Pd and Re.

Among three spinel lherzolites, both 0901-1 and 0902-1 had the similar trend of HSE patterns, but 0901-1 were more depleted in all HSE contents than 0902-1, whereas the Os, Ir and Ru contents in 0902-1 were similar as the PUM (Figure 3.8). Sample 0904-1 had the depletions of all HSEs compared to the PUM, except for Pd. The harzburgites tended to have more scattered HSE patterns than plagioclase lherzolites and spinel lherzolites. The samples 09013 and 0902-10 kept relatively smooth HSE patterns compared to other harzburgites, especially 0901-2 which had the strongest depletions of Pd and Re, but not for Os, Ir and Ru. The most depleted Ir and Ru concentrations were observed in

samples 0902-3 and 0903-13.

The HSE patterns of plagioclase lherzolites from B-TLP seemed more scattered than those of P-MSPs (Figure 3.8). Sample HR-37, HR-70 and HR-90 of B-TLP showed more smooth HSE patterns and more enriched in Re than the other three samples of HR+0, HR-50 and HR-60. Moreover, HR-37, and HR-90 also had the depleted HSE patterns relative to the PUM. Sample HR-50 had the strongest depletions of Pt, Pd and Re, even compared to harzburgite HR+5.

Figure 3.9 shows the HSE and S abundances, Re/Os, Ru/Ir and  $^{187}\text{Os}/^{188}\text{Os}$  ratios of thin-layer peridotites from top to bottom in lithology diagrams. The Os, Ir, Ru, Pt and Pd mass fractions of plagioclase lherzolites both in T-TLP and B-TLP showed almost constant values, whereas, the Re, S mass fractions, and Re/Os, Ru/Ir ratios were more scattered in these samples. Harzburgite HR+5 had higher Os and Ru values, compared to plagioclase lherzolites from both T-TLPs and B-TLPs. Both MSPs and TLPs were relatively scattered distributed in diagrams of HSEs (Os, Ir, Ru, Pt, Pd) contents vs. Yb contents (Figure 3.10), whereas, the Re and Yb contents seemed to be positive correlations, ranging from harzburgites, spine-lherzolites to plagioclase lherzolites in MSPs. Moreover, TLPs seemed to have two different trends. The same feature was also observed in plots of HSE contents vs. S contents that Re and S contents showed very clear positive correlations in both MSPs and TLPs, but not for other HSEs (Figure 3.11).

### 5.3. Os isotope ratios

The  $^{187}\text{Os}/^{188}\text{Os}$  ratios of the massive lherzolites and harzburgites ranged from 0.1188 to 0.1316. The Re and Os mass fractions varied from 0.020 to 0.683 ng g<sup>-1</sup> and from 2.09 to 5.19 ng g<sup>-1</sup>, respectively (Table 3.1). The Re content varied by a factor of ~35, whereas the Os content varied by a factor of ~

2.5. The  $^{187}\text{Os}/^{188}\text{Os}$  ratios for the massive lherzolites and harzburgites (except for 0902-2) were lower than the Os isotopic composition of the PUM ( $^{187}\text{Os}/^{188}\text{Os} = 0.1296 \pm 0.008$ , Meisel et al. 2001). However, most plagioclase lherzolites had higher  $^{187}\text{Re}/^{188}\text{Os}$  ratios than that of the PUM ( $^{187}\text{Re}/^{188}\text{Os} = 0.4346$ , Meisel et al. 2001), and sample 0902-2 had the highest  $^{187}\text{Re}/^{188}\text{Os}$  ratio of  $0.13107 \pm 0.0007$  (Figure 3.12).

The fertility indicator  $\text{Al}_2\text{O}_3$  content normally showed good linear trends with the  $^{187}\text{Os}/^{188}\text{Os}$  ratios (Figure 3.13). All the MSPs ranging from harzburgites, spinel lherzolites to plagioclase lherzolites spanned almost the whole range from very depleted (i.e., low  $\text{Al}_2\text{O}_3$  contents and subchondritic  $^{187}\text{Os}/^{188}\text{Os}$  ratios) to fertile compositions ( $\text{Al}_2\text{O}_3 = \sim 3\text{-}4$  wt. %). Moreover, the  $\text{Al}_2\text{O}_3$  contents of the samples from 0904-1 series were systematically more depleted (i.e., more extensive melting) than other plagioclase lherzolites. The  $^{187}\text{Re}/^{188}\text{Os}$  ratios showed large variation between 0.037 and 1.534 in MSPs. In general, the enrichment and depletion of Re relative to other HSEs are interpreted to have been caused by the refertilisation and melt extraction processes, respectively. The higher enrichment of Re in 0902-2 was consistent with the enrichment of La/Ce, relative to sample 0902-2a (Figure 3.5) could be attributed to the refertilisation process caused by melt-rock interaction process. However, no obvious evidence for melt addition was observed in other P-MSP samples (e.g., Figure 3.10).

The  $^{187}\text{Os}/^{188}\text{Os}$  ratios of T-TLP and B-TLP ranged from 0.1202 to 0.1300. The Re and Os mass fractions varied from 0.044 to 0.621  $\text{ng g}^{-1}$  and 1.93 to 5.90  $\text{ng g}^{-1}$ , respectively (Table 3.1). The Re content varied by a factor of  $\sim 14$ , while the Os content varied by a factor of  $\sim 3$ . The  $^{187}\text{Os}/^{188}\text{Os}$  ratios of B-TLPs were lower than the PUM, except for one sample HR-70 ( $^{187}\text{Os}/^{188}\text{Os} = 0.12998$ ). And only HR-70 and HR-90 had higher  $^{187}\text{Re}/^{188}\text{Os}$  ratios than those of the PUM (Figure 3.12). Basically, the  $^{187}\text{Os}/^{188}\text{Os}$  ratios of B-TLP defined a positive correlation with  $\text{Al}_2\text{O}_3$  contents. Moreover, two samples

HR+0 (Al<sub>2</sub>O<sub>3</sub>=4.65 wt. %) and HR-70 (Al<sub>2</sub>O<sub>3</sub>=4.93 wt. %) had more fertile composition than that of the PUM (Al<sub>2</sub>O<sub>3</sub>= ~ 4.27 wt. %) (Figure 3.13). The positive correlations between <sup>187</sup>Os/<sup>188</sup>Os ratios and Al<sub>2</sub>O<sub>3</sub> contents in both MSP and TLP indicate that variable <sup>187</sup>Os/<sup>188</sup>Os ratios could be basically attributed to the fertility.

## 6. Discussion

### 6.1. Evaluation of Re-Os model ages

Both mantle model ages (T<sub>MA</sub>) and Re depletion model ages (T<sub>RD</sub>) may provide estimates for the minimum age of melt extractions in ancient peridotites. The assumption with T<sub>MA</sub> is that <sup>187</sup>Re/<sup>188</sup>Os ratio measured in the sample is an accurate reflection of its long-term history and has not been affected by later processes.

$$T_{MA} = 1/\lambda \times \ln\left\{\left(\frac{{}^{187}\text{Os}/{}^{188}\text{Os}_{PUM} - {}^{187}\text{Os}/{}^{188}\text{Os}_{sample}}{{}^{187}\text{Re}/{}^{188}\text{Os}_{PUM} - {}^{187}\text{Re}/{}^{188}\text{Os}_{sample}}\right) + 1\right\}$$

By contrast, the T<sub>RD</sub> does not rely on the <sup>187</sup>Re/<sup>188</sup>Os ratio measured in the sample, which can be affected by recent Re addition. This method used for depleted peridotite/xenolith by assuming that the original Re in the peridotite was removed during melt-extraction; and the Re was added later to the sample from the host melt. In reality, this model provides a minimum age for samples that have experienced melt-depletion, if no secondary process was occurred:

$$T_{RD} = 1/\lambda \times \ln\left\{\left(\frac{{}^{187}\text{Os}/{}^{188}\text{Os}_{PUM} - {}^{187}\text{Os}/{}^{188}\text{Os}_{sample}}{{}^{187}\text{Re}/{}^{188}\text{Os}_{PUM}}\right) + 1\right\}$$

The hypothesis of melt extraction can somehow reflect the formation of the lithospheric mantle with the interpretation of T<sub>MA</sub>. However, if the variations of moderately incompatible lithophile elements (such as Al, Na) in peridotites is controlled by melt-rock interaction (i.e., the addition of incompatible elements from the reacting melt into the peridotite, this could also affect the Re-Os isotope system,

leading to improper interpretations of  $T_{MA}$  as well as the abundances of HSEs in peridotites. Most P-MSPs showed higher  $^{187}\text{Re}/^{188}\text{Os}$  ratios than the 4.56 Ga reference line for PUM (Figure 3.12), indicating that the Re-Os isotope system in these samples were modified by later Re addition or Os subtraction processes after the melt extraction.

Both  $T_{MA}$  and  $T_{RD}$  ages of ES-MSPs displayed relatively large variations, ranging from 0.5-2.5 Ga. Yoshikawa and Nakamura (2000) concluded that melt extraction occurred at ~850 Ma, using Sm-Nd isotope system. Also, Malaviarachchi et al. (2008) reported Sm-Nd and Lu-Hf isochron ages of ~ 1Ga as the partial melting age. Although both  $T_{MA}$  and  $T_{RD}$  ages were not inconsistent with the previous age data, the significantly large variation among the determined ages reveals that Re-Os isotope system in the analysed samples were not only controlled by melt-extraction. Only two harzburgite (0901-2 and 0903-13) and one B-TLP (HR-50) which had extremely low  $^{187}\text{Re}/^{188}\text{Os}$  ratios (<0.07) may indicate the minimum age of melt extraction age at 1.2 -1.4 Ga.

## **6.2. HSE abundances and fertility**

Generally, the systematic depletions of Re, S,  $\text{Al}_2\text{O}_3$ , and Yb concentrations in harzburgites and S-MSPs relative to P-MSPs and TLPs indicate that they may have experienced higher degrees of melt extraction during partial melting (Figure 3.6, 3.10 and 3.11).

The Yb contents are positively correlated with  $\text{Al}_2\text{O}_3$  contents (Figure 3.6), thus, Yb also represents the fertility in peridotites during melting process. If the initial compositions of P-MSP prior to melt extraction was assumed within the range of PUM, the Os, Ir, Ru, and Pt abundances of P-MSPs would not change significantly from PUM composition with the decreasing of Yb contents (e.g., Becker and Dale 2016). As shown in PUM-normalised patterns (Figure 3.8), Ir and Pt in P-MSPs did not deviated

significantly from the PUM, thus, they also did not show systematic trend against Yb contents (Figure 3.10). However, almost all ES-MSP samples, one from 0902-8 series (0902-8a), three from 0904-1 series (0904-1, b, and c), and one from T-TLP (HR+20) showed constantly lower values than the PUM.

The negative anomalies of Os and Ru are expressed by plotting Os/Ir and Ru/Ir ratios against Yb contents (Figure 3.14a and b). No correlation could be found in both figures, however, when data of DP-MSP and EP-MSP are individually observed, Ru/Ir ratios of both groups showed positive correlations, and the trends of DP- and EP-MSP aligned in parallel. The plot of Os/Ir vs. Yb also showed similar patterns except for one sample from 0902-8 series (0908-2a). If the melt extraction process controls Yb abundances, Os/Ir, and Ru/Ir ratios of the residual peridotites should not change against Yb under the low-degree of melting, or negatively and positively correlated with Yb, respectively, under the relatively high degree of melting. Thus, the depletions of Os and Ru relative to Ir could not be solely attributed to the melt extraction process, and additional process has to be considered for the fractionation of Os/Ir and Ru/Ir ratios in P-MSPs.

During melting in the mantle, the variation of Re/Os ratio in peridotites should be basically controlled by the degrees of Re depletion. Saal et al. (2001) also argued that the Re-Os isotope system of Horoman peridotites was mainly controlled by variable Re additions. However, the systematic depletions of Os for all DP-MSPs and some of the EP-MSPs indicate that variations of Re/Os ratio could also be controlled by the depletion of Os. When the Re/Os ratio was plotted against Re contents, two distinct trends were observed (Figure 3.15a). These trends could not be seen in plot of Re/Ir vs. Re (Figure 3.15d), suggesting that these trends were controlled by Os concentrations. The plots of Re/Os vs. Os and Re vs. Os also supported this idea (Figure 3.15b and c). Thus, the P-MSPs were classified as low-Os and high-Os types (Figure 3.15). In the plot of  $^{187}\text{Re}/^{188}\text{Os}$  vs.  $^{187}\text{Os}/^{188}\text{Os}$  ratios,

samples forming these two trends showed clear differences (Figure 3.16). The high-Os type of P-MSPs were plotted left of the 4.56 Ga reference line for PUM in Figure 3.16. On the other hand, most low-Os type of P-MSP samples were plotted right of the 4.56 reference line. Therefore, Os subtraction from P-MSPs basically controlled the higher values of  $^{187}\text{Re}/^{188}\text{Os}$  ratios in the Re-Os isotope system, although the possibility of melt addition cannot be denied in some samples (e.g., 0902-2).

The trace element compositions and O-Sr-Nd-Hf-Pb isotopic compositions revealed that melt-peridotite reactions apparently occurred in B-TLPs (Figure 3.4), which have interacted with melts related to thin-layer gabbros at  $\sim 300$  Ga (Malaviarachchi et al., 2010). The variable patterns of HSEs relative to PUM may suggest multiple melt-rock reaction process in B-TLPs (Figure 3.8). Therefore, the B-TLPs were further classified into three types based on HSE abundances and Re-Os isotope system (Figure 3.21). The first type (samples HR+5 and HR+50) with the most depletion of Pt, Pd and Re basically only underwent melt extraction; the second type (samples HR-37, HR-90 and HR-70) may undergo melt-rock reaction by addition of Re and Pd, leading to higher  $^{187}\text{Re}/^{188}\text{Os}$  ratios. The third type (samples HR-37 and HR+0) was reacted with S-saturated melt. The Pt and Pd were dissolved and precipitated again in sulfide, but less Re was added than the second type, leading to lower  $^{187}\text{Re}/^{188}\text{Os}$  ratios.

### **6.3. Phase control for Os and Ru fractionations**

It is somehow difficult to explain Os and Ru depletions (but not for Ir) using melt extraction and/or melt addition processes as seen in the PUM-normalised patterns (Figure 3.8), hence, it is necessary to consider additional processes to explain the fractionations of Os/Ir and Ru/Ir ratios. HSEs are mainly distributed in sulfide or alloy in the peridotite, which can be dissolved by inverse aqua regia (see in Chapter 2). The pentlandite is the main sulfide phase observed in MSPs, and is mostly anhedral in

shape and distributed as filling the grain boundaries of the constituent minerals. Thus, sulfides in MSPs were interpreted as secondary products caused by fluid or melt interaction processes (Ranaweena et al., 2018).

The Os, Ir, and Ru (IPGE group) showed compatible behavior in olivine and chromite relative to the coexisting melts (Puchtel and Humayun, 2001) during melt extraction. However, it is considered that the apparent compatibilities of IPGE in olivine and chromite is controlled by the presence of microinclusions of platinum group element minerals (PGM), such as IPGE-bearing alloy laurite ( $\text{RuS}_2$ )-erlichmanite ( $\text{OsS}_2$ ) (e.g., Brenan et al. 2016). Thus, the depletions of Ru and Os relative to Ir for low-Os type from P-MSPs could be possibly caused by the dissolution of  $\text{RuS}_2$ - $\text{OsS}_2$  phases during metamorphic or alteration processes.

#### **6.4. Effect of fluid-rock interaction**

As explained previously, the MSPs could have been experienced by several fluid-rock interaction processes after the melt extraction at MOR setting (Ranaweera et al., 2018). Thus, the timing of dissolution and extraction of  $\text{RuS}_2$ - $\text{OsS}_2$  phases in the Horoman peridotites will be examined.

##### **6.4.1. Recent serpentinisation process**

During hydrothermal serpentinisation process, most HSEs (Ru, Ir, Os, Rh, Au) are typically rarely fluid-mobile. The modal abundance of serpentine is positively correlated with bulk  $\text{H}_2\text{O}$  contents (Figure 3.17). Among P-MSPs, the 0908-8 series contained extremely high abundances of serpentines (17-20 vol. %) and  $\text{H}_2\text{O}$  contents (2.67-2.77 wt.%) relative to other plagioclase lherzolites (serpentine < 2.3 vol.% and  $\text{H}_2\text{O}$  < 0.61 wt.%). However, there was no systematic trend of Ru/Ir and Os/Ir ratios against  $\text{H}_2\text{O}$  content for all P-MSPs (Figure 3.17). Also, there was no systematic relationship between

H<sub>2</sub>O content against Ru/Ir and Os/Ir ratios for spinel lherzolites and harzburgites (Figure 3.17). Hence, it is inferred that the fractionations of HSEs were least affected by the latest serpentinisation process, which could be occurred during exhumation or after the exposure.

#### **6.4.2. SSH alteration at MOR after melt extraction**

The Pb isotopic compositions of the massive peridotites exhibit a large variation (Figure 3.20). The P-MSPs had unradiogenic Pb isotope ratios, whereas the S-MSPs had more enriched and radiogenic Pb isotopic compositions. Malaviarachchi et al. (2008) pointed out that the plagioclase lherzolites with the highly unradiogenic Pb isotope ratios relative to any known peridotites may solely undergo the process of melt extraction (no sign of melt-rock reactions) at the MOR. These samples preserved the least radiogenic Pb component without convective stirring and homogenisation in the Earth's mantle for at least ~1Ga, which might help to solve the Earth's Pb paradox. The SSH alteration was occurred at the MOR following melt extraction, which could lead to the enrichment of fluid-mobile elements and Li isotopic compositions (Ranaweena et al. 2018). If the Os loss was occurred during SSH alteration without involving Re and/or Os from hydrothermal fluid, the Re-Os isotopic compositions should follow the ~1Ga isochron. However, the analysed isotope data did not support this evidence. Even Os loss was occurred at MOR, the later process may have erased the evidence.

#### **6.4.3. Fluid-rock reaction in the mantle wedge**

Because of the high diffusivity of hydrogen in the constituent minerals at the upper mantle temperature, the H<sub>2</sub>O content in peridotites could have been modified after fluid-rock interaction process occurred in the mantle wedge. However, the fluid-related processes in P-MSPs have been identified by the isotopic compositions of fluid-mobile elements (i.e., <sup>7</sup>Li/<sup>6</sup>Li and <sup>87</sup>Rb-<sup>87</sup>Sr isotope systems) (Ranaweena et al., 2018). The variations of  $\delta^7\text{Li}_{\text{LSEVC}}$  values (hereafter expressed as  $\delta^7\text{Li}$ ) of P-MSPs

showed large ranges between +4 and -1 ‰, while those of TLPs showed relatively narrow ranges between +5 and +6‰, which was identical with DMM composition. The systematic lower  $\delta^7\text{Li}$  values in EP-MSP relative to DP-MSP were explained by the isotopic fractionation during SSH alteration, followed by dehydration in the recycling of the mantle. The  $^{87}\text{Rb}$ - $^{87}\text{Sr}$  isotope system of P-MSPs revealed more obvious differences between DP-MSP and EP-MSP. The Sr isotopic compositions of DP-MSP were more depleted than those of DMM, while those of EP-MSP were more enriched than DMM, defining an age of  $154 \pm 38$  Ma with the initial  $^{87}\text{Sr}/^{86}\text{Sr}$  ratio of  $0.70224 \pm 0.00004$ . The Sr isotopic composition revealed that the source of EP-MSPs was interacted with the slab-derived fluid in the mantle wedge at circa 150 Ma. On the other hand, the initial  $^{87}\text{Sr}/^{86}\text{Sr}$  ratio of DP-MSP at 150 Ma was much lower than the MORB-like mantle composition, indicating that no isotope modification was occurred in DP-MSPs. The EP-MSP tended to have higher Os mass fractions relative to DP-MSP. Among EP-MSPs, the 0902-8 series with higher Rb/Sr ratio showed relatively higher Ru/Ir and Os/Ir ratio than those of 0904-1 series. Assume that Ru and Os were added by the fluid-rock interaction process, hence, in this case, the extremely high fluid-rock ratio is a prerequisite, as HSE abundances in the fluid are presumably much lower than in the peridotites. Assume that the fluid-rock ratio is high enough, and fluid is derived from the subduction slab, however, it is difficult to explain the depleted Sr and Pb isotopic compositions in EP-MSPs. Therefore, we propose a new Os subtraction model. The possible explanation for the Os depletion in P-MSPs is probably caused by the dissolution of Ru-Os sulfides without modifying the Rb-Sr and U-Th-Pb isotope systems. The sulfide  $(\text{Ru-Os})\text{S}_2$  in low-Os type may undergo an unknown dissolution process, however, the mechanism of the dissolution process still remains unclear.

#### **6.5. Re-Os model ages for two-step fractionation processes**

As the low-Os type samples had higher  $^{187}\text{Re}/^{188}\text{Os}$  and lower  $^{187}\text{Os}/^{188}\text{Os}$  ratios relative to the PUM,

it is impossible to explain their genesis by single melt-extraction process. As mentioned above, the Horoman peridotites have experienced melt-rock interaction and/or probably hydrothermal alteration processes at ~300 Ma and ~150 Ma, respectively, following melt extraction. Hence, the Re-Os fractionation could be occurred during these periods. The Re-Os model ages using two-steps fractionation processes were calculated as follows (Figure. 3.19): (1) The age of melt-extraction was estimated at ~1.4 Ga, using  $T_{RD}$  ages of harzburgites which had the minimum  $^{187}\text{Re}/^{188}\text{Os}$  and  $^{187}\text{Os}/^{188}\text{Os}$  ratios. (2) The melt-extracted mantle compositions at 0.3 Ga and 0.15 Ga were calculated, which are shown in red line in Figure 3.19a and b, respectively. (3) Re-Os fractionation caused by Os loss was assumed at 0.3 Ga and 0.15 Ga, respectively, giving variable  $^{187}\text{Re}/^{188}\text{Os}$  ratios (i.e., 0.08 to 0.40). (4) The isotope reference lines of 0.3 Ga and 0.15 Ga at given  $^{187}\text{Re}/^{188}\text{Os}$  ratios were calculated. Both model age calculations did not show the significant differences, indicating that it is difficult to identify the ages of the secondary Re-Os fractionations correctly. Nevertheless, the Re-Os isotopic variations in most P-MSPs could be possibly explained by the secondary Os subtraction process. Assume the Os subtraction process was occurred at ~150Ma, the scenario may include two steps. The sulfide (Ru-Os)<sub>2</sub> was first dissolved in low-Os type during a given metamorphic or alteration process in the mantle wedge, and then the slab-derived fluid washed Os and Ru away out of the minerals.

#### **6.6. Melt/fluid-rock reaction of one sample dunite**

Among all Horoman peridotite samples, however, dunite presented different behavior of HSE abundances and Os isotopic compositions compared to lherzolites and harzburgites (Figure 3.8 and 3.12). The reason remains obscure. As the dunites are commonly interpreted as olivine rich rocks reacted with the basaltic-melts in the former melt channels (e.g., Kelemen, 1990), hence, the enrichment of Pd, Pt and Re concentrations compared to the PUM, and also much higher  $^{187}\text{Re}/^{188}\text{Os}$  (1.096) ratios than PUM ( $^{187}\text{Re}/^{188}\text{Os} = 0.4346$ ) observed in our study may be ascribed to the process

of the melt-peridotite reaction, however, the age of melt-rock reactions and the possible melt source are still unclear. On the other hand, it is also possible that the highly radiogenic  $^{187}\text{Os}/^{188}\text{Os}$  ratio (0.14493) in dunite compared to the PUM ( $^{187}\text{Os}/^{188}\text{Os} = 0.1296$ ) was added through the fluid transport (e.g., Brandon et al. 1996), which might be derived from the sediments at the subduction zone at younger age.

## 7. Conclusions

In this study, we determined HSE abundances and  $^{187}\text{Os}/^{188}\text{Os}$  ratios of a suite of Horoman peridotite samples, ranging from fertile plagioclase lherzolites through refractory spinel lherzolites, highly depleted spinel harzburgites to subordinated dunite. Generally, the positive correlations between Re and S,  $\text{Al}_2\text{O}_3$ , and Yb concentrations, ranging from harzburgites, spinel lherzolites to plagioclase lherzolites, indicate that harzburgites and spinel lherzolites may have experienced higher degrees of melt extraction during partial melting. The melt extraction may have occurred at  $\sim 1.4$  Ga using the most depleted harzburgite samples based on Re depletion model ages.

Moreover, it is also observed that the most massive plagioclase lherzolite samples showed depleted Os and Ru patterns relative to the PUM, and higher  $^{187}\text{Re}/^{188}\text{Os}$  ratios than the 4.56 Ga reference line for PUM in Re-Os isochron diagram, which could not simply explained by melt extraction. Hence, the massive plagioclase lherzolites samples were classified as low-Os and high-Os types from this study. The Os subtraction process occurred in low-Os type of massive plagioclase lherzolites (i.e., their  $^{187}\text{Re}/^{188}\text{Os}$  ratios were plotted in the right of the 4.56 Ga reference line) basically controlled the higher  $^{187}\text{Re}/^{188}\text{Os}$  ratios. Moreover, the higher enrichment of Re in 0902-2 was consistent with the enrichment of La/Ce, relative to sample 0902-2a, which might be also possibly attributed to the refertilisation caused by melt-rock interaction process. Nevertheless, the Os subtraction is likely to be

a predominant secondary process following melt extraction in most massive plagioclase lherzolites. The depletions of Ru and Os in low-Os type of massive plagioclase lherzolites could be caused by the dissolution of platinum group element minerals such as  $\text{RuS}_2$ - $\text{OsS}_2$  phases during metamorphic or alteration processes. However, the timing and mechanism of Os subtraction remain still unclear. As sulfides/alloys are the host minerals for HSEs in peridotites, in-situ analysis of HSEs in sulfide/alloy may help to reveal more detailed information about HSE behavior during secondary process. On the other hand, the bottom thin-layer peridotites preserved successive melt extraction, melt-rock interaction, sulfide precipitation processes that could not be decoded by lithophile elements geochemistry. The thin-layer peridotites were classified into three types based on HSE abundances and Re-Os isotope system. The first type with the most depletion of Pt, Pd and Re only underwent melt extraction; the second type experienced melt-rock reaction by addition of Re and Pd, leading to higher  $^{187}\text{Re}/^{188}\text{Os}$  ratios. The third type was reacted with S-saturated melt. The Pt and Pd were dissolved and precipitated again in sulfide, but less Re was added, leading to lower  $^{187}\text{Re}/^{188}\text{Os}$  ratios.

Dunite presented different behavior of HSE abundances and Os isotopic compositions among all the massive peridotite samples. The enrichment of Pd, Pt and Re concentrations compared to PUM, and higher  $^{187}\text{Re}/^{188}\text{Os}$  ratios than PUM may be attributed to the process of the basaltic-melt addition to the peridotites. Also, the fluid alteration could be one of the explanations for the highly radiogenic  $^{187}\text{Os}/^{188}\text{Os}$  ratios observed in dunite, which may have occurred at the subduction zone at younger age.

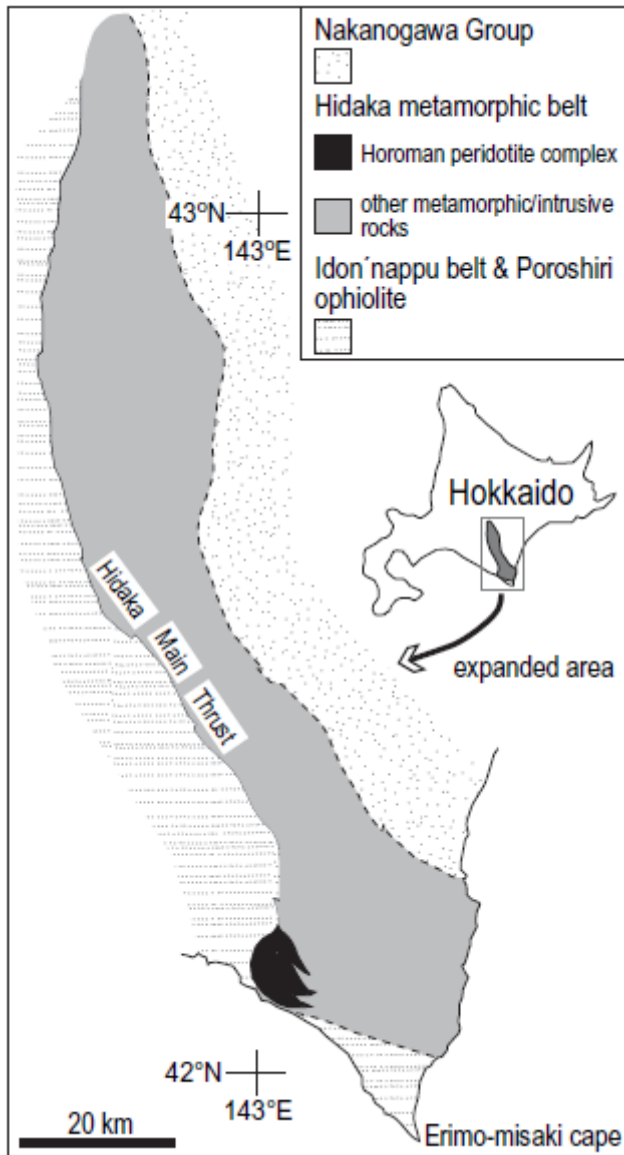


Figure 3.1. Map of regional setting of the Hidaka metamorphic belt and location of the Horoman peridotite massif (Yamamoto et al. 2010).

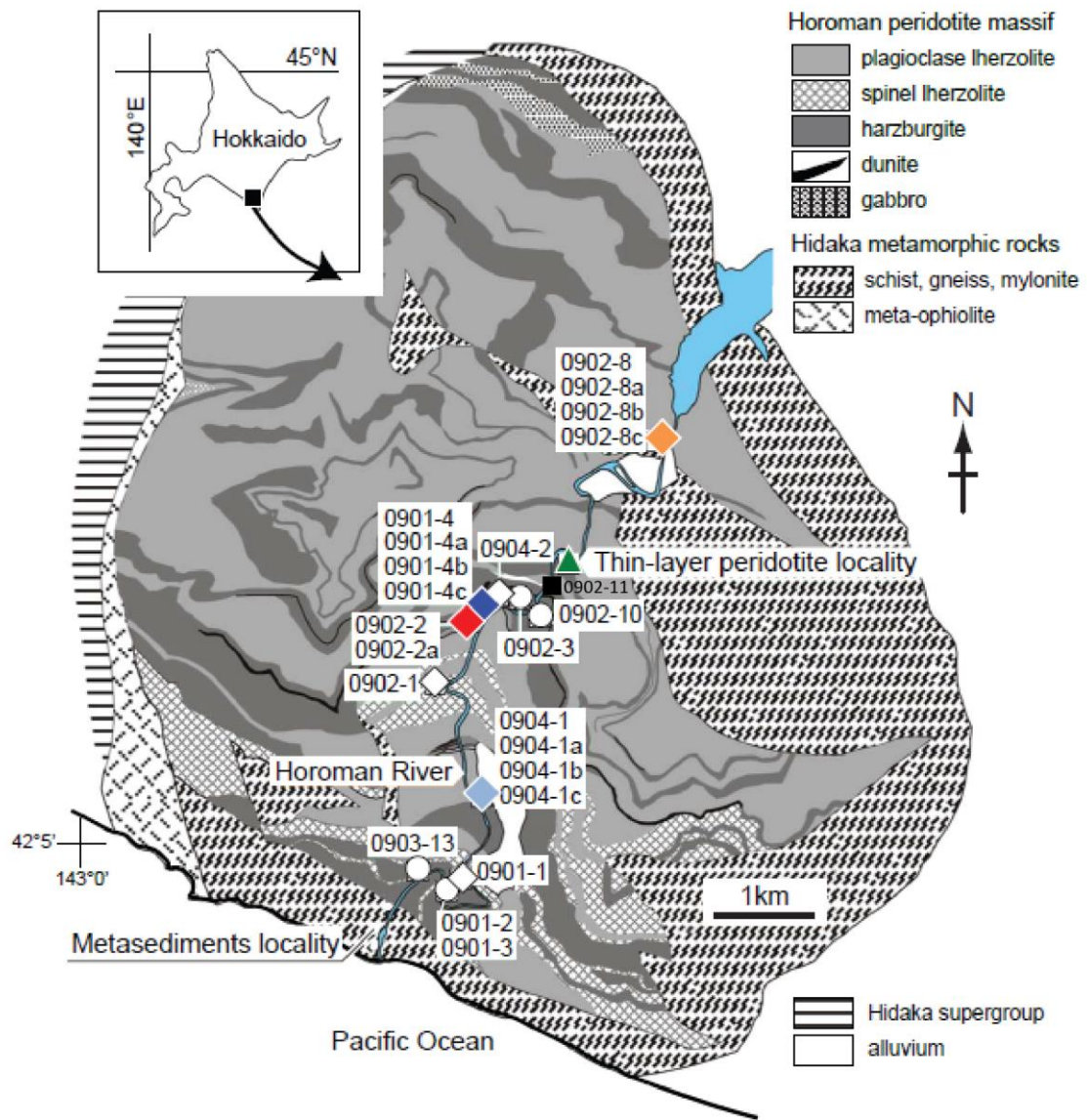


Figure 3.2. Lithologic map of the Horoman peridotite massif. The map is modified after Ranaweera et al. (2018).

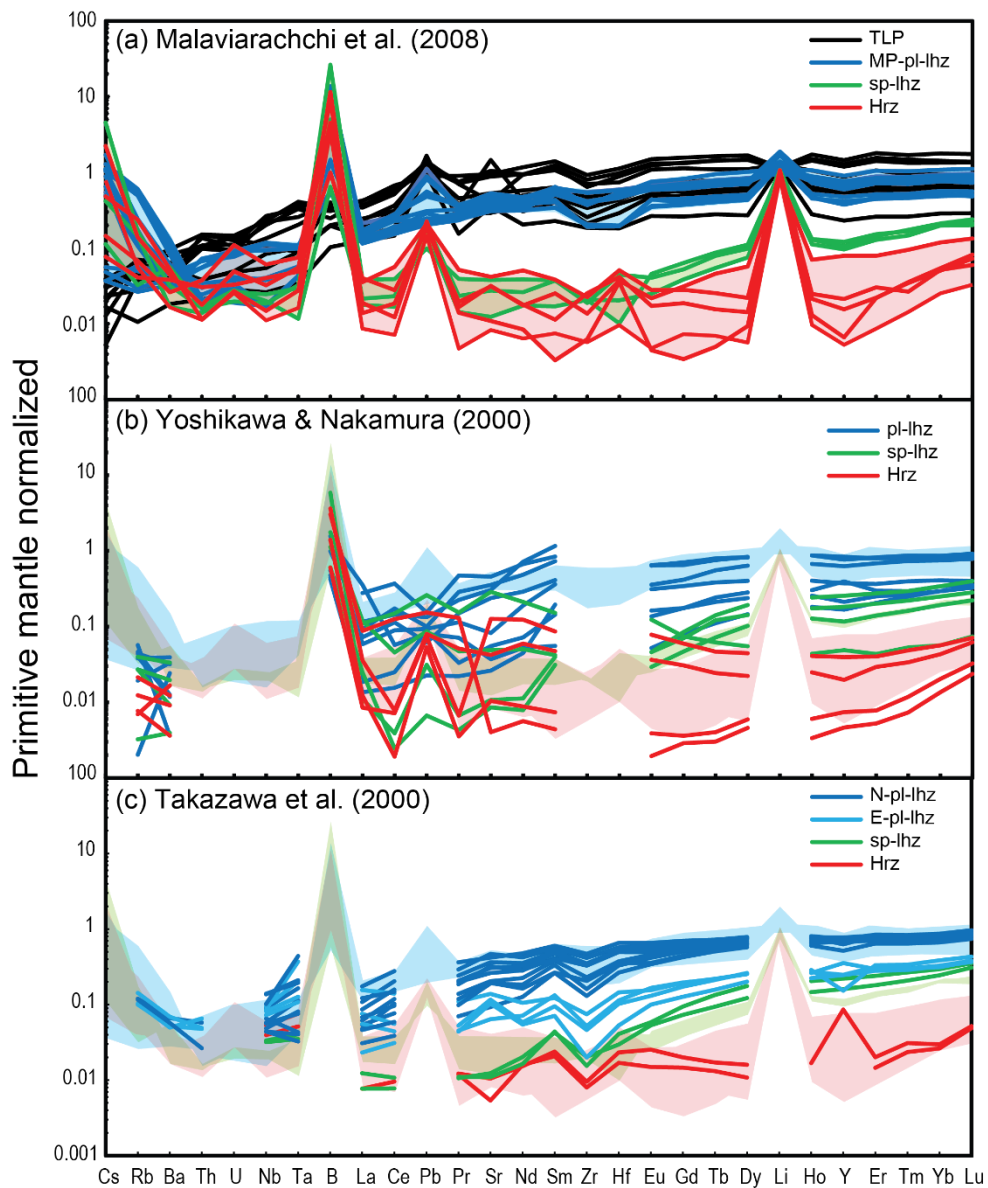


Figure 3.3. Primitive mantle normalised REE patterns from previous literatures. Primitive mantle data: McDonough and Sun (1995).

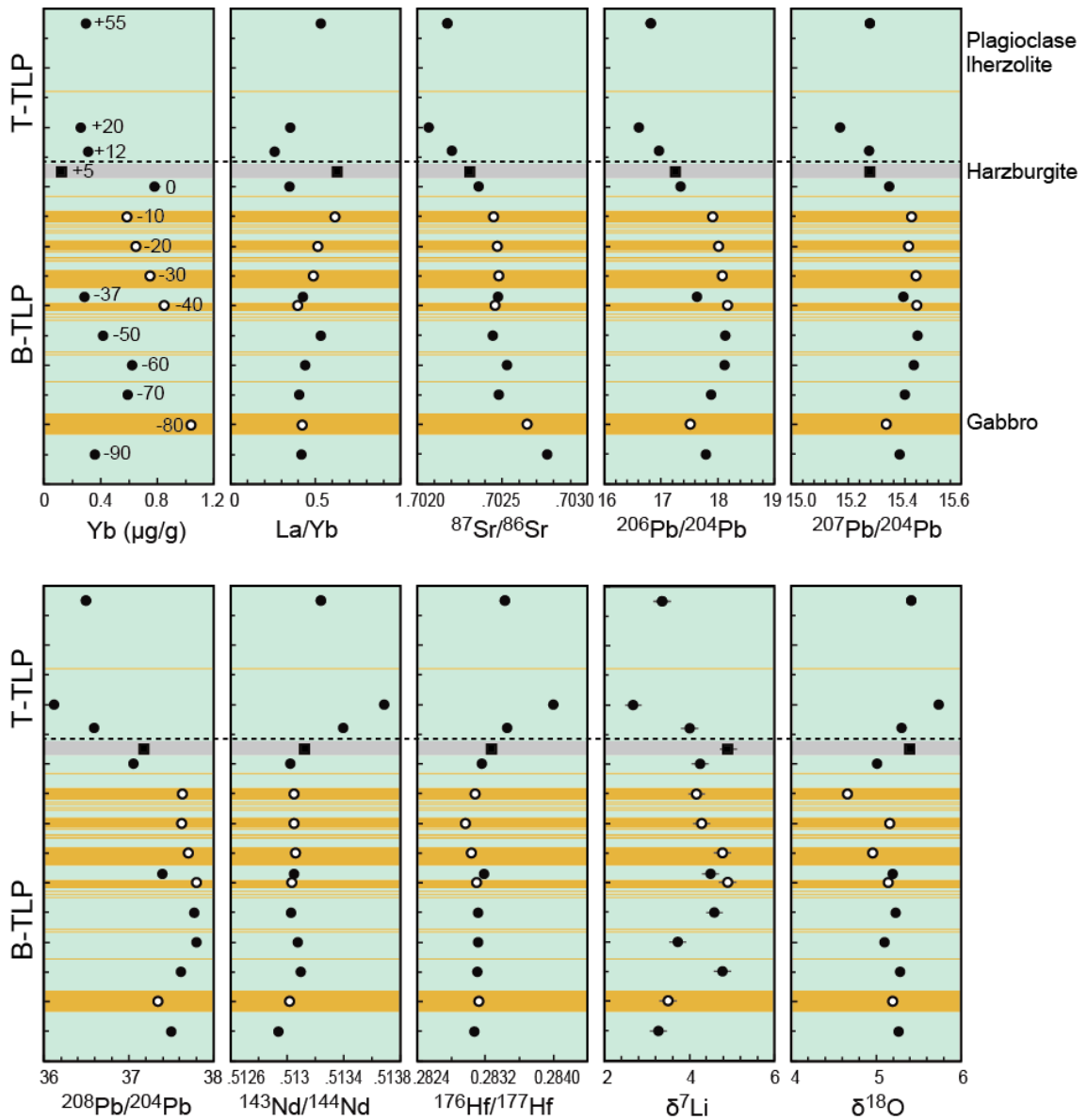


Figure 3.4. Lithological variation of trace elements and isotopic data for TLP. The thickness from bottom to top is 1.95m. The broken line is boundary of T-TLP and B-TLP classified in this study. Data are from Malaviarachchi et al. (2008, 2010) and Ranaweera et al. (2018). Black circle: plagioclase lherzolite; black square: harzburgite; open circle: gabbro.

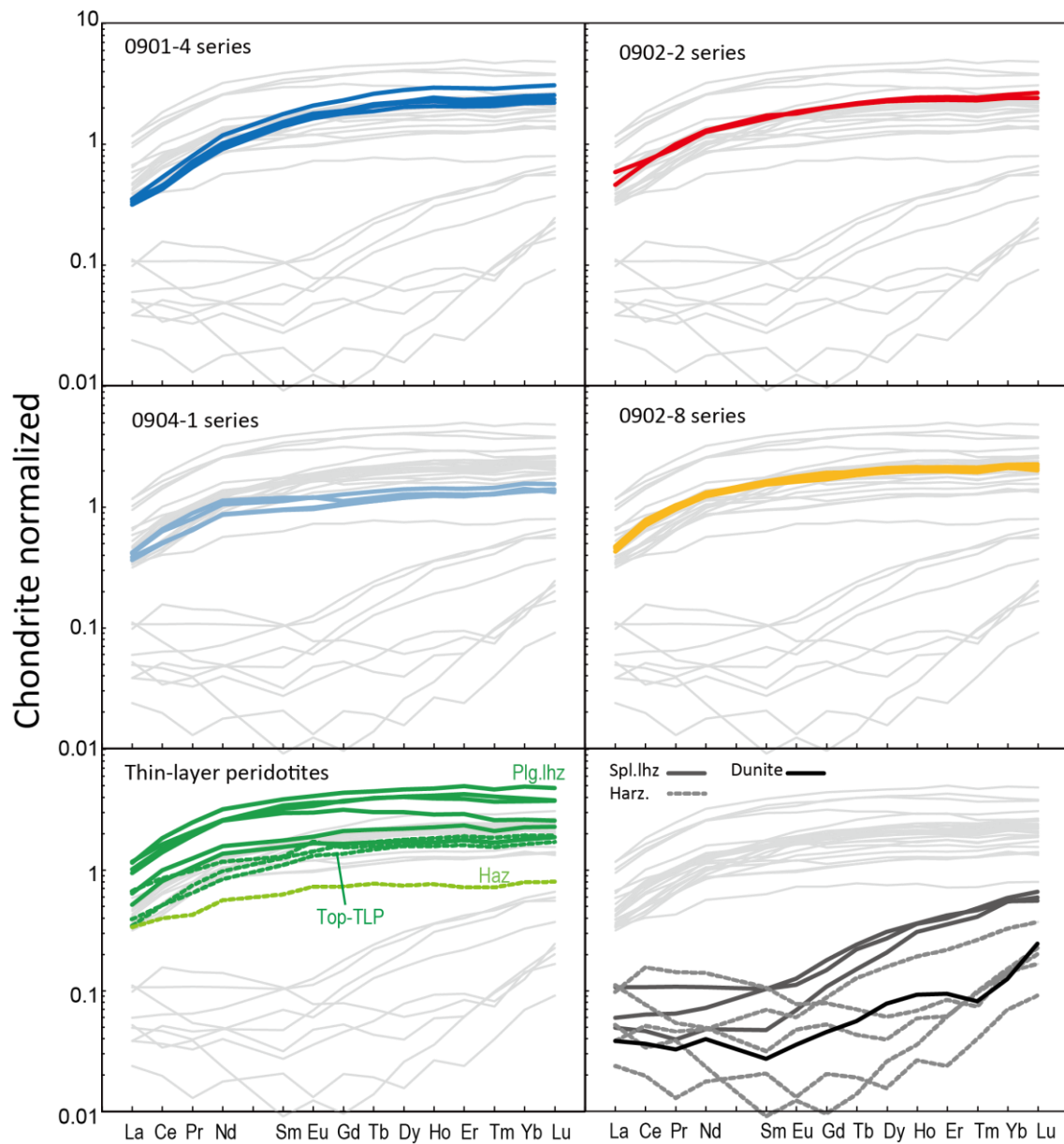


Figure 3.5. CI chondrite normalised REE patterns of Horoman peridotite samples. CI chondrite data: McDonough and Sun (1995). Data are from Malavirachchi et al. (2008) and unpublished data for dunite.

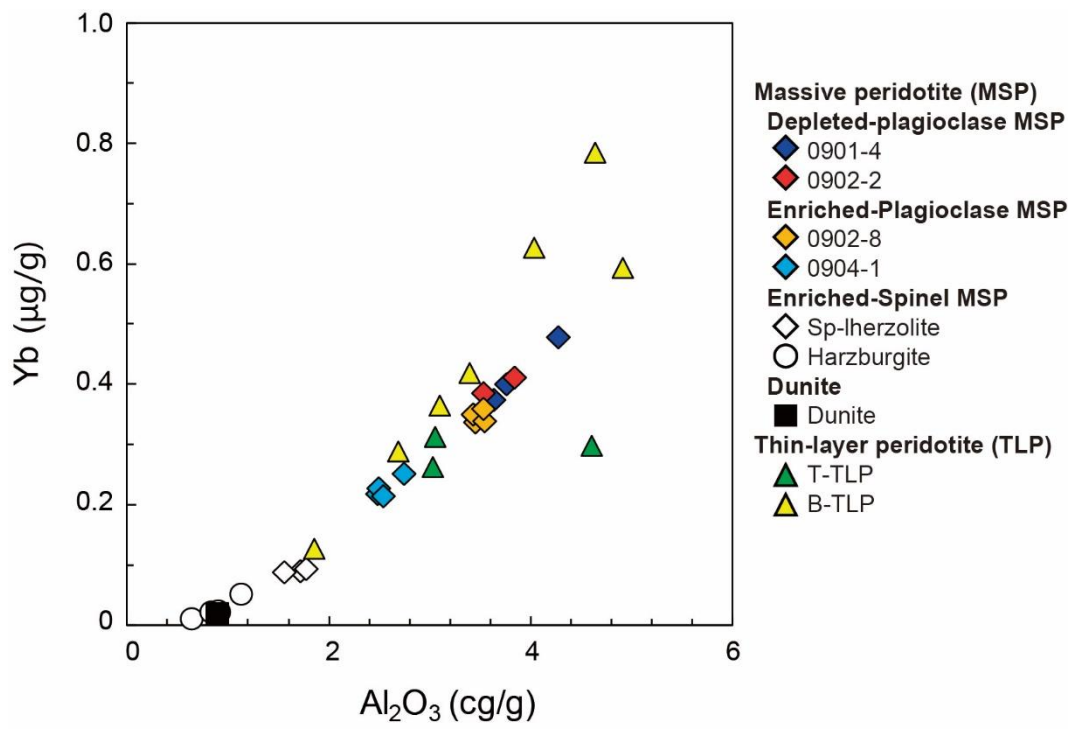


Figure 3.6. Plot of Yb vs. Al<sub>2</sub>O<sub>3</sub> in Horoman peridotite samples.

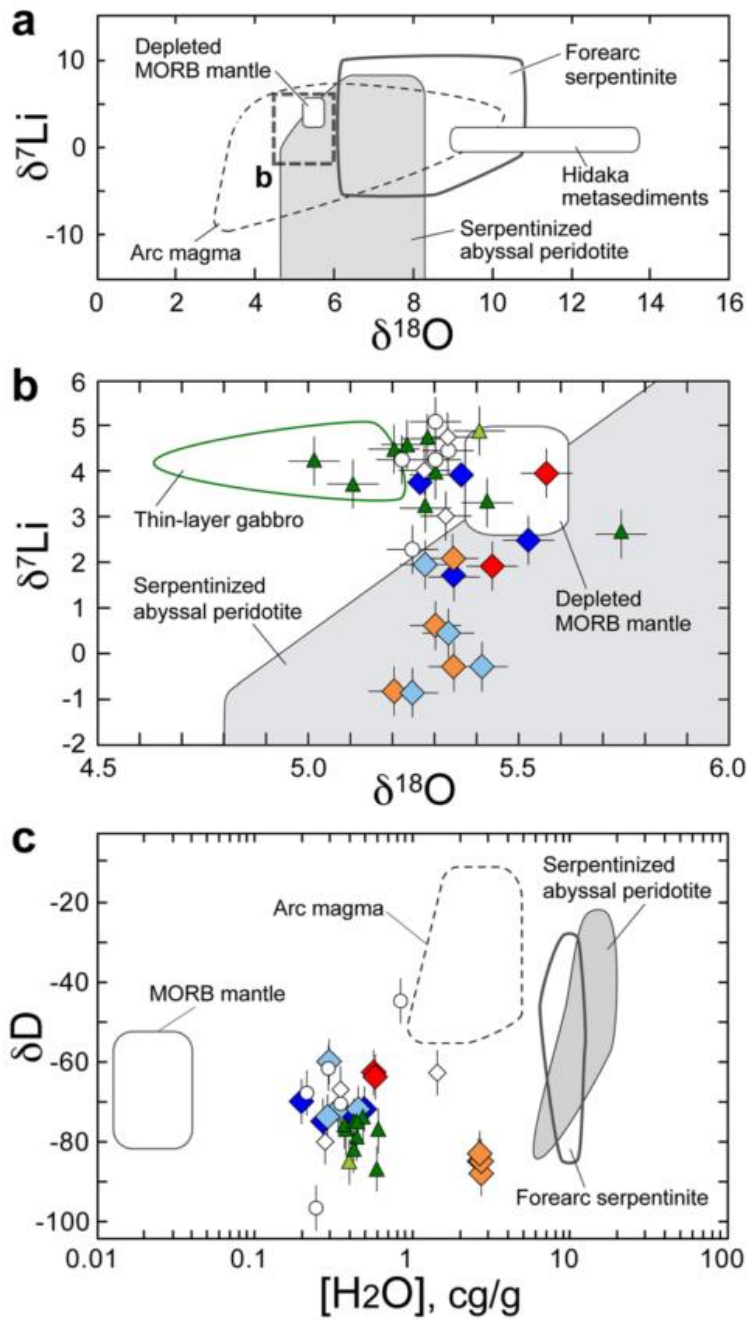


Figure 3.7. Oxygen, Li and H isotopic compositions, and H<sub>2</sub>O concentrations of the Horoman peridotite samples (Ranaweera et al. 2018). Symbols are the same as in Figure 3.6. (a) Oxygen and Li isotope compositions. The range of the plot displayed in (b) is shown by the dashed line. (b) Oxygen and Li isotope compositions of the Horoman samples. (c) Hydrogen isotope compositions and H<sub>2</sub>O concentrations of the Horoman peridotites.

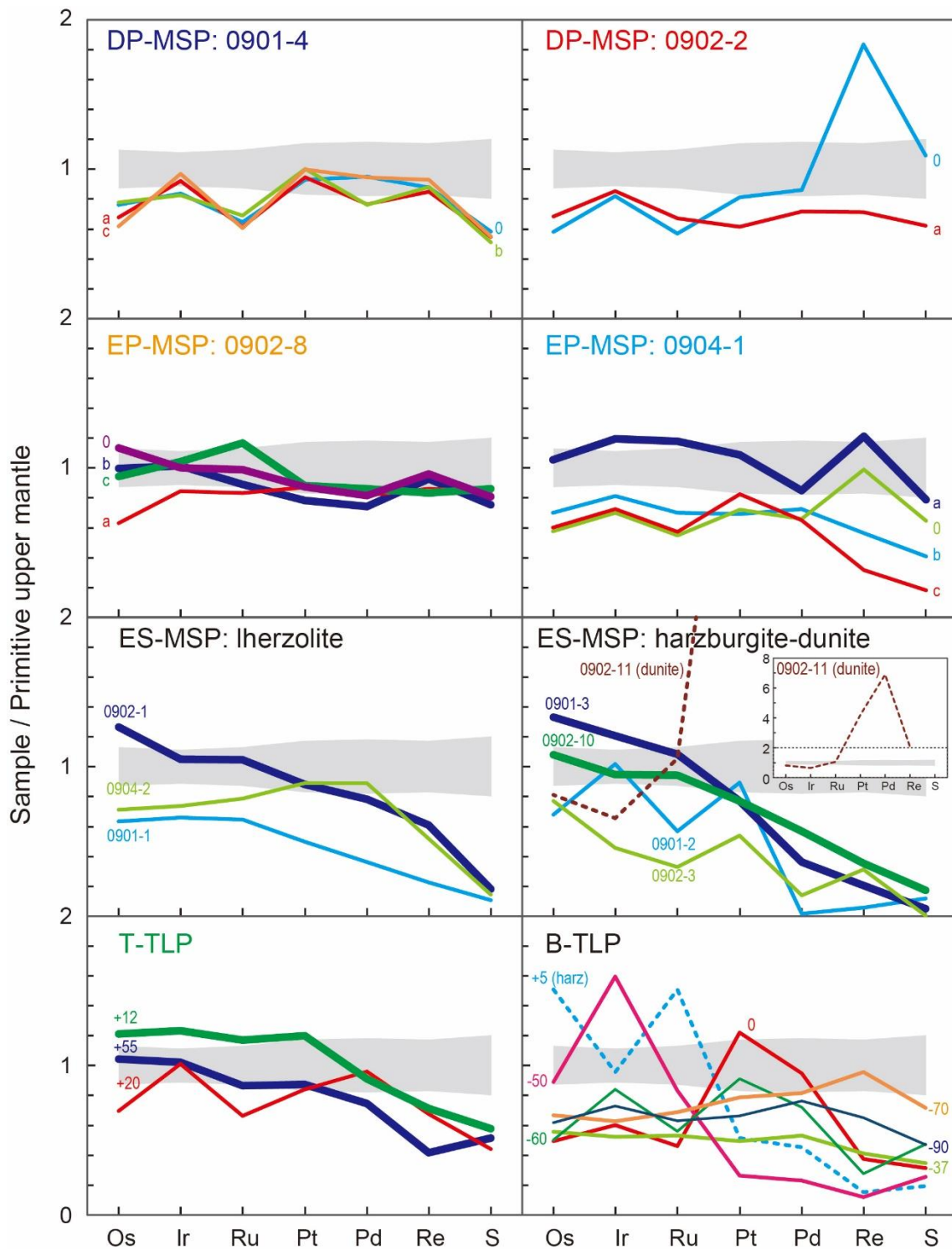


Figure 3.8. Primitive upper mantle normalised patterns of Horoman peridotite samples. PUM data: Becker et al. (2006) for HSEs and McDonough and Sun (1995) for S (primitive mantle composition). Grey region: 1 $\sigma$  range of the estimated primitive upper mantle.

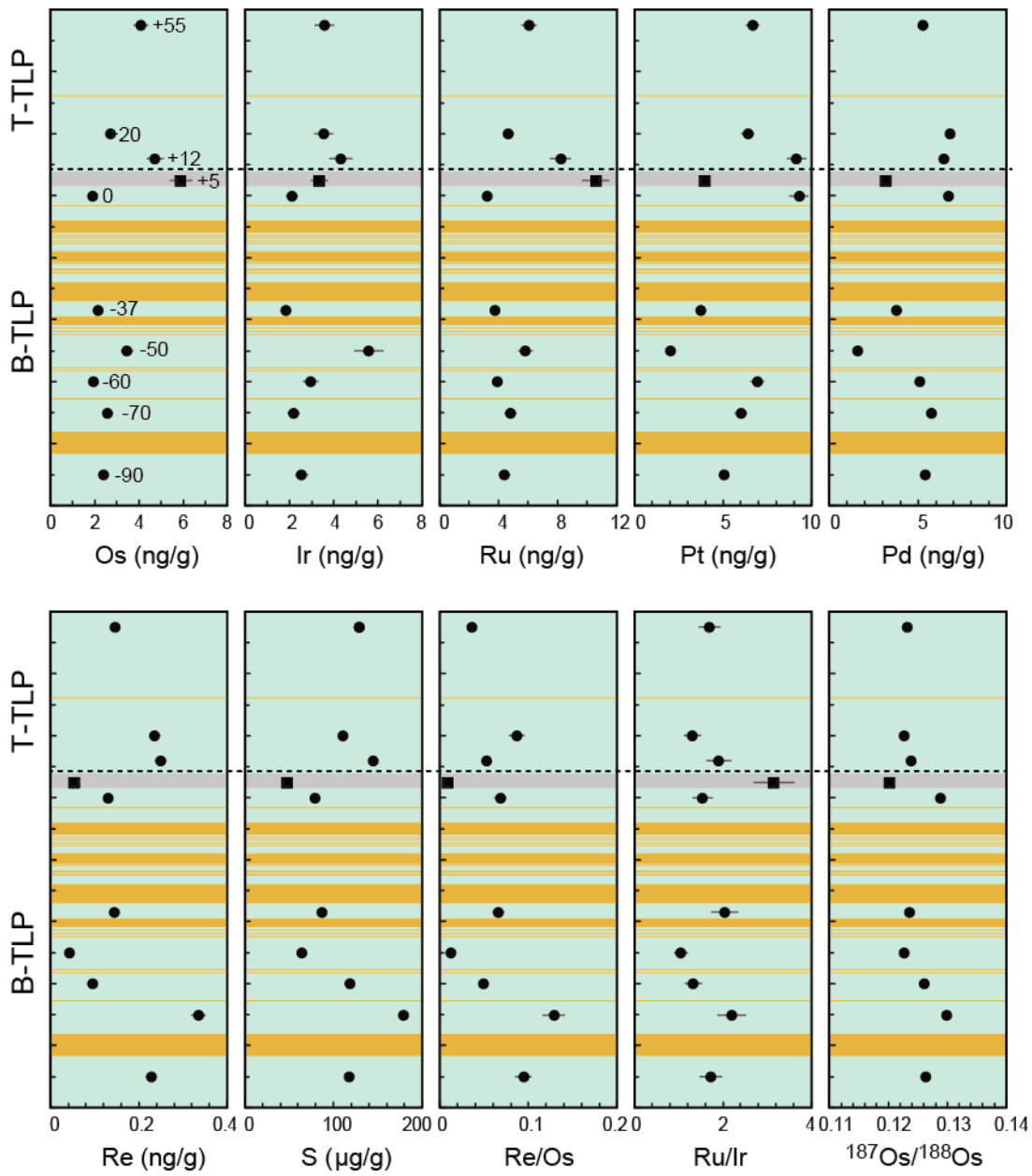


Figure 3.9. Lithology diagram of the HSE and S abundances, Re/Os, Ru/Ir and  $^{187}\text{Os}/^{188}\text{Os}$  ratios of thin-layer peridotites from top to bottom.

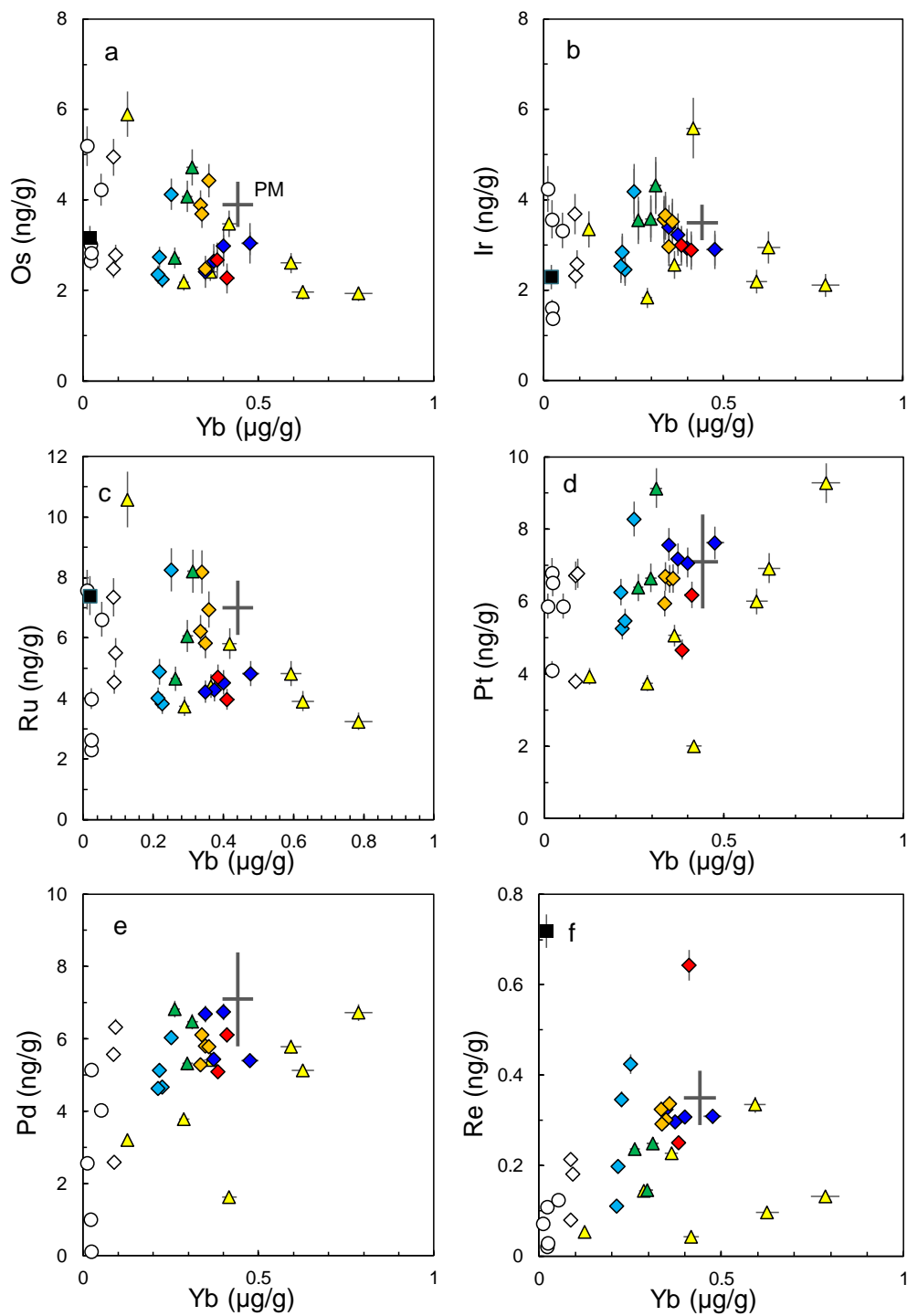


Figure 3.10. Plots of HSEs vs. Yb in Horoman peridotite samples. PM is the  $1\sigma$  range of primitive mantle value for Yb (McDonough and Sun, 1995) and primitive upper mantle value of Becker et al. (2006). Error bars in each sample is determined by  $1\sigma$  external precision of reference samples. Symbols are the same as in Figure 3.6.

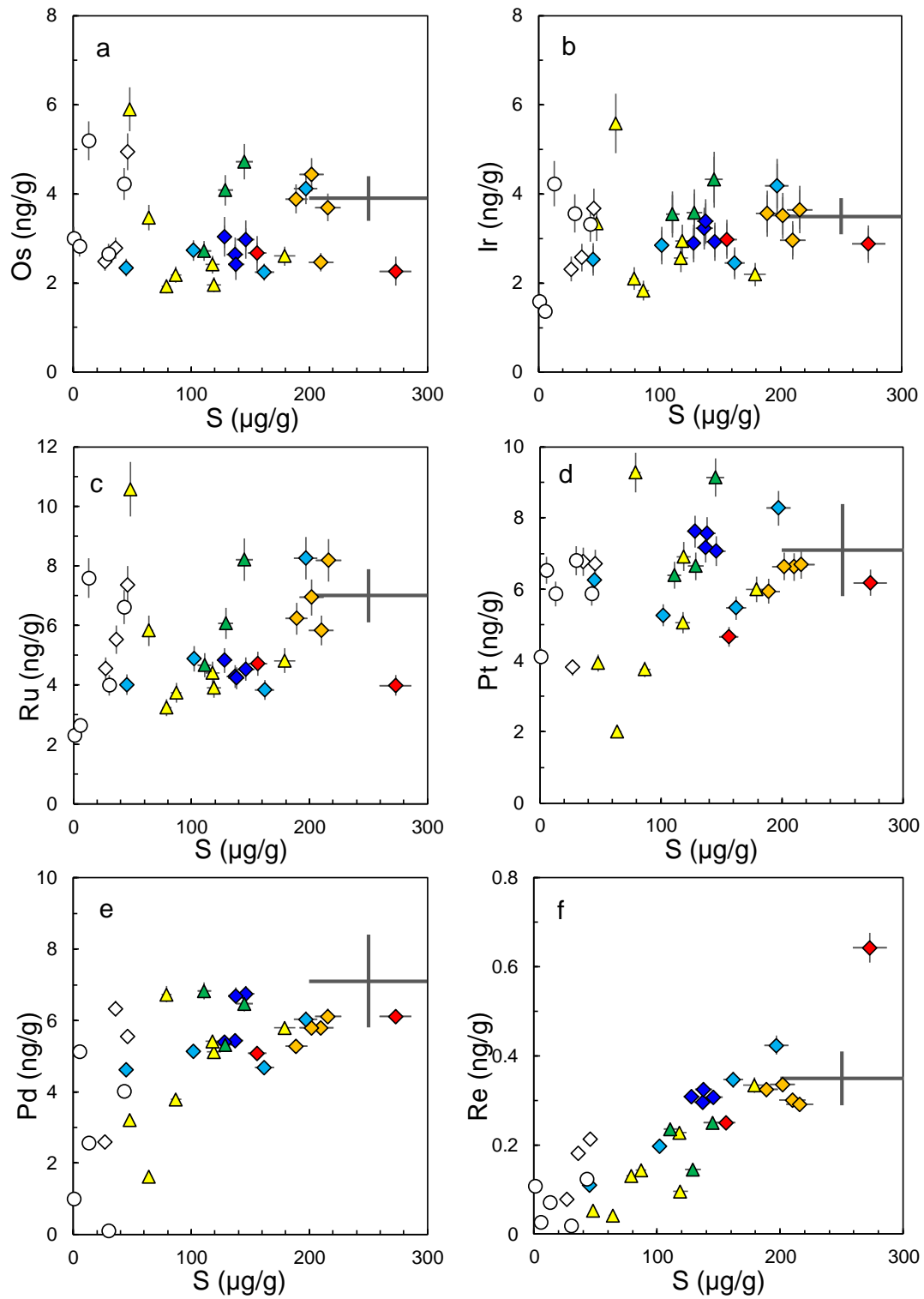


Figure 3.11. Plots of HSEs vs. S in Horoman peridotite samples. PM is the  $1\sigma$  range of primitive mantle value for S (McDonough and Sun, 1995) and primitive upper mantle value of Becker et al. (2006). Error bars in each sample is determined by  $1\sigma$  external precision of reference samples. Symbols are the same as in Figure 3.6.

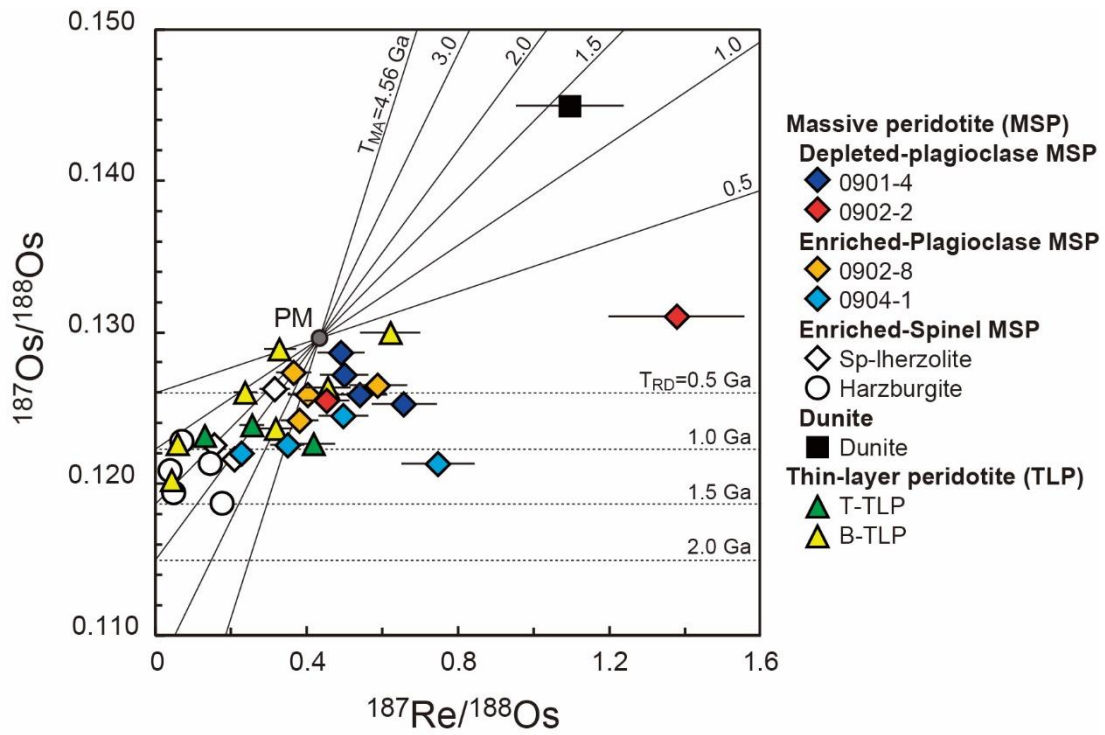


Figure 3.12. Re-Os isochron diagram for Horoman peridotite samples.  $T_{MA}$  ages are shown as solid lines;  $T_{RD}$  ages are shown as horizontal dashed lines.

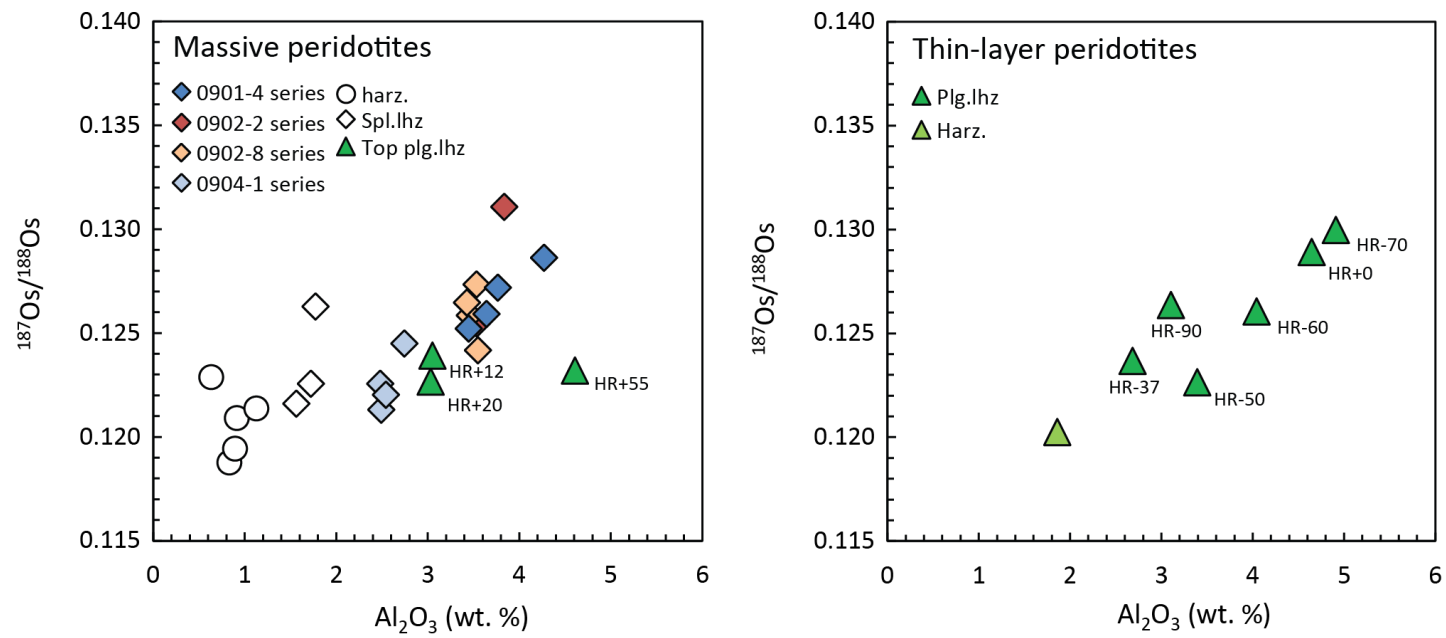


Figure 3.13. Plots of fertility indicator  $\text{Al}_2\text{O}_3$  vs.  $^{187}\text{Os}/^{188}\text{Os}$  for the massive (left) and thin-layer (right) peridotites. Three samples of T-TLP (HR+55, +20, +12) are plotted in massive peridotite diagram (left).

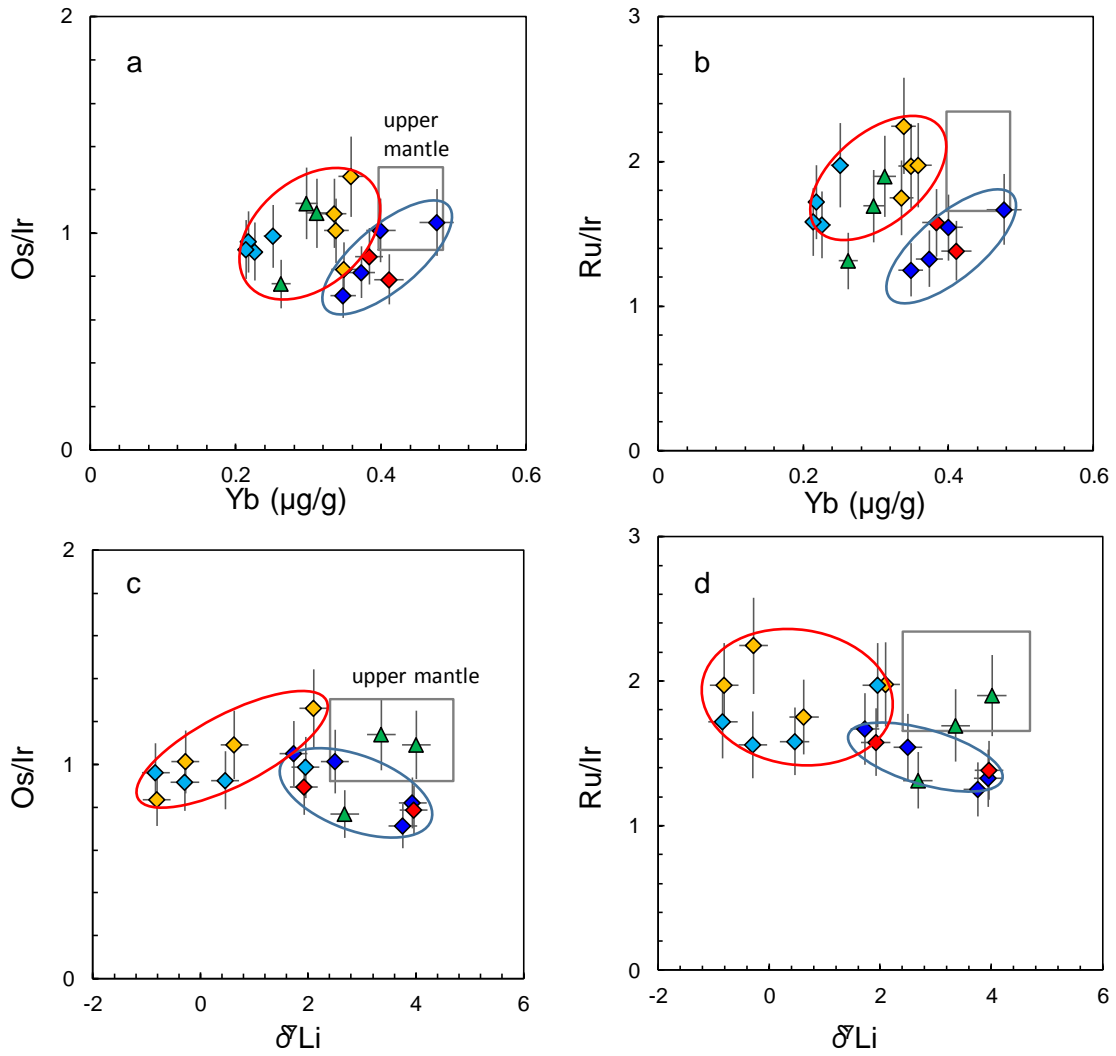


Figure 3.14. Plots of Os/Ir vs. Yb (a), Ru/Ir vs. Yb (b) and Os/Ir vs.  $\delta^7\text{Li}$  (c), Ru/Ir vs.  $\delta^7\text{Li}$  (d) for Horoman peridotite samples. Symbols are the same as in Figure 3.6.

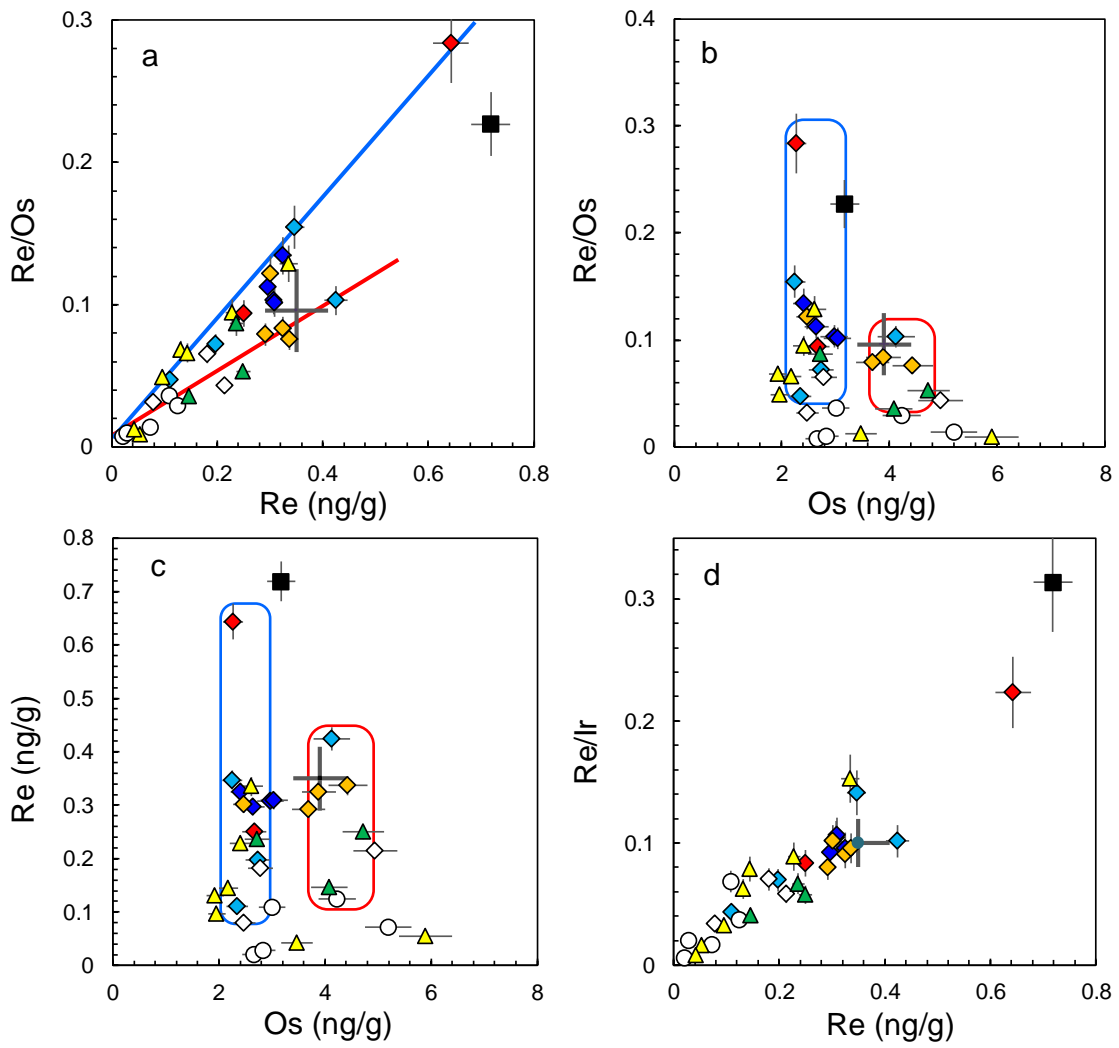


Figure 3.15. Plots of Re/Os vs. Re (a), Re/Os vs. Os (b), Re vs. Os (c), Re/Ir vs. Re (d) for Horoman peridotite samples. Blue and red indicate the low-Os and high-Os types of peridotites. Symbols are the same as in Figure 3.6.

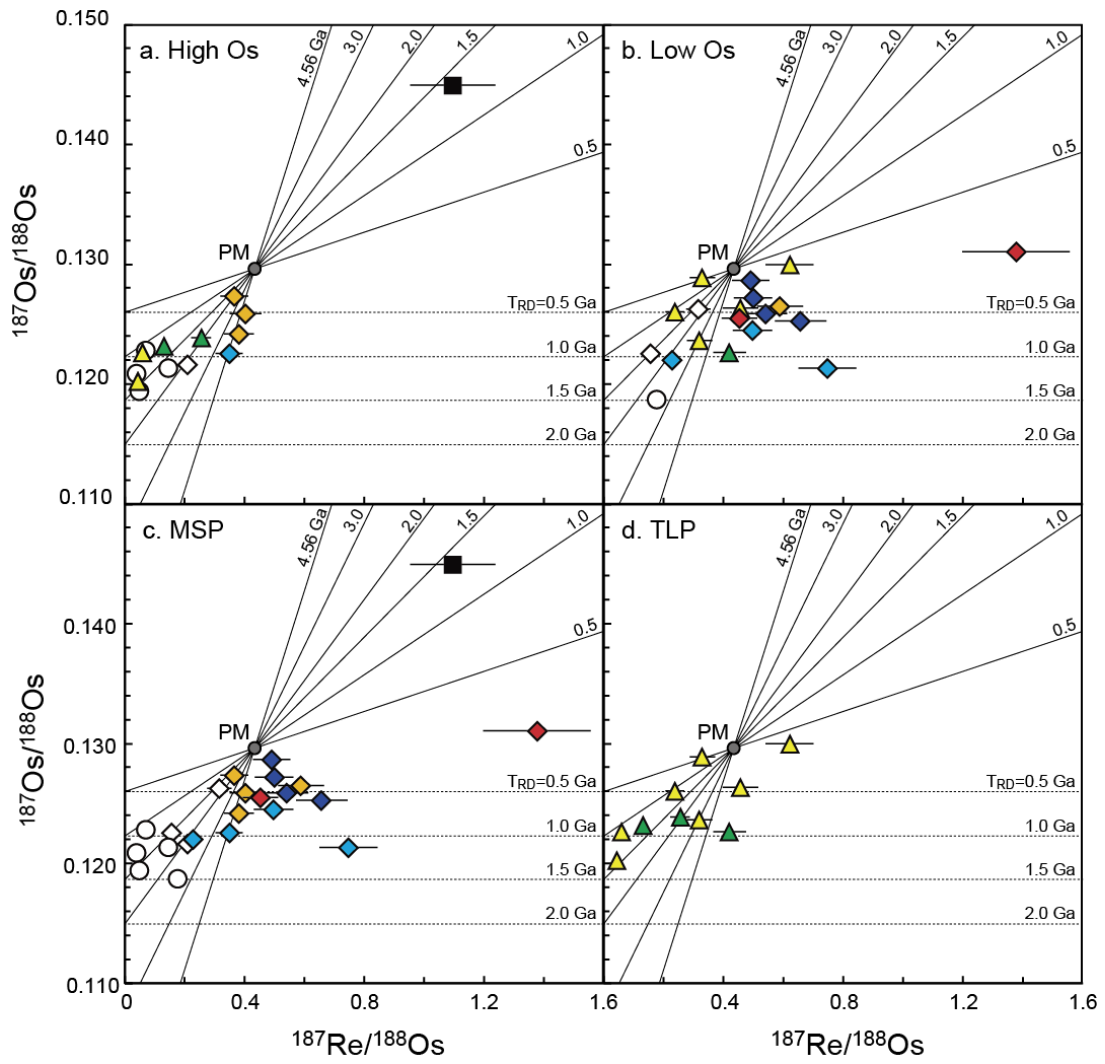


Figure 3.16. Re-Os isochron diagrams of Horoman peridotite samples. Blue and red indicate the low-Os and high-Os types of peridotites. Symbols are the same as in Figure 3.6.

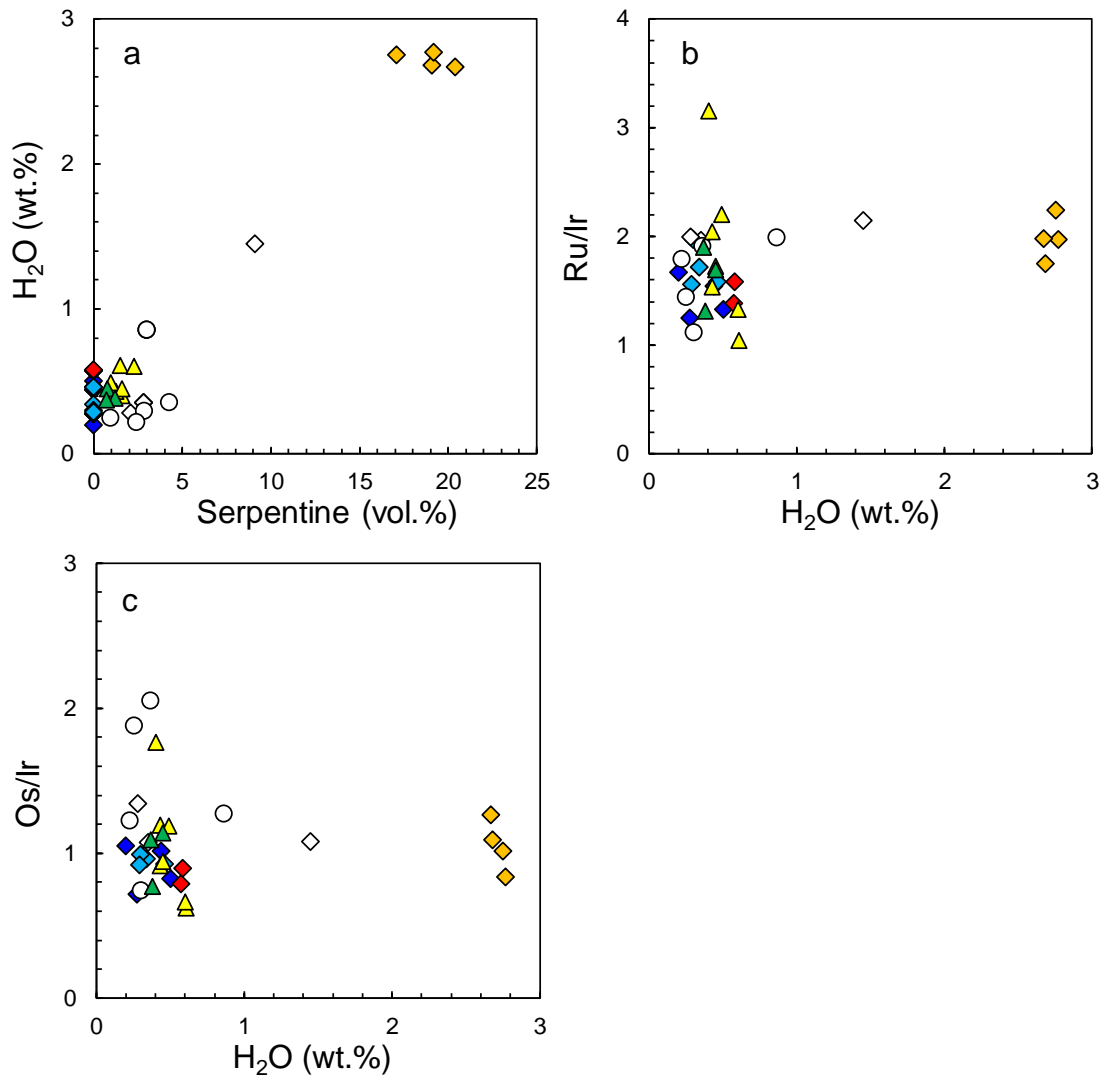


Figure 3.17. (a) Plot of modal abundances vs. H<sub>2</sub>O contents; (b) H<sub>2</sub>O vs. Ru/Ir, and (c) H<sub>2</sub>O content vs. Os/Ir of Horoman peridotite samples. The data for serpentine abundances and H<sub>2</sub>O contents are from Ranaweera et al. (2018). Symbols are the same as in Figure 3.6.

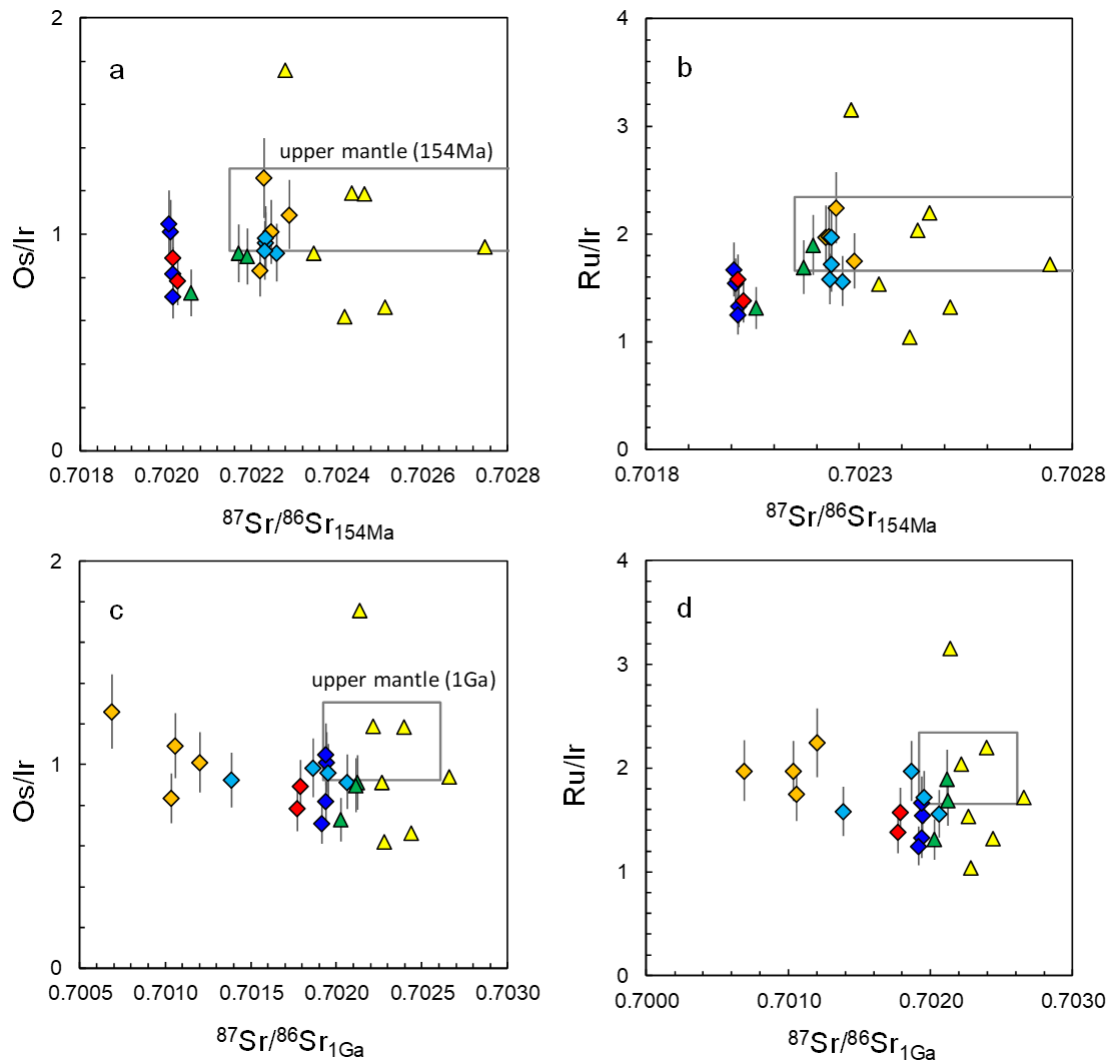


Figure 3.18. Initial  $^{87}\text{Sr}/^{86}\text{Sr}$  ratios of Horoman peridotite samples at 154 Ma (a and b) and 1 Ga (c and d). The Sr isotopic compositions of the upper mantle is between E-DMM and D-DMM of Workman and Hart (2005). The ranges of Os/Ir and Ru/Ir ratios in the upper mantle is  $\pm 1\sigma$  range of PUM after Becker et al. (2006). Symbols are the same as in Figure 3.6.

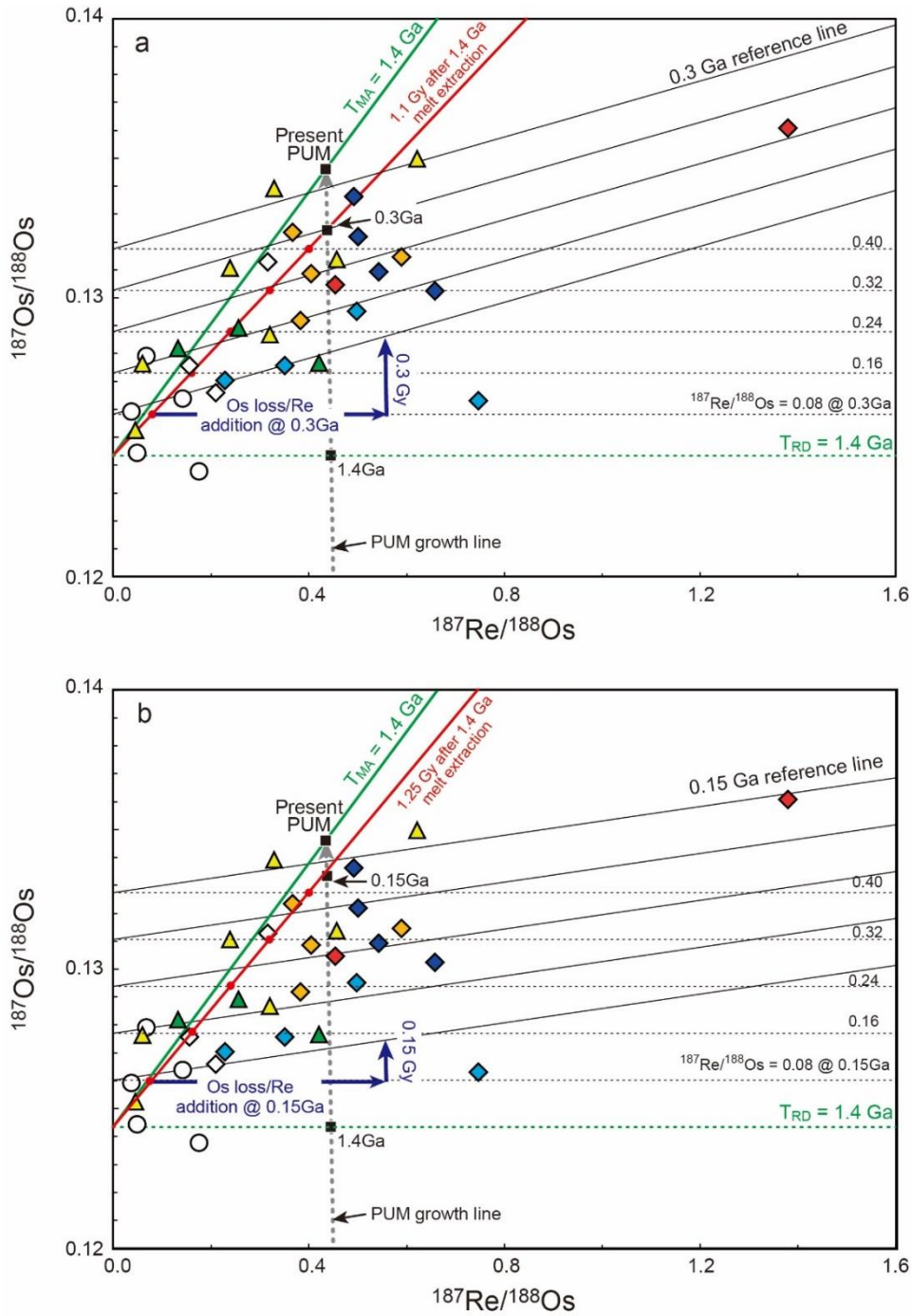


Figure 3.19. Re-Os isotope model calculation for estimation of the two-steps fractionation processes. The first step was melt extraction from the PUM composition at 1.4 Ga, the age of initial melt extraction was assumed by  $T_{RD}$  of the harzburgite samples. The secondary Re/Os fractionation was calculated at (a) 0.3 Ga when TLP were reacted with MORB-like melt and (b) 0.15 Ga when the fluid metasomatism was occurred for EP-MSP in the mantle wedge.

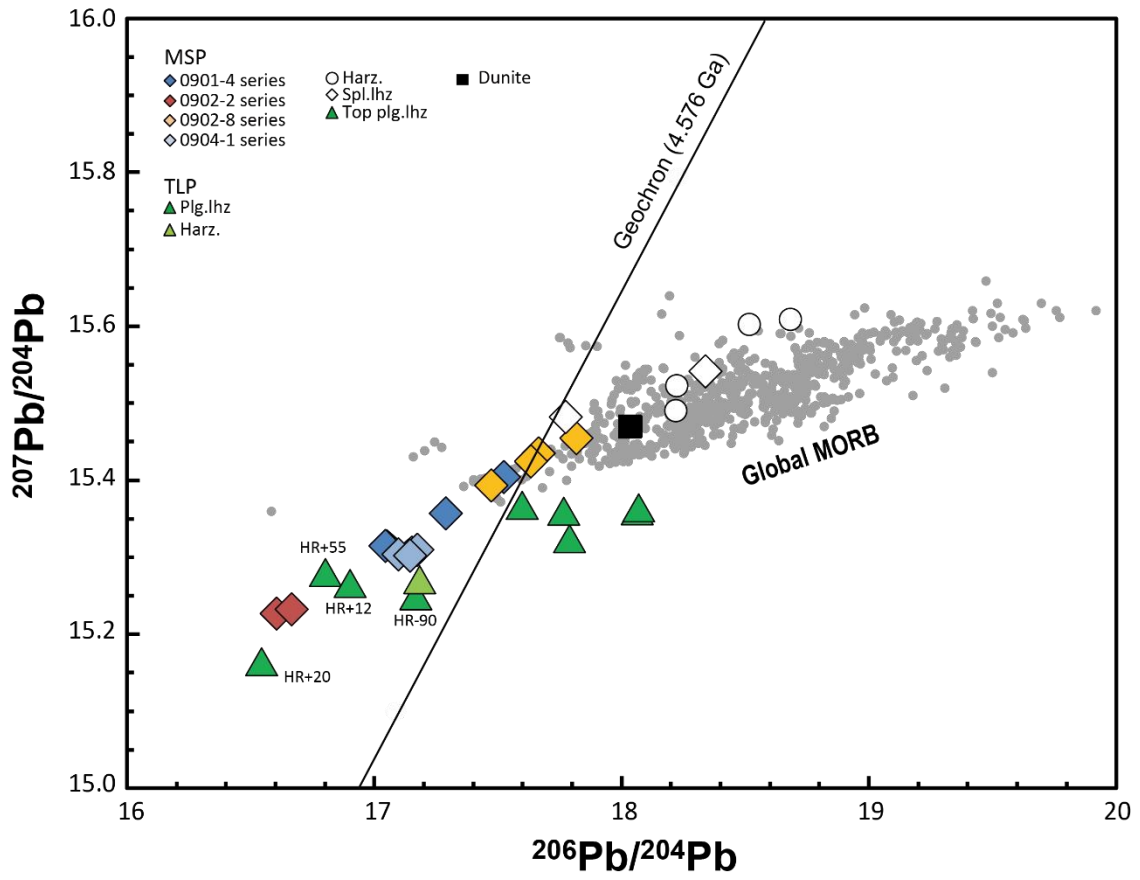


Figure 3.20. Pb isotopic compositions of the massive and thin-layer peridotites. The global MORB data (small grey circles) are from the PetDB Database

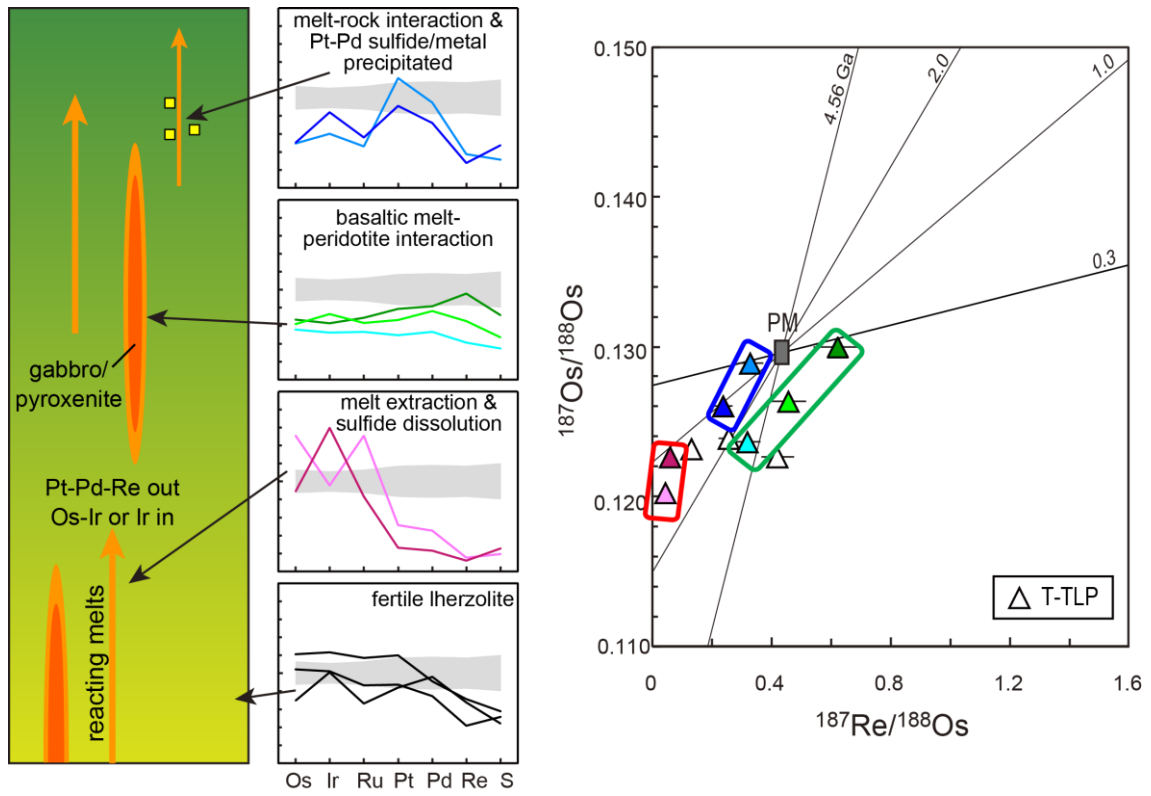


Figure 3.21. The classification of B-TLPs based on the HSE abundances and Re-Os isotope system.

Table 3.1 HSE mass fractions (ng g<sup>-1</sup>), Al<sub>2</sub>O<sub>3</sub> contents (wt. %) and Os model ages of Horoman peridotite samples from this study.

Sample	Os	Ir	Ru	Pt	Pd	Re	<sup>187</sup> Re/ <sup>188</sup> Os	<sup>187</sup> Os/ <sup>188</sup> Os	T <sub>MA</sub> (Ga)	T <sub>RD</sub> (Ga)	Al <sub>2</sub> O <sub>3</sub>	
<b>Massive peridotites</b>												
Plg.lhz	0901-4		2.88	4.15	7.46	7.47	0.308					3.77
	Duplicate	2.97	2.99	4.91	6.69	6.01	0.307	0.499	0.12720			
	0901-4a	2.64	3.22	4.28	7.17	5.45	0.297	0.542	0.12592			3.64
	0901-4b	3.04	2.89	4.83	7.62	5.40	0.309	0.491	0.12863			4.27
	0901-4c	2.66	3.64	4.21	7.51	7.23	0.318	0.577	0.12522			3.45
	Duplicate	2.16	3.13	4.25	7.64	6.16	0.331	0.738	0.12528			
	0902-2	2.15	2.91	3.88	6.28	6.26	0.683	1.534	0.13160			3.84
	Duplicate	2.38	2.84	4.08	6.09	5.97	0.603	1.224	0.13055			
	0902-2a	2.67	2.99	4.71	4.66	5.08	0.250	0.453	0.12546			3.54
	0902-8	3.89	3.56	6.23	5.94	5.28	0.325	0.404	0.12586			3.46
	0902-8a	2.47	2.96	5.83	6.62	5.80	0.301	0.589	0.12647			3.43
	0902-8b	3.69	3.65	8.19	6.70	6.12	0.292	0.382	0.12418			3.55
	0902-8c	4.43	3.51	6.94	6.64	5.79	0.336	0.367	0.12735			3.54
	0904-1	2.73	2.84	4.89	5.27	5.14	0.198	0.350	0.12257			2.48
	0904-1a	4.12	4.18	8.25	8.28	6.04	0.424	0.497	0.12451			2.74
	0904-1b	2.25	2.45	3.83	5.47	4.68	0.347	0.746	0.12132			2.49
	0904-1c	2.60	2.52	4.34	6.10	4.77	0.117	0.217	0.12227			2.54
Duplicate	2.09	2.55	3.68	6.42	4.47	0.104	0.240	0.12180				
Spl.lhz	0901-1	2.31	2.38	4.38	4.44	2.64	0.082	0.172	0.12317	1.5	0.9	1.72
	Duplicate	2.64	2.24	4.70	3.16	2.55	0.075	0.138	0.12196	1.5	1.0	
	0902-1	4.94	3.68	7.35	6.71	5.56	0.214	0.209	0.12160	2.1	1.1	1.57
0904-2	2.78	2.58	5.52	6.78	6.33	0.181	0.314	0.12628	1.6	0.5	1.78	
Hrz	0901-2	2.66	3.57	3.99	6.80	0.12	0.020	0.037	0.12092	1.3	1.2	0.91
	0901-3	5.19	4.24	7.59	5.87	2.58	0.072	0.067	0.12290	1.1	0.9	0.64
	0902-3	3.01	1.60	2.31	4.11	1.00	0.109	0.175	0.11877	2.5	1.5	0.83
	0902-10	4.02	3.43	6.41	6.20	4.15	0.127	0.153	0.12113	1.6	1.2	1.13
	Duplicate	4.43	3.22	6.82	5.55	3.90	0.121	0.132	0.12162	1.8	1.1	
0903-13	2.82	1.38	2.64	6.53	5.14	0.028	0.048	0.11944	1.6	1.4	0.89	
Dunite	0902-11	3.17	2.29	7.40	31.9	49.0	0.719	1.096	0.14493			1.86
<b>Thin-layer peridotites</b>												
Plg.lhz	HR+55	4.08	3.52	6.49	6.41	5.33	0.111	0.131	0.12319			4.61
	Duplicate		3.65	5.64	6.89	5.29	0.181					
	HR+20	2.72	3.55	4.66	6.39	6.83	0.236	0.419	0.12266			3.03
	HR+12	4.72	4.32	8.21	9.13	6.48	0.250	0.255	0.12391			3.05
	HR+0	1.93	2.11	3.24	9.28	6.74	0.131	0.329	0.12891			4.65
	HR-37	2.18	1.83	3.74	3.75	3.78	0.144	0.320	0.12367			2.69
	HR-50	3.47	5.58	5.82	2.00	1.63	0.043	0.059	0.12264			3.39
	HR-60	1.96	2.95	3.91	6.92	5.12	0.096	0.238	0.12606			4.04
	HR-70	2.60	2.19	4.82	6.00	5.79	0.335	0.621	0.12998			4.91
	HR-90	2.41	2.56	4.41	5.06	5.42	0.228	0.457	0.12636			3.11
Hrz	HR+5	5.90	3.35	10.57	3.93	3.21	0.054	0.044	0.12024			1.86

Values of PUM <sup>187</sup>Os/<sup>188</sup>Os=0.1296 and <sup>187</sup>Re/<sup>188</sup>Os=0.4346 used for the calculation of T<sub>MA</sub> and T<sub>RD</sub> ages (Meisel et al. 2001)

## Appendix



Figure A1. Photo of the amplifier assembly of TRITON Plus.

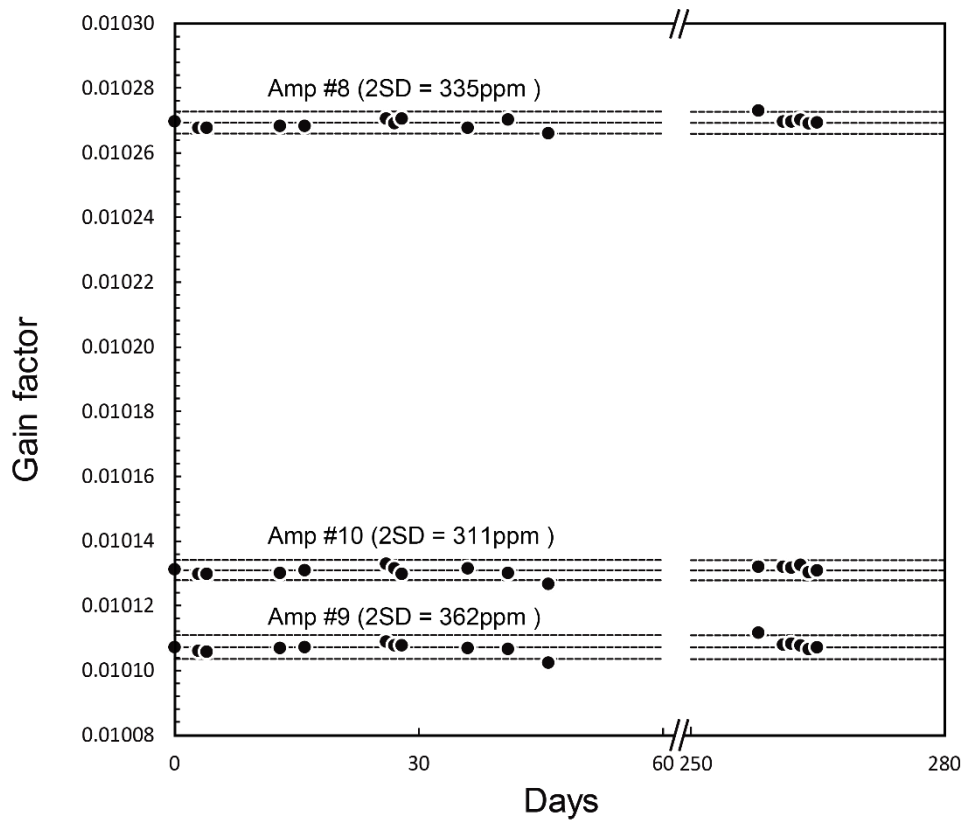


Figure A2. The gain factors of the three  $10^{13}\Omega$  amplifiers at negative mode from this study

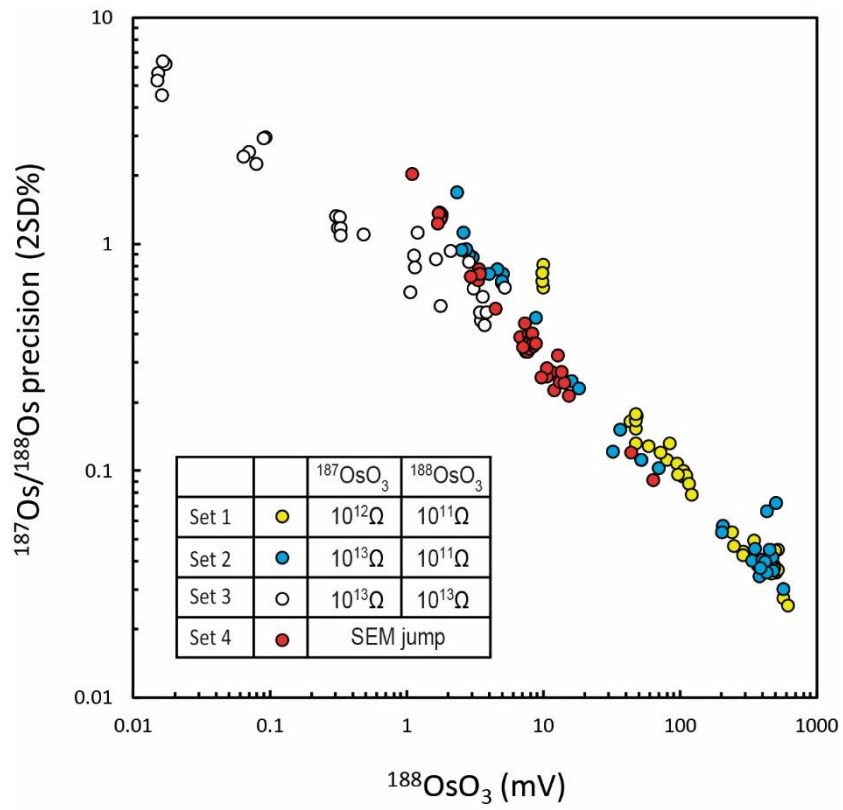


Figure A3. Comparison of analytical precision of  $^{187}\text{Os}/^{188}\text{Os}$  ratios measured by different sources

DROsS: Durham Romil Osmium solution

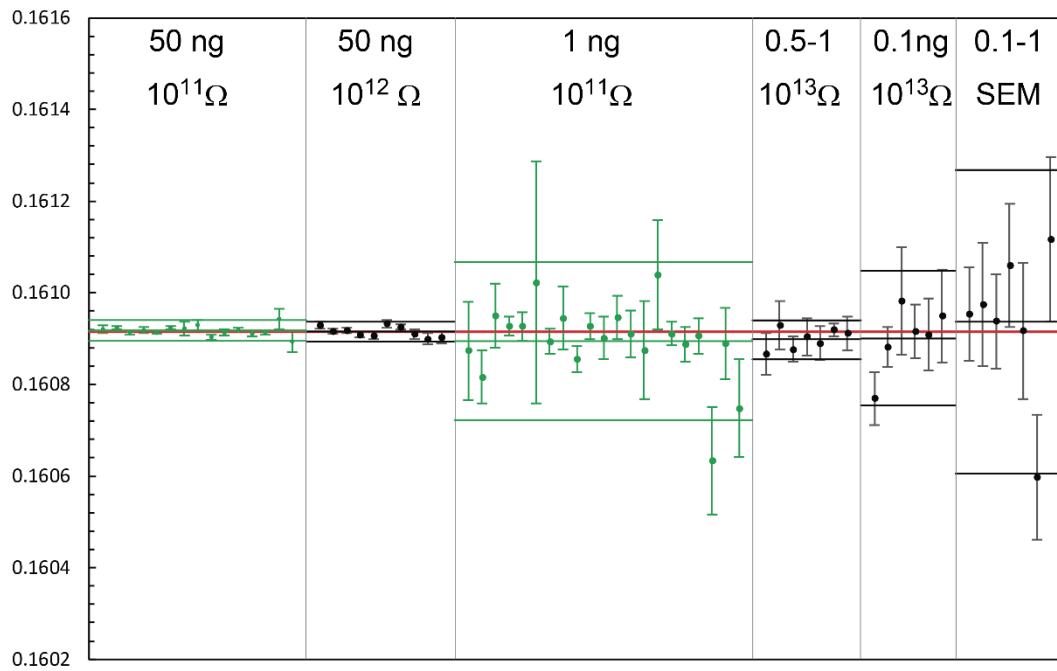


Figure A4. Comparison of  $^{187}\text{Os}/^{188}\text{Os}$  ratios using various amounts of the DROsS obtained by TRITON and TRITON Plus with different amplifiers. Green dot: TRITON data; Black dot: TRITON Plus data.

Table A1. Sequence of gain calibration

Cup	L3	L2	L1	C	H1	H2	H3
Mass	$^{184}\text{Os}^{16}\text{O}_3$ (232)	$^{186}\text{Os}^{16}\text{O}_3$ (234)	$^{187}\text{Os}^{16}\text{O}_3$ (235)	$^{188}\text{Os}^{16}\text{O}_3$ (236)	$^{189}\text{Os}^{16}\text{O}_3$ (237)	$^{190}\text{Os}^{16}\text{O}_3$ (239)	$^{192}\text{Os}^{16}\text{O}_3$ (241)
Seq. #1	$10^{12}\Omega$	$10^{12}\Omega$	$10^{12}\Omega$	$10^{11}\Omega$	$10^{12}\Omega$	$10^{11}\Omega$	$10^{11}\Omega$
Seq. #2	$10^{12}\Omega$	$10^{13}\Omega$ (Amp 9)	$10^{13}\Omega$ (Amp 8)	$10^{11}\Omega$	$10^{12}\Omega$	$10^{11}\Omega$	$10^{11}\Omega$
Seq. #3	$10^{12}\Omega$	$10^{13}\Omega$ (Amp 10)	$10^{13}\Omega$ (Amp 9)	$10^{11}\Omega$	$10^{12}\Omega$	$10^{11}\Omega$	$10^{11}\Omega$
Seq. #4	$10^{12}\Omega$	$10^{13}\Omega$ (Amp 8)	$10^{13}\Omega$ (Amp 10)	$10^{11}\Omega$	$10^{12}\Omega$	$10^{11}\Omega$	$10^{11}\Omega$
Seq. #5	$10^{12}\Omega$	$10^{12}\Omega$	$10^{12}\Omega$	$10^{11}\Omega$	$10^{12}\Omega$	$10^{11}\Omega$	$10^{11}\Omega$

Table A2. Total procedural blanks (ng), HSE mass fractions (ng g<sup>-1</sup>) and Os isotope ratios of UB-N from this study.

Sample		Os	Ir	Ru	Pt	Pd	Re	<sup>187</sup> Re/ <sup>188</sup> Os	<sup>187</sup> Os/ <sup>188</sup> Os	
<b>Total procedural blanks</b>										
CT	1	0.004	0.0002	0.002	0.006	0.008	0.0002			
	2	0.005	0.0002	0.002	0.005	0.005	0.0004			
	3	0.006	0.0001	0.007	0.014	0.008	0.0001			
	4	0.007	0.0001	0.001	0.025	0.028	0.0001			
	5		0.0000	0.002	0.013	0.008	0.0001			
<b>Reference material UB-N</b>										
CT	1	3.69	2.91	6.28	6.37	5.98	0.182	0.239	0.12727	
	2	3.58	3.43	6.38	6.90	5.60	0.190	0.256	0.12751	
	3		2.99	5.82	7.21	6.11	0.203			
	4	4.97*	3.85	8.41*	6.91	5.84	0.197	0.191	0.12652	
	5	4.18	3.52	7.16	7.47	6.02	0.180	0.208	0.12678	
	Mean	3.81	3.34	6.41	6.97	5.91	0.19	0.224	0.12702	
	1 SD	0.32	0.39	0.55	0.41	0.20	0.01	0.029	0.00045	
% RSD	8.4	12	8.7	5.9	3.4	5.2	13	0.36		
Ishikawa et al. (2012)	CT	mean(n=9)	6.85	5.55	0.210	3.47	6.98	3.97	0.257	0.12732
		RSD%	5.9	3.1	8.6	6.7	5.0	9.6	15	0.67
CT-HF	mean(n=4)	6.70	5.67	0.203	3.26	6.82	3.57	0.275	0.12720	
	RSD%	9.9	2.9	0.86	8.9	3.7	7.8	7.9	0.40	
Li et al. (2014)	CT	mean(n=5)	7.09	5.66	0.197	3.56	7.56	3.42	0.280	0.12700
		RSD%	16	6.3	6.6	16.2	4.0	11	7.6	0.16
Fischier et al. (2011)	CT	mean(n=8)	6.52	5.85	0.201	3.33	7.55	3.70		0.12704
		RSD%	6.2	3.4	5.9	5.0	5.0	8.4		0.20
Becker et al. (2006)	CT	mean(n=4)	6.51	5.86	0.205	3.26	7.00	3.51	0.282	0.12737
		RSD%	5.0	4.5	1.9	4.0	3.2	3.6	5.1	0.25
Luguet et al. (2007)	CT	mean(n=6)	6.48	6.17	0.205	3.24	8.07	3.66		0.12790
		RSD%	4.5	4.1	3.4	9.6	14	4.1		0.39
Puchtel et al. (2008)	CT	mean(n=4)	6.93	5.70	0.213	3.58	7.47	3.85		0.1272
		RSD%	3.4	1.1	2.6	5.6	1.1	4.2		0.15
Kogiso et al. (2008)	CT	mean(n=3)	6.23	6.05	0.190	3.38	7.40	3.56		
		RSD%	0.97	1.3	1.1	0.95	2.7	2.6		
Fischier et al. (2011)	HPA	mean(n=11)	6.36	5.86	0.184	3.02	7.16	3.46	0.257	0.12729
		RSD%	5.7	3.5	14	5.0	6.5	5.7	13	0.20
Meisel and Moser (2004)	HPA	mean(n=14)	6.30	6.11	0.206	3.38	7.42	3.71		
		RSD%	4.6	2.9	2.4	6.4	4.0	7.2		

\* nugget effect, CT: Carius tube, HPA: High pressure Asher, HF: Desilicification

Table A3. Relative percentage difference of duplicate Horoman peridotite samples from this study.

	Os	Ir	Ru	Pt	Pd	Re
	Duplicate samples, n=2					
0901-4		3.8	17	11	22	0.2
0901-4c	21	15	0.9	1.6	16	3.8
0902-2	10	2.4	5.1	3.2	4.9	12
0904-1c	21	1.5	16	5.1	6.5	11
0901-1	13	5.9	7.0	34	3.5	8.9
0902-10	9.7	6.5	6.2	11	6.3	4.6
HR+55		3.5	14	7.2	0.8	48
Mean	15	5.6	9.5	10	8.5	13

## References

- Barnes S. J., Naldrett A. J. and Gorton M. P. (1985)** The origin of the fractionation of platinum-group elements in terrestrial magmas. **Chemical Geology**, **53**, 303-323.
- Becker H. and Dale C. W. (2016)** Re–Pt–Os isotopic and highly siderophile element behavior in oceanic and continental mantle tectonites. **Reviews in Mineralogy and Geochemistry**, **81**, 369-440.
- Becker H., Horan M.F., Walker R.J., Gao S., Lorand J.P. and Rudnick R.L. (2006)** Highly siderophile element composition of the Earth's primitive upper mantle: Constraints from new data on peridotite massifs and xenoliths. **Geochimica et Cosmochimica Acta** **70**, 4528-4550.
- Becker H., Morgan J.W., Walker R.J., MacPherson G.J. and Grossman J.N. (2001a)** Rhenium osmium systematics of calcium-aluminium-rich inclusions in carbonaceous chondrites. **Geochimica et Cosmochimica Acta** **65**, 3379-3390.
- Becker H., Shirey S. B. and Carlson R. W. (2001b)** Effects of melt percolation on the Re–Os systematics of peridotites from a Paleozoic convergent plate margin. **Earth and Planetary Science Letters**, **188**, 107-121.
- Birck J.L., Barman M.R. and Capmas F. (1997)** Re-Os isotopic measurements at the femtomole level in natural samples. **Geostandards Newsletter: The Journal of Geostandards and Geoanalysis**, **21**, 19-27.
- Bockrath C., Ballhaus C., and Holzheid A. (2004)** Fractionation of the Platinum-Group Elements During Mantle Melting. **Science**, **305**, 1951–1953. doi:10.1126/science.1100160
- Bodinier J. L., Vasseur G., Vernieres J., Dupuy C. and Fabries J. (1990)** Mechanisms of mantle metasomatism: geochemical evidence from the Lherz orogenic peridotite. **Journal of Petrology**, **31**, 597-628.
- Bonatti E., Emiliani C., Ferrara G., Honnorez J. and Rydell H. (1974)** Ultramafic-carbonate breccias from the equatorial Mid Atlantic Ridge. **Marine Geology**, **16**, 83-102.
- Boudier F. and Coleman R. G. (1981)** Cross section through the peridotite in the Samail ophiolite, southeastern Oman Mountains. **Journal of Geophysical Research: Solid Earth**, **86**, 2573-2592.
- Bodinier J. L., Dupuy C. and Dostal J. (1988)** Geochemistry and petrogenesis of Eastern Pyrenean peridotites. **Geochimica et Cosmochimica Acta**, **52**, 2893-2907.
- Bodinier J. L., Menzies M. A. and Thirlwall M. F. (1991)** Continental to oceanic mantle transition—REE and Sr-Nd isotopic geochemistry of the Lanzo lherzolite massif. **Journal of Petrology**, **2**, 191-210.
- Brandon A.D., Norman M.D., Walker R.J. and Morgan J.W. (1999)** <sup>186</sup>Os-<sup>187</sup>Os systematics of Hawaiian picrites. **Earth and Planetary Science Letters**, **174**, 25-42.

- Brandon A.D. and Walker R.J. (2005)** The debate over core-mantle interaction. **Earth and Planetary Science Letters**, **232**, 211-225.
- Brandon A.D., Walker R.J. and Puchtel I.S. (2006)** Platinum-osmium isotope evolution of the Earth's mantle: Constraints from chondrites and Os-rich alloys. **Geochimica et Cosmochimica Acta**, **70**, 2093-2103.
- Brandon A. D., Creaser R. A., Shirey S. B. and Carlson R. W. (1996)** Osmium recycling in subduction zones. **Science**, **272**, 861-863.
- Brenan J. M., Bennet, N. R. and Zajacz Z. (2016)** Experimental results on fractionation of the highly siderophile elements (HSE) at variable pressures and temperatures during planetary and magmatic differentiation. **Reviews in Mineralogy and Geochemistry**, **81**, 1-87.
- Brueckner H. K. and Medaris L. G. (2000)** A general model for the intrusion and evolution of 'mantle' garnet peridotites in high-pressure and ultra-high-pressure metamorphic terranes. **Journal of Metamorphic Geology**, **18**, 123-133.
- Burnham O.M., Meisel T., and Kriete C. (2010)** OKUM and MUH-1: two new IAG-certified ultramafic rock reference materials. **Geochimica et Cosmochimica Acta**, **74**, A129.
- Cawthorn R. G. (1975)** The amphibole peridotite-metagabbro complex, Finero, northern Italy. **The Journal of Geology**, **83**, 437-454.
- Chatterjee R. and Lassiter J. C. (2015)** High precision Os isotopic measurement using N-TIMS: Quantification of various sources of error in  $^{186}\text{Os}/^{188}\text{Os}$  measurements. **Chemical Geology**, **396**, 112-123.
- Chou C. L. (1978)** Fractionation of siderophile elements in the Earth's upper mantle. **In Lunar and Planetary Science Conference Proceedings (Vol. 9)**.
- Chu Z., Yan Y., Chen Z., Guo J., Yang Y., Li C. and Zhang Y. (2015a)** A comprehensive method for precise determination of Re, Os, Ir, Ru, Pt, Pd concentrations and Os isotopic compositions in geological samples. **Geostandards and Geoanalytical Research**, **39**, 151-169.
- Chu Z. Y., Li C. F., Chen Z., Xu J. J., Di Y. K. and Guo J. H. (2015b)**. High-precision measurement of  $^{186}\text{Os}/^{188}\text{Os}$  and  $^{187}\text{Os}/^{188}\text{Os}$ : isobaric oxide corrections with in-run measured oxygen isotope ratios. **Analytical chemistry**, **87**, 8765-8771.
- Cohen A.S. and Waters F.G. (1996)** Separation of osmium from geological materials by solvent extraction for analysis by thermal ionisation mass spectrometry. **Analytica Chimica Acta**, **332**, 269-275.
- Coleman R. G. (1971)** Plate tectonic emplacement of upper mantle peridotites along continental edges. **Journal of Geophysical Research**, **76**, 1212-1222.

- Creaser R.A., Papanastassiou D.A. and Wasserburg G.J. (1991)** Negative thermal ion mass spectrometry of osmium, rhenium and iridium. *Geochimica et Cosmochimica Acta*, **55**, 397-401.
- Dale C. W., Burton K. W., Pearson D. G., Gannoun A., Alard O., Argles T. W. and Parkinson I. J. (2009)** Highly siderophile element behaviour accompanying subduction of oceanic crust: whole rock and mineral-scale insights from a high-pressure terrain. *Geochimica et Cosmochimica Acta*, **73**, 1394-1416.
- Dale C.W., Burton K.W., Greenwood R.C., Gannoun A., Wade J., Wood B.J. and Pearson D.G. (2012a)** Late accretion on the earliest planetesimals revealed by the highly siderophile elements. *Science*, **336**, 72-75.
- Dale C.W., Macpherson C.G., Pearson D.G., Hammond S.J. and Arculus R.J. (2012b)** Inter-element fractionation of highly siderophile elements in the Tonga Arc due to flux melting of a depleted source. *Geochimica et Cosmochimica Acta*, **89**, 202-225.
- Day J.M. and Walker R.J. (2015)** Highly siderophile element depletion in the Moon. *Earth and Planetary Science Letters*, **423**, 114-124.
- Day J., Waters C.L., Schaefer B.F., Walker R.J. and Turner S. (2016)** Use of hydrofluoric acid desilicification in the determination of highly siderophile element abundances and Re-Pt-Os isotope systematics in mafic-ultramafic rocks. *Geostandards and Geoanalytical Research*, **40**, 49-65.
- De Roever W.P. (1957)** Sind die alipionotypen peridotitmassen vielleicht tecnosch verfrachtete bruchstücke der Peridotitschale? *Geologische Rundschau* **46**, 137-146.
- Den Tex E. (1969)** Origin of ultramafic rocks, their tectonic setting and history: A contribution to the discussion of the paper "The origin of ultramafic and ultrabasic rocks" by PJ Wyllie. *Tectonophysics*, **7**, 457-488.
- Ely J.C., Neal C.R., O'Neill J.A. and Jain J.C. (1999)** Quantifying the platinum group elements (PGEs) and gold in geological samples using cation exchange pretreatment and ultrasonic nebulization inductively coupled plasma-mass spectrometry (USN-ICP-MS). *Chemical Geology*, **157**, 219-234.
- Fischer-Gödde M., Becker H. and Wombacher F. (2011)** Rhodium, gold and other highly siderophile elements in orogenic peridotites and peridotite xenoliths. *Chemical Geology*, **280**, 365-383.
- Frey F. A., Shimizu N., Leinbach A., Obata M., and Takazawa E. (1991)** Compositional variations within the lower layered zone of the Horoman peridotite, Hokkaido, Japan: constraints on models for melt-solid segregation. *Journal of Petrology*, **2**, 211-227.
- Green II H. W., Dobrzhinetskaya L., Riggs E. M. and Jin Z. M. (1997)** Alpe Arami: a peridotite massif from the Mantle Transition Zone? *Tectonophysics*, **279**, 1-21.

- Hartmann G. and Wedepohl K. H. (1993)** The composition of peridotite tectonites from the Ivrea Complex, northern Italy: residues from melt extraction. *Geochimica et Cosmochimica Acta*, **57**, 1761-1782.
- Hoffman E. L., Naldrett A. J., Van Loon J. C., Hancock R. G. V. and Manson A. (1978)** The determination of all the platinum group elements and gold in rocks and ore by neutron activation analysis after preconcentration by a nickel sulphide fire-assay technique on large samples. *Analytica Chimica Acta*, **102**, 157-166.
- Horan M.F., Walker R.J., Morgan J.W., Grossman J.N. and Rubin A.E. (2003)** Highly siderophile elements in chondrites. *Chemical Geology*, **196**, 27-42.
- Ishikawa A., Senda R., Suzuki K., Dale C. W. and Meisel T. (2014)** Re-evaluating digestion methods for highly siderophile element and <sup>187</sup>Os isotope analysis: Evidence from geological reference materials. *Chemical Geology*, **384**, 27-46.
- Jarvis I., Totland M.M. and Jarvis K.E. (1997a)** Determination of the platinum-group elements in geological materials by ICP-MS using microwave digestion, alkali fusion and cation-exchange chromatography. *Chemical Geology*, **143**, 27-42.
- Jarvis I., Totland M.M. and Jarvis K.E. (1997b)** Assessment of Dowex 1-X8-based anion-exchange procedures for the separation and determination of ruthenium, rhodium, palladium, iridium, platinum and gold in geological samples by inductively coupled plasma mass spectrometry. *Analyst*, **122**, 19-26.
- Jolivet L., Cadet J. P. and Lalevée F. (1988)** Mesozoic evolution of Northeast Asia and the collision of the Okhotsk microcontinent. *Tectonophysics*, **149**, 89-109.
- Kelemen P. B. (1990)** Reaction between ultramafic rock and fractionating basaltic magma I. Phase relations, the origin of calc-alkaline magma series, and the formation of discordant dunite. *Journal of Petrology*, **31**, 51-98.
- Kelemen P. B., Kikawa E., Miller D. J. and Party S. S. (2007)** Leg 209 summary: Processes in a 20-km-thick conductive boundary layer beneath the Mid-Atlantic Ridge, 14-16 N. In Proc. Ocean Drill. Program, *Sci. Results*, **209**, 1-33.
- Kelemen P. B., Shimizu N. and Salters V. J. (1995)** Extraction of mid-ocean-ridge basalt from the upwelling mantle by focused flow of melt in dunite channels. *Nature*, **375**, 747.
- Kiyokawa S. (1992)** Geology of the Idonnappu belt, central Hokkaido, Japan: Evolution of a Cretaceous accretionary complex. *Tectonics*, **11**, 1180-1206.
- Kogiso T., Suzuki K., Suzuki T., Shinotsuka K., Uesugi K., Takeuchi A. and Suzuki Y. (2008)** Detecting micrometer-scale platinum-group minerals in mantle peridotite with microbeam synchrotron radiation X-ray fluorescence analysis. *Geochemistry, Geophysics, Geosystems*, **9**, Q03018, doi:10.1029/2007GC001888.

- Komatsu M. Miyashita S. Maeda J. Osanai Y. and Toyoshima T. (1983)** Disclosing of a deepest section of continental-type crust up-thrust as the final event of collision of arcs in Hokkaido, north Japan. **In Hashimoto M. and Uyeda S(eds.)** Accretion Tectonics in the Circum-Pacific Regions, 149-165.
- Komatsu M. and Noci M. (1996)** Ultrabasic rocks in the Hidaka metamorphic belt, Hokkaido, Japan I. Mode of occurrence of the Horoman ultrabasic rocks. **Earth Science** **20**, 21-29.
- Korkish J. (1989)** Handbook of ion exchange resins: The application to analytical inorganic analytical chemistry. **CRC Press (Boca Raton, USA)**, 352pp.
- Li J., Jiang X.Y., Xu J.F., Zhong L.F., Wang X.C., Wang G.Q. and Zhao P.P. (2014)** Determination of platinum-group elements and Re-Os isotopes using ID-ICP-MS and N-TIMS from a single digestion after two-stage column separation. **Geostandards and Geoanalytical Research**, **38**, 37-50.
- Li J., Zhao P.P., Liu J., Wang X.C., Yang A.Y., Wang G.Q. and Xu J.F. (2015)** Reassessment of hydrofluoric acid desilicification in the Carius tube digestion technique for Re-Os isotopic determination in geological samples. **Geostandards and Geoanalytical Research**, **39**, 17-30.
- Liu J. and Pearson D.G. (2014)** Rapid, precise and accurate Os isotope ratio measurements of nanogram to sub-nanogram amounts using multiple Faraday collectors and amplifiers equipped with  $10^{12} \Omega$  resistors by N-TIMS. **Chemical Geology**, **363**, 301-311.
- Le Roux V., Bodinier J. L., Tommasi A., Alard O., Dautria J. M., Vauchez A. and Riches A. J. V. (2007)** The Lherz spinel lherzolite: refertilized rather than pristine mantle. **Earth and Planetary Science Letters**, **259**, 599-612.
- Lorand J. P., Alard O. and Godard M. (2009)** Platinum-group element signature of the primitive mantle rejuvenated by melt - rock reactions: evidence from Sumail peridotites (Oman Ophiolite). **Terra Nova**, **21**, 35-40.
- Luguet A., Nowell G.M. and Pearson D.G. (2008)**  $^{184}\text{Os}/^{188}\text{Os}$  and  $^{186}\text{Os}/^{188}\text{Os}$  measurements by negative thermal ionisation mass spectrometry (N-TIMS): Effects of interfering element and mass fractionation corrections on data accuracy and precision. **Chemical Geology**, **248**, 342-362.
- Luguet A., Shirey S.B., Lorand J.P., Horan M.F. and Carlson R.W. (2007)** Residual platinum-group minerals from highly depleted harzburgites of the Lherz massif (France) and their role in HSE fractionation of the mantle. **Geochimica et Cosmochimica Acta**, **71**, 3082-3097.
- Makishima A. and Nakamura E. (2001)** Determination of total sulfur at microgram per gram levels in geological materials by oxidation of sulfur into sulfate with in situ generation of bromine using isotope dilution high-resolution ICPMS. **Analytical chemistry**, **73**, 2547-2553.

- Makishima A., Tanaka R. and Nakamura E. (2009)** Precise elemental and isotopic analyses in silicate samples employing ICP-MS: Application of hydrofluoric acid solution and analytical techniques. *Analytical Sciences*, **25**, 1181-1187.
- Malaviarachchi S. P. K., Makishima A. and Nakamura E. (2010)** Melt-peridotite reactions and fluid metasomatism in the upper mantle, revealed from the geochemistry of peridotite and gabbro from the Horoman peridotite massif, Japan. *Journal of Petrology*, **51**, 1417–1445. doi:10.1093/petrology/egq024
- Malaviarachchi S. P. K., Makishima A., Tanimoto M., Kuritani T. and Nakamura E. (2008)** Highly unradiogenic lead isotope ratios from the Horoman peridotite in Japan. *Nature Geoscience*, **1**, 859–863. doi:10.1038/ngeo363
- Martin C. E. (1991)** Osmium isotopic characteristics of mantle-derived rocks. *Geochimica et Cosmochimica Acta*, **55**, 1421-1434.
- McDonough W.F. and Sun S-s (1995)** The composition of the Earth. *Chemical Geology*, **120**, 223-253.
- Menzies M., Blanchard D., Brannon J. and Korotev R. (1977)** Rare earth geochemistry of fused ophiolitic and alpine lherzolites. *Contributions to Mineralogy and Petrology*, **64**, 53-74.
- Medaris G., Wang H., Jelínek E., Mihaljevič M. and Jakeš P. (2005)** Characteristics and origins of diverse Variscan peridotites in the Gföhl nappe, Bohemian Massif, Czech Republic. *Lithos*, **82**, 1-23.
- Meisel T., Burnham M., Kriete C., Bokhari S.N. and Schulz T. (2013)** Osmium isotope and PGE reference materials OKUM and MUH-1. *Mineralogical Magazine*, **77**, 1734.
- Meisel T., Dale C., Pearson D. and Sergeev D. (2009)** Complete sample digestions for accurate isotope measurements? The Re-Os isotope system under scrutiny. *Geochimica et Cosmochimica Acta Supplement*, **73**, 867.
- Meisel T. and Horan M.F. (2016)** Analytical methods for the highly siderophile elements. *Reviews in Mineralogy and Geochemistry*, **81**, 89-106.
- Meisel T., Moser J., Fellner N., Wegscheider W. and Schoenberg R. (2001)** Simplified method for the determination of Ru, Pd, Re, Os, Ir and Pt in chromitites and other geological materials by isotope dilution ICP-MS and acid digestion. *Analyst*, **126**, 322-328.
- Meisel, T., Fellner, N. and Moser, J. (2003a)** A simple procedure for the determination of platinum group elements and rhenium (Ru, Rh, Pd, Re, Os, Ir and Pt) using ID-ICP-MS with an inexpensive on-line matrix separation in geological and environmental materials. *Journal of Analytical Atomic Spectrometry*, **18**, 720-726.
- Meisel T., Reisberg L., Moser J., Carignan J., Melcher F. and Brüggmann G. (2003b)** Re-Os systematics of UB-N, a serpentinised peridotite reference material. *Chemical Geology*, **201**, 161-179.

- Meisel T. and Moser J. (2004a)** Platinum-group element and rhenium concentrations in low abundance reference materials. **Geostandards and Geoanalytical Research**, **28**, 233-250.
- Meisel T. and Moser J. (2004b)** Reference materials for geochemical PGE analysis: New analytical data for Ru, Rh, Pd, Os, Ir, Pt and Re by isotope dilution ICP-MS in 11 geological reference materials. **Chemical Geology**, **208**, 319-338.
- Meisel T., Walker R. J., Irving A. J., and Lorand J. P. (2001)** Osmium isotopic compositions of mantle xenoliths: a global perspective. **Geochimica et Cosmochimica Acta**, **65**, 1311-1323.
- Menzies M. A. and Dupuy C. (1991)** Orogenic massifs: protolith, process and provenance. **Journal of Petrology**, **2**, 1-16.
- Miyashita S. (1983)** Reconstructions of the ophiolite succession in the western zone of the Hidaka Metamorphic Belt, Hokkaido. **Journal of the Geological Society of Japan** **89**, 69-86.
- Mitchell R. H. and Keays R. R. (1981)** Abundance and distribution of gold, palladium and iridium in some spinel and garnet lherzolites: implications for the nature and origin of precious metal-rich intergranular components in the upper mantle. **Geochimica et Cosmochimica Acta**, **45**, 2425-2442.
- Morgan J. W. (1986)** Ultramafic xenoliths: clues to Earth's late accretionary history. **Journal of Geophysical Research: Solid Earth**, **91**, 12375-12387.
- Morgan J. W., Wandless G. A., Petrie R. K. and Irving A. J. (1981)** Composition of the Earth's upper mantle—I. Siderophile trace elements in ultramafic nodules. **Tectonophysics**, **75**, 47-67.
- Morgan J. W. and Walker R. J. (1989)** Isotopic determinations of rhenium and osmium in meteorites by using fusion, distillation and ion-exchange separations. **Analytica Chimica Acta**, **222**, 291-300.
- Münker C., Weyer S., Scherer E. and Mezger K. (2001)** Separation of high field strength elements (Nb, Ta, Zr, Hf) and Lu from rock samples for MC-IPMS measurements. **Geochemistry, Geophysics, Geosystems**, **2**, 10.1029/2001GC000183.
- Nakamura E., Makishima A., Moriguti T., Kobayashi K., Sakaguchi C., Yokoyama T., Tanaka R., Kuritani T. and Takei H. (2003)** Comprehensive geochemical analyses of small amounts (< 100 mg) of extraterrestrial samples for the analytical competition related to the sample return mission MUSES-C. **ISAS Report SP**, **16**, 49-101.
- Nanayama F. (1992)** Stratigraphy and facies of the Paleocene Nakanogawa Group in the southern part of central Hokkaido, Japan. **J. Geol. Soc. Japan**, **98**, 1041-1059.
- Niida K. (1984)** Petrology of the Horoman ultramafic rocks. *Journal of Faculty of Sciences, Hokkaido University, Series IV* **21**, 61-81.
- Niida K. and Katoh T. (1978)** Ultramafic rocks in Hokkaido. **Monography of the association for the geological collaboration in Japan** **21**, 61-81.

- Niida K. and Takazawa E. (2007)** Origin of layering observed in the Horoman peridotite complex, Japan. **Journal of the Geological Society of Japan, Supplement 113**, 167-184.
- Nier A.O. (1937)** The isotopic constitution of osmium. **Physical Review**, **52**, 885.
- O'hara M. J. (1967)** Mineral parageneses in ultrabasic rocks. Ultramafic and related rocks, 393-403.
- Osanai Y., Komatsu M. and Owada M. (1991)** Metamorphism and granite genesis in the Hidaka metamorphic belt, Hokkaido, Japan. **Journal of Metamorphic Geology**, **9**, 111-124.
- Obata M. and Nagahara N. (1987)** layering of alpine - Type peridotite and the segregation of partial melt in the upper mantle. **Journal of Geophysical Research: Solid Earth**, **92**, 3467-3474.
- Pattou L., Lorand J. P. and Gros M. (1996)** Non-chondritic platinum-group element ratios in the Earth's mantle. **Nature**, **379**, 712.
- Pearson D.G. and Woodland S.J. (2000)** Solvent extraction/anion exchange separation and determination of PGEs (Os, Ir, Pt, Pd, Ru) and Re–Os isotopes in geological samples by isotope dilution ICP-MS. **Chemical Geology**, **165**, 87-107.
- Prinz M., Keil K., Green J. A., Reid A. M., Bonatti E. and Honnorez J. (1976)** Ultramafic and mafic dredge samples from the equatorial Mid-Atlantic ridge and fracture zones. **Journal of Geophysical Research**, **81**, 4087-4103.
- Puchtel I.S., Walker R.J., James O.B. and Kring D.A. (2008)** Osmium isotope and highly siderophile element systematics of lunar impact melt breccias: Implications for the late accretion history of the Moon and Earth. **Geochimica et Cosmochimica Acta**, **72**, 3022-3042.
- Puchtel I. S. and Humayun M. (2001)** Platinum group element fractionation in a komatiitic basalt lava lake. **Geochimica et Cosmochimica Acta**, **65**, 2979-2993.
- Qi L., Zhou M.F. and Wang C.Y. (2004)** Determination of low concentrations of platinum group elements in geological samples by ID-ICP-MS. **Journal of Analytical Atomic Spectrometry**, **19**, 1335-1339.
- Qi L. and Zhou M.F. (2008)** Platinum-group elemental and Sr-Nd-Os isotopic geochemistry of Permian Emeishan flood basalts in Guizhou Province, SW China. **Chemical Geology**, **248**, 83-103.
- Obata M. and Nagahara N. (1987)** layering of alpine-Type peridotite and the segregation of partial melt in the upper mantle. **Journal of Geophysical Research: Solid Earth**, **92**, 3467-3474.
- Rampone E. and Morten L. (2001)** Records of crustal metasomatism in the garnet peridotites of the Ulten Zone (Upper Austroalpine, Eastern Alps). **Journal of Petrology**, **42**, 207-219.
- Ranaweera L. V., Ota T., Moriguti T., Tanaka R. and Nakamura E. (2018)** Circa 1 Ga sub-seafloor hydrothermal alteration imprinted on the Horoman peridotite massif. **Scientific reports**, **8**, 9887.

- Rehkämper M. and Halliday A.N. (1997)** Development and application of new ion exchange techniques for the separation of the platinum group and other siderophile elements from geological samples. *Talanta*, **44**, 663-672.
- Rehkämper M., Halliday A. N., Alt J., Fitton J. G., Zipfel J. and Takazawa E. (1999)** Non-chondritic platinum-group element ratios in oceanic mantle lithosphere: petrogenetic signature of melt percolation?. *Earth and Planetary Science Letters*, **172**, 65-81.
- Ren M., Sun Y., Wang C.Y. and Sun S. (2016)** Determination of platinum-group elements in geological samples by isotope dilution-inductively coupled plasma-mass spectrometry combined with sulfide fire assay preconcentration. *Geostandards and Geoanalytical Research*, **40**, 67-83.
- Reisberg L. C., Allègre, C. J. and Luck J. M. (1991)** The Re-Os systematics of the Ronda ultramafic complex of Southern Spain. *Earth and Planetary Science Letters*, **105**, 196-213.
- Reisberg L. and Lorand J. P. (1995)** Longevity of sub-continental mantle lithosphere from osmium isotope systematics in orogenic peridotite massifs. *Nature*, **376**, 159.
- Rudnick R. L. and Walker R. J. (2009)** Interpreting ages from Re-Os isotopes in peridotites. *Lithos*, **112**, 1083-1095.
- Saal A. E., Takazawa E., Frey F. A., Shimizu N. and Hart S. R. (2001)** Re-Os isotopes in the Horoman Peridotite: evidence for refertilization? *Journal of Petrology*, **42**, 25-37. doi:10.1093/petrology/42.1.25
- Sawlowicz Z. (1993)** Iridium and other platinum-group elements as geochemical markers in sedimentary environments. *Palaeogeography, Palaeoclimatology, Palaeoecology*, **104**, 253-270.
- Savard D., Barnes S J. and Meisel T. (2010)** Comparison between nickel-sulfur fire assay Te Co-precipitation and isotope dilution with high-pressure asher acid digestion for the determination of platinum-group elements, rhenium and gold. *Geostandards and Geoanalytical Research*, **34**, 281-291.
- Shen J.J., Papanastassiou D.A. and Wasserburg G.J. (1996)** Precise Re-Os determinations and systematics of iron meteorites. *Geochimica et Cosmochimica Acta*, **60**, 2887-2900. ¥
- Shiba M. Kawamura M. and Onuki H. (1992)** Granulite facies metamorphism in the southern part of the Hidaka metamorphic belt. *Chikyu Monthly* **155**, 300-305.
- Shinotsuka K. and Suzuki K. (2007)** Simultaneous determination of platinum group elements and rhenium in rock samples using isotope dilution inductively coupled plasma mass spectrometry after cation exchange separation followed by solvent extraction. *Analytica Chimica Acta*, **603**, 129-139.
- Shirey S.B. and Walker R.J. (1995)** Carius tube digestion for low-blank rhenium-osmium analysis. *Analytical Chemistry*, **67**, 2136-2141.

- Shirey S. B. and Walker R. J. (1998)** The Re-Os isotope system in cosmochemistry and high-temperature geochemistry. **Annual Review of Earth and Planetary Sciences**, **26**, 423-500.
- Smoliar M.I., Walker R.J. and Morgan J.W. (1996)** Re-Os ages of group IIA, IIIA, IVA, and IVB iron meteorites. **Science**, **271**, 1099-1102.
- Snow J. E. and Schmidt G. (1998)** Constraints on Earth accretion deduced from noble metals in the oceanic mantle. **Nature**, **391**, 166.
- Takahashi N. (1991)** Origin of three peridotite suites from Horoman peridotite complex, Hokkaido, Japan; Melting, melt segregation and solidification processes in the upper mantle. **Journal of Mineralogy, Petrology and Economic Geology**, **86**, 199-215.
- Takazawa E. (1996)** Geodynamic evolution of the Horoman peridotite, Japan: geochemical study of lithospheric and asthenospheric processes (Doctoral dissertation, Massachusetts Institute of Technology Cambridge, MA, 562 pp.).
- Takazawa E., Frey F. A and Obata M. (2000)** Whole rock compositional variations in an upper mantle peridotite (Horoman, Hokkaido, Japan): Are they consistent with a partial melting process? **Geochimica et Cosmochimica Acta**, **64**, 695.
- Takazawa E., Frey F. A., Shimizu N., Saal A. and Obata M. (1999)** Petrogenesis of mafic layers in the Horoman peridotite complex, Japan. **Ofioliti**, **24**, 173. doi:10.1093/etroj/40.12.1827
- Toyoshima T. Komatsu M. and Shimura T. (1994)** Tectonic evolution of lower crustal rocks in an exposed magmatic arc section in the Hidaka metamorphic belt, Hokkaido, northern Japan. **Island Arc**, **3**, 182-198.
- Trinquier A. (2014)** Gain calibration protocol for  $10^{13} \Omega$  resistor current amplifiers using the certified neodymium standard JNdi-1 on the TRITON Plus. **Technical note**, 30285.
- Tubia J. M. and Cuevas J. (1986)** High-temperature emplacement of the Los Reales peridotite nappe (Betic Cordillera, Spain). **Journal of Structural Geology**, **8**, 473-482.
- Völkening J., Walczyk T., and Heumann K.G. (1991)** Osmium isotope ratio determinations by negative thermal ionization mass spectrometry. **International Journal of Mass Spectrometry and Ion Processes**, **105**, 147-159.
- Walker R.J., Brandon A.D., Bird J.M., Piccoli P.M., McDonough W.F. and Ash R.D. (2005)**  $^{187}\text{Os}$ - $^{186}\text{Os}$  systematics of Os-Ir-Ru alloy grains from southwestern Oregon. **Earth and Planetary Science Letters**, **230**, 211-226.
- Walker R. J., Carlson R. W., Shirey S. B. and Boyd F. R. (1989)** Os, Sr, Nd, and Pb isotope systematics of southern African peridotite xenoliths: implications for the chemical evolution of subcontinental mantle. **Geochimica et Cosmochimica Acta**, **53**, 1583-1595.
- Walker R. J., Prichard H. M., Ishiwatari A. and Pimentel M. (2002)** The osmium isotopic composition of convecting upper mantle deduced from ophiolite chromites. **Geochimica et Cosmochimica Acta**, **66**, 329-345.

- Wang Z. and Becker H. (2014)** Abundances of sulfur, selenium, tellurium, rhenium and platinum-group elements in eighteen reference materials by isotope dilution sector-field ICP-MS and negative TIMS. *Geostandards and Geoanalytical Research*, **38**, 189-209.
- Wittig N., Pearson D.G., Baker J.A., Duggen S. and Hoernle K. (2010)** A major element, PGE and Re-Os isotope study of Middle Atlas (Morocco) peridotite xenoliths: Evidence for coupled introduction of metasomatic sulphides and clinopyroxene. *Lithos*, **115**, 15-26.
- Workman R. K. and Hart S. R. (2005)** Major and trace element composition of the depleted MORB mantle (DMM). *Earth and Planetary Science Letters*, **231**, 53-72.
- Yamakawa A., Yamashita K., Makishima A. and Nakamura E. (2009)** Chemical separation and mass spectrometry of Cr, Fe, Ni, Zn, and Cu in terrestrial and extraterrestrial materials using thermal ionization mass spectrometry. *Analytical chemistry*, **81**, 9787-9794.
- Yamamoto H., Nakamori N., Terabayashi M., Rehman H. U., Ishikawa M., Kaneko Y. and Matsui T. (2010)** Subhorizontal tectonic framework of the Horoman peridotite complex and enveloping crustal rocks, south-central Hokkaido, Japan. *Island Arc*, **19**, 458-469.
- Yoshikawa M., Nakamura E. and Takahashi N. (1993)** Rb-Sr isotope systematics in a phlogopite-bearing spinel lherzolite and its implications for the age and origin of metasomatism in the Horoman peridotite complex, Hokkaido, Japan. *J. Mineral. Petrol. Econ. Geol.*, **88**, 121-130.
- Yoshikawa M. and Nakamura E. (2000)** Geochemical evolution of the Horoman peridotite complex: Implications for melt extraction, metasomatism, and compositional layering in the mantle. *Journal of Geophysical Research*, **105**, 2879. doi:10.1029/1999JB900344